CORROSION INHIBITION OF MAGNESIUM ALLOY BY DISSOLVED LITHIUM CARBONATE

CORROSION INHIBITION OF MAGNESIUM ALLOY BY DISSOLVED LITHIUM CARBONATE

By Basem Mohamed Saad Zaghloul Mohamed Ahmed

A Thesis Submitted to the School of Graduate Studies in Partial Fulfillment
of the Requirements for the Degree Doctor of Philosophy

McMaster University

McMaster University DOCTOR OF PHILOSOPHY (2021)

Hamilton, Ontario (Materials Science and Engineering)

CORROSION INHIBITION OF MAGNESIUM ALLOY BY
DISSOLVED LITHIUM CARBONATE

AUTHOR: Basem Mohamed Saad Zaghloul Mohamd Ahmed

M.Sc. in Chemical Engineering (Military Technical College MTC, Egypt)

B.Sc. in Chemical Engineering (Military Technical College MTC, Egypt)

SUPERVISOR:

Prof. Joseph R. Kish, Professor, Associate Chair – Graduate Department of
Materials Science and Engineering

Faculty of Engineering, McMaster University, Hamilton, Ontario, Canada

NUMBER OF PAGES: 204

Lay Abstract

The objective of this research was to determine the extent to which dissolved lithium carbonate (Li_2CO_3) can inhibit corrosion of lightweight magnesium (Mg) alloy sheet metal in contact with aqueous NaCl solutions. Corrosion inhibition by dissolved Li_2CO_3 in 0.1 M NaCl (aq) was demonstrated for two Mg alloy sheet metal alloys: AZ31B (3% Al, 1% Zn, 0.5% Mn, balance Mg) and ZEK100 (1.3% Zn, 0.2% Nd, 0.25% Zr, balance Mg). As a next step towards the development of a protective coating scheme, corrosion inhibition of ZEK100 by Li_2CO_3, as a surface coating applied, is achieved through a reduction of both the anodic dissolution and the cathode (H_2 gas evolution) kinetics in large part by the formation of a Li-doped MgO film at anodic dissolution sites.

Abstract

The extent to which dissolved Li_2CO_3 can inhibit corrosion of lightweight Mg alloy sheet metal in contact with aqueous NaCl solutions was determined. Two Mg alloy sheet metal alloys were studied, which include: AZ31B (3% Al, 1% Zn, 0.5% Mn, balance Mg) and ZEK100 (1.3% Zn, 0.2% Nd, 0.25% Zr, balance Mg).

Corrosion inhibition was first determined for each alloy separately when immersed in 0.1 M NaCl (aq), with and without dissolved Li_2CO_3 added. The addition of 100 mM Li_2CO_3 (aq) reduces the corrosion rate of AZ31B by a factor of ~10 and ZEK100 by a factor of ~12. Inhibition involves a reduction in both global anodic dissolution and cathode (H_2 gas evolution) kinetics. It also involves suppression of localized filament-like corrosion and associated anode/cathode activation. Site specific cross-sectional analysis of the surface film formed during forced anode activation (polarization) revealed the formation of a Li-doped MgO film, akin to what forms, and provides protection to, Mg alloys with Li added as an alloying element. Such film formation was used to explain all corrosion inhibition aspects.

Corrosion inhibition was then determined for ZEK100 when immersed in 0.1 M NaCl (aq) with and without a spray-deposited Li_2CO_3 surface coatings added. A commercial hexafluoro-titanate/zirconate-polymer conversion coating (Bonderite® MNT 5200) also served as the comparative basis. The Li_2CO_3-coated surface exhibits the lowest relative corrosion, whereas the conversion-coated surface exhibits the highest. Improved corrosion control is attributed to the formation of a compact coating (physical contribution) and the ability of dissolved Li_2CO_3 to inhibit both the anode and cathode kinetics (electrochemical) contribution. The findings are of interest to automotive industry as a possible means to effectively control corrosion of Mg alloy sheet metal using Li_2CO_3 as a surface pre-treatment or the inclusion of Li_2CO_3 to a polymer as an inhibitor additive.

Acknowledgment

First and foremost, my deepest gratitude goes to my supervisor, Prof. Joey Kish, for always being available to provide answers, encouragement, research guidance, and discussions throughout this critical time. Nothing can describe how it feels to have him as a mentor. Thanks for your understanding as I worked within the time constraint. Your excessive support, teaching, and encouragement are appreciated more than you know.

I would also like to express my sincere thanks to my committee member Dr. Joe McDermid for his valuable discussion and suggestions during supervisory committee and CAMC group meetings. I would also express my gratitude to Dr. Peter Kruse and Dr. Kathryn Grandfield for serving as members of my supervisory committee and providing feedback along the way. I would like to thank my colleagues in the CAMC, especially Dr. David Wilkinson, Dr. Beth McNally, and Dr. Mike Bruhis for their kindly help, and Daniella Pallisco for help indexing the SAED patters. I would also like to express my gratitude to the following people for their technical support for my research study: Dr. James Britten (MAX), Dr. Victoria Jarvis (MAX), Dr. Travis Casagrande (CCEM), and Dr. Natalie Hamada (CCEM). I am so grateful to my beautiful county Egypt for their sponsorship and especially Dr. Mohamed Gobara and Dr. Motasfa Seleet from MTC in Egypt for their support.

Words cannot express my gratitude to my wife Iman and my angel sons Anas and Baraa for all the patience, love, and endless support. Lastly, but most importantly, I would like to express my indebtedness to my family, especially my dad, mom and brother for their prayers, inspiration, support, and blessed wishes.

Table of Contents

List of Figures

List of Tables

Declaration of Academic Achievements

This thesis dissertation fulfills in part the requirements of the PhD program in Materials Science and Engineering at McMaster University. All of the research was conducted from September 2018 to June 2021. The thesis includes seven chapters, for which the following declaration of academic achievement is provided:

Chapter 1: Dr. Joseph Kish assisted with the editing.

Chapter 2: Dr. Joseph Kish assisted with the editing.

Chapter 3: This is peer-reviewed journal article (B. Zaghloul, C. F. Glover, J. R. Scully, and J. R. Kish, "Inhibiting Corrosion of Mg Alloy AZ31B-H24 Sheet Metal with Lithium Carbonate," ***Corrosion***, vol. 77, no. 2, pp. 192–203, 2021, doi: 10.5006/3625Dr. Carol Glover (University of Virgina) assisted with the SVET measurements (training pupose) and editing, Dr. John Scully (University of Virgina) and Dr. Joespeh Kish assisted with the editing.

Chapter 4: This is a journal article that has been for publication consideration (B. Zaghloul and J.R. Kish, "Corrosion Inhibition of Mg Alloy ZEK100 Sheet Metal by Dissolved Lithium Carbonate", submitted to the ***Journal of the Electrochemcial Society***, manuscript ID JES-104889, June 23, 2021. Dr. Joseph Kish assisted with the editing.

Chapter 5: This is a journal article that has been for publication consideration (B. Zaghloul and J.R. Kish, “Reducing Corrosion of Mg Alloy ZEK100 Sheet Metal with Lithium Carbonate Surface Pre-Treatment” ssubmitted to ***Surface Coatings and Technology***, manuscript reference number SURFCOAT-D-21-02547, June 22, 2021.) Dr. Joseph Kish assisted with the editing.

Chapter 6: Dr. Joseph Kish assisted with the editing.

Chapter 7: Dr. Joseph Kish assisted with the editing.

Chapter 1

Introduction

Increased use of structural lightweight materials to reduce the mass of transportation vehicles is arguably the best enabling means to improve fuel efficiency [1-2] and, thus reduce harmful greenhouse gas emissions associated with the combustion engine [3]. Wrought magnesium alloy sheet metal, when incorporated into lightweight multi-material structural assemblies, has considerable potential to achieve this goal [4-5]. An exemplary example is the recent Magna International, Ford Motor Company and the U.S. Department of Energy collaboration created to develop a multi-material lightweight vehicle (MMLV) that accomplishes a curb-side mass reduction of 25-30% relative the baseline Ford Fusion production model (1,559 kg). In the MMLV-I design, an Al-intensive vehicle was manufactured to demonstrate a 363 kg mass reduction (23%) and associated 962-gallon fuel savings over a 250,000-km lifetime [4]. In the MMLV-II design, a Mg/composite-intensive vehicle was designed, albeit in a paper study, to demonstrate a 797 kg mass reduction (51%) relative the Ford Fusion baseline [5].

One key technical issue preventing increased use of Mg alloy sheet metal is the corrosion susceptibility in aqueous chloride-containing solutions. This is driven in large part by: (i) electrochemical reactivity (low standard redox potential), (ii) high rate of the H_2 gas evolution reaction as the cathode and (iii) tendency of the native oxide surface film to breakdown and be replaced with a significantly thicker and much less protective corrosion product film. Corrosion of Mg in aqueous chloride-containing solutions involves the conversion of Mg to $Mg(OH)_2$ according to the overall reaction: $Mg + 2H_2O \rightarrow Mg(OH)_2 + H_2$. Elementary steps include: (i) anodic dissolution of Mg to Mg^{2+}, (ii) cathodic reduction of H_2O to H_2, and (iii) precipitation of $Mg(OH)_2$ from a supersaturated alkaline solution at cathode sites. Various alloying, processing and surface modification strategies for improved corrosion control have been proposed and are reviewed elsewhere [3,6,7].

Multi-layered protective coatings are currently the preferred corrosion control strategy used for Mg alloys in automotive applications [8,9]. Typical coating schemes involve an inner pre-treatment layer and a polymer over-layer as a minimum. Class A surface finishes require additional layers, namely a leveler, base coat and a top coat. Pre-treating the surface performs two key functions: (i) provide a measure of barrier layer corrosion control and (ii) provide a favorable surface to promote adhesion of organic over-layers. A myriad of surface pre-treatments have been developed as part of protective coatings for Mg alloys, which, for example, include those reviewed for chemical/ electrochemical deposition [10-12], anodizing [13], plasma electrolytic deposition [14] and sol-gel [15] processes. The ability to provide corrosion inhibition at local defects sites that expose bare metal is a desirable feature. Inhibitor types studied in this context include anode/cathode site specific adsorption and barrier/blocking effects of anionic surfactants [16-19], complexing of dissolved noble metal (relative to Mg) to prevent re-deposition and associated anode/cathode activation [20-21] and sparingly soluble anions to promote surface film formation [22-24].

The emerging protective coating for corrosion control of Mg alloy sheet metal in the MMLV-II design is one comprising a commercial plasma electrolytic deposition surface pre-treatment based on Mg-F-O chemistry (Henkel Bonderite® MgC (magnesium coating)) with a cathodic electrophoretic deposited epoxy (E-coat) over-layer [1]. In a related study, it was shown that a scribed E-coated Mg alloy sheet metal surface pre-treated with the commercial Mg-F-O plasma electrolytic deposition process exhibits a significant reduction in both corrosion spread and depth as compared to a scribed surface pre-treated with the industry baseline conversion coating (hexafluoro-titanate/zirconate-polymer (Bonderite® MNT 5200)) [25]. As Figure 1.1 shows, corrosion control of coated Mg alloys at defect sites, at a level similar to that exhibited by coated AA6xxx Al alloys, remains a significant technical challenge: one that could be addressed with an improved inhibition capability.

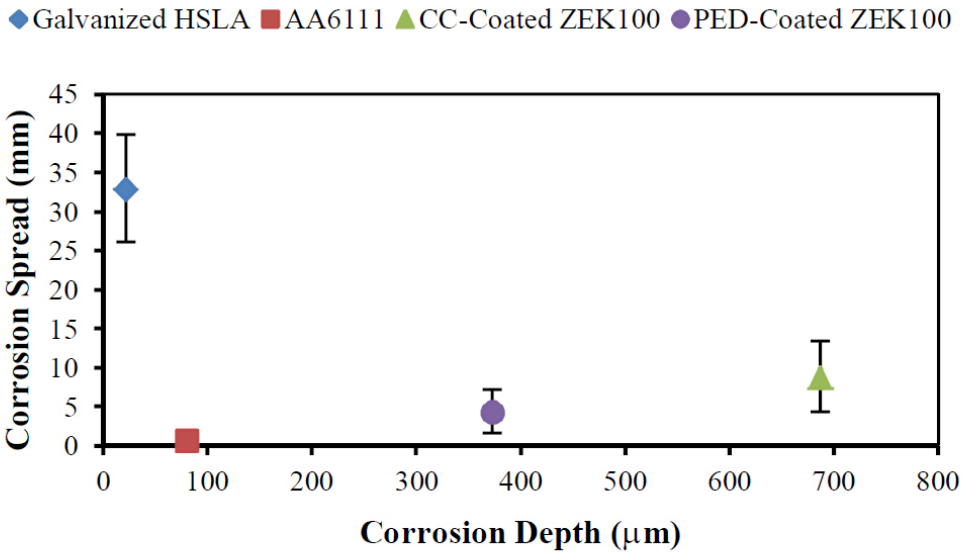

Figure 1.1: Scatter plot of corrosion spread (measured in plan-view) vs. corrosion depth (measured in cross-section) after 1000 h ASTM B117 salt fog exposure [1]. (CC =

conversion coating and PED = plasma electrolytic deposition)

Li_2CO_3 is a promising candidate for inclusion into a protective coating scheme considering the beneficial effect of Li, as an alloying element, has on inhibiting the anodic kinetics of Mg [26] and of dissolved carbonate (CO_3^{2-}/HCO^{3-}/OH^-) on inhibiting both the anode and cathode kinetics of Mg [27-29]. Alloyed Li promotes the formation of Li-doped MgO surface film [30-32] that shows a self-healing capability [33] when mechanically damaged (scratched). Li_2CO_3 has been added as a leachable inhibitor additive in a protective coating applied to Al alloys for improved corrosion control [34-36]. Dissolved Li ions promote the fast formation of a protective multi-layered Al-Li-O surface film [36].

The overarching objective of my research is to determine the extent to which dissolved Li_2CO_3 inhibits corrosion of Mg alloy sheet metal when in contact with NaCl (aq). Conventional and scanning electrochemical and bulk immersion measurements were coupled with site specific surface structure and composition measurements for this purpose. This thesis contains seven chapters, including this introduction. Chapter 2 presents a literature review that places this research hypothesis and associated objectives within the current state of knowledge. Chapters 3 to 5 then present individual journal articles that present and discuss the experimental results. Chapter 3 is a published peer-reviewed article, whereas Chapters 4 and 5 present articles that have been submitted for peer-review publication. A global discussion of the experimental results is presented in Chapter 6 and proposed future research directions. Finally, Chapter 7 presents the global conclusions.

1.1 References

[1] J. R. Kish, Z. Cano, A. Kobylecky, J. McDermid, and T. Skszek, “Comparative Corrosion Assessment of Coated Alloys for Multi-Material Lightweight Vehicle Architectures,” *SAE Tech. Pap.* vol. 01, no. 0738, 2015, doi: 10.4271/2015-01-0738.

[2] Younes, Amir, “Effect of Electrolyte Flow on the Corrosion Behaviour of AZ31B Alloy for Use in the Automotive Industry” McGill University (Canada), 2018.

[3] M. Esmaily, J. E. Svensson, S. Fajardo, N. Birbilis, G. S. Frankel, S. Virtanen, R. Arrabal, S. Thomas, and L. G. Johansson., “Fundamentals and Advances in Magnesium Alloy Corrosion,” *Prog. Mater. Sci.*, vol. 89, pp. 92–193, 2017, doi: 10.1016/j.pmatsci.2017.04.011.

[4] L. Bushi, “Comparative LCA Study of the Magna / Ford MMLV Concept Vehicle Design Comparative LCA Study of Lightweight Auto parts of MMLV Mach-I Vehicle as per ISO 14040 / 44 LCA Standards and CSA Group 2014 LCA Guidance Document for Auto Parts,” *Engineering Solutions for Sustainability*, Springer, Cham, pp. 193-208, 2015.

[5] T. Skszek, “Demonstration Project for a Multi-Material Lightweight Prototype Vehicle as Part of the Clean Energy Dialogue with Canada,” United States: N. p., 2015. Web. doi:10.2172/1332277.

[6] X. B. Chen, H. Y. Yang, T. B. Abbott, M. A. Easton, and N. Birbilis, “Magnesium: Engineering the Surface,” *JOM*, vol. 64, no. 6, pp. 650–656, 2012, doi: 10.1007/s11837-012-0331-3.

[7] K. Gusieva, C. H. J. Davies, J. R. Scully, and N. Birbilis, “Corrosion of Magnesium Alloys: The Role of Alloying,” *Int. Mater. Rev.*, vol. 60, no. 3, pp. 169–194, 2015, doi: 10.1179/1743280414Y.0000000046.

[8] M. P. Brady, W. J. Joost, and C. D. Warren, “Insights from a Recent Meeting :

Current Status and Future Directions in Magnesium Corrosion Research," *Corrosion*, vol. 73, no. 5, pp. 452–462, 2017, doi.org/10.5006/2255.

[9] W. J. Joost, "Reducing Vehicle Weight and Improving Energy Efficiency Using Integrated Computational Materials Engineering," *JOM*, vol. 64, no. 9, pp. 1032-1038, 2012, doi: 10.1007/s11837-012-0424-z.

[10] J. E. Gray and B. Luan, "Protective Coatings on Magnesium and its Alloys - A Critical Review," *J. Alloys Compd.*, vol. 336, no. (1-2), pp. 88–113, 2002, doi.org/10.1016/S0925-8388(01)01899-0

[11] X. B. Chen, N. Birbilis, and T. B. Abbott, "Review of Corrosion-Resistant Conversion Coatings for Magnesium and its Alloys," *Corrosion*, vol. 67, no. 3, pp. 1–16, 2011, doi: 10.5006/1.3563639.

[12] I. Milošev and G. S. Frankel, "Review - Conversion Coatings Based on Zirconium and/or Titanium," *J. Electrochem. Soc.*, vol. 165, no. 3, pp. C127-C144, 2018, doi: 10.1149/2.0371803jes.

[13] C. Blawert, W. Dietzel, E. Ghali, and G. Song, "Anodizing Treatments for Magnesium Alloys and their Effect on Corrosion Resistance in Various Environments," *Adv. Eng. Mater.*, vol. 8, no. 6, pp. 511–533, 2006, doi: 10.1002/adem.200500257.

[14] J. Dou, Y. Chen, H. Yu, and C. Chen, "Research Status of Magnesium Alloys by Micro-Arc Oxidation: A Review," *Surf. Eng.*, vol. 33, no. 10, pp. 731–738, 2017, doi: 10.1080/02670844.2017.1278642.

[15] M. Talha, Y. Ma, M. Xu, Q. Wang, Y. Lin, and X. Kong, "Recent Advancements in Corrosion Protection of Magnesium Alloys by Silane-Based Sol-Gel Coatings," *Ind. Eng. Chem. Res.*, vol. 59, no. 45, pp. 19840–19857, 2020, doi: 10.1021/acs.iecr.0c03368.

[16] H. Gao, Q. Li, Y. Dai, F. Luo, and H. X. Zhang, "High Efficiency Corrosion

Inhibitor 8-Hydroxyquinoline and its Synergistic Effect with Sodium Dodecylbenzenesulphonate on AZ91D Magnesium Alloy," *Corros. Sci.*, vol. 52, no. 5, pp. 1603–1609, 2010, doi: 10.1016/j.corsci.2010.01.033.

[17] D. Eaves, G. Williams, and H. N. McMurray, "Inhibition of Self-Corrosion in Magnesium by Poisoning Hydrogen Recombination on Iron Impurities," *Electrochim. Acta*, vol. 79, pp. 1–7, 2012, doi: 10.1016/j.electacta.2012.05.148.

[18] A. Frignani, V. Grassi, F. Zanotto, and F. Zucchi, "Inhibition of AZ31 Mg Alloy Corrosion by Anionic Surfactants," *Corros. Sci.*, vol. 63, pp. 29–39, 2012, doi: 10.1016/j.corsci.2012.05.012.

[19] N. Dinodi and A. N. Shetty, "Alkyl Carboxylates as Efficient and Green Inhibitors of Magnesium Alloy ZE41 Corrosion in Aqueous Salt Solution," *Corros. Sci.*, vol. 85, pp. 411–427, 2014, doi: 10.1016/j.corsci.2014.04.052.

[20] S. V. Lamaka, D. Höche, R. P. Petrauskas, C. Blawert, and M. L. Zheludkevich, "A New Concept for Corrosion Inhibition of Magnesium: Suppression of Iron Re-Deposition," *Electrochem. Commun.*, vol. 62, pp. 5–8, 2016, doi: 10.1016/j.elecom.2015.10.023.

[21] S. V. Lamaka, B. Vaghefinazari, D. Mei, R. P. Petrauskas, D. Höche, and M. L. Zheludkevich, "Comprehensive Screening of Mg Corrosion Inhibitors," *Corros. Sci.*, vol. 128, pp. 224–240, 2017, doi: 10.1016/j.corsci.2017.07.011.

[22] G. Williams, H. N. McMurray, and R. Grace, "Inhibition of Magnesium Localised Corrosion in Chloride Containing Electrolyte," *Electrochim. Acta*, vol. 55, no. 27, pp. 7824–7833, 2010, doi: 10.1016/j.electacta.2010.03.023.

[23] G. Williams, R. Grace, and R. M. Woods, "Inhibition of the Localized Corrosion of Mg Alloy AZ31 in Chloride Containing Electrolyte," *Corrosion*, vol. 71, no. 2, pp. 184–198, 2015, doi: 10.5006/1376.

[24] Z. Feng, "Erratum: Corrosion Inhibition of AZ31 Mg Alloy by Aqueous Selenite

(SeO 3 2−),” *J. Electrochem. Soc.*, vol. 167, no. 8, p. 089002, 2020, doi: 10.1149/1945-7111/ab8928.

[25] J. R. Kish, Z. Cano, A. Kobylecky, J. McDermid, and T. Skszek, “Comparative Corrosion Assessment of Coated Alloys for Multi-Material Lightweight Vehicle Architectures,” *SAE Tech. Pap.* vol. 01, no. 0738, 2015, doi: 10.4271/2015-01-0738.

[26] W. Xu, Birbilis N, Sha G, Wang Y, Daniels JE, Xiao Y, Ferry M “A High-Specific-Strength and Corrosion-Resistant Magnesium Alloy,” *Nat. Mater.*, vol. 14, no.12, pp. 1229–1236, 2015, doi: 10.1038/NMAT4435.

[27] E. Gulbrandsen, “Anodic behaviour of Mg in HCO_3^-/CO_3^{2-} Buffer Solutions. Quasi-Steady Measurements,” *Electrochim. Acta*, vol. 37, no. 8, pp. 1403–1412, 1992, http://www.sciencedirect.com/science/article/pii/001346869287014Q.

[28] B. Raza and S. Moon, “Electrochemical Properties of Air-Formed Oxide Film-Covered AZ31 Mg Alloy in Aqueous Solutions Containing Various Anions,” vol. 50, no. 3, pp. 147–154, 2017, doi.org/10.5695/JKISE.2017.50.3.147.

[29] L. Prince, M. A. Rousseau, X. Noirfalise, L. Dangreau, L. B. Coelho, and M. G. Olivier, “Inhibitive Effect of Sodium Carbonate on Corrosion of AZ31 Magnesium Alloy in NaCl Solution,” *Corros. Sci.*, vol. 179, pp. 109131, 2021, doi: 10.1016/j.corsci.2020.109131.

[30] Y. M. Yan, O. Gharbi; A. Maltseva; X.B. Chen; Z.R. Zeng; S.W. Xu; W.Q. Xu; P. Volovich; M. Ferry; N. Birbilis, “Investigating the structure of the surface film on a corrosion resistant Mg-Li (-Al-Y-Zr) alloy,” *Corrosion*, vol. 75, no. 1, pp. 80-89, 2019, https://doi.org/10.5006/2995 .

[31] Y. Yan, Y. Qiu, O. Gharbi, N. Birbilis, and P. N. H. Nakashima, “Characterisation of Li in the Surface Film of a Corrosion Resistant Mg-Li-(Al-Y- Zr) Alloy,” *Appl. Surf. Sci.*, vol. 494, pp. 1066–1071, 2019, doi: 10.1016/j.apsusc.2019.07.167.

[32] Yan, Y.M., Maltseva, A., Zhou, P., Li, X.J., Zeng, Z.R., Gharbi, O., Ogle, K., La Haye, M., Vaudescal, M., Esmaily, M. and Birbilis, N, “On the In-Situ Aqueous Stability of an Mg-Li- (Al-Y-Zr) Alloy: Role of Li,” vol. 164, pp. 108342, 2020, doi: 10.1016/j.corsci.2019.108342.

[33] Yan, Y., Zhou, P., Gharbi, O., Zeng, Z., Chen, X., Volovitch, P., Ogle, K. and Birbilis, N, “Investigating Ion Release using Inline ICP during In Situ Scratch Testing of an Mg-Li- (Al-Y-Zr) alloy,” *Electrochem. Commun.*, vol. 99, pp. 46–50, 2019, doi: 10.1016/j.elecom.2019.01.001.

[34] P. Visser, Y. Gonzalez-Garcia, J. M. C. Mol, and H. Terryn, “Mechanism of Passive Layer Formation on AA2024-T3 from Alkaline Lithium Carbonate Solutions in the Presence of Sodium Chloride,” *J. Electrochem. Soc.*, vol. 165, no. 2, pp. C60–C70, 2018, doi: 10.1149/2.1011802jes.

[35] P. Visser, H. Terryn, and J. M. C. Mol, “Active Corrosion Protection of Various Aluminium Alloys by Lithium-Leaching Coatings,” *Surf. Interface Anal.*, vol. 51, no. 12, pp. 1276–1287, 2019, doi: 10.1002/sia.6638.

[36] A Kosari, A., Visser, P., Tichelaar, F., Eswara, S., Audinot, J.N., Wirtz, T., Zandbergen, H., Terryn, H. and Mol, J.M.C, “Cross-Sectional Characterization of the Conversion Layer Formed on AA2024-T3 by a Lithium-Leaching Coating,” *Appl. Surf. Sci.*, vol. 512, pp. 145665, 2020, doi: 10.1016/j.apsusc.2020.145665.

Chapter 2

Literature Review

2.1 Mg Alloy Sheet Metal

To achieve the 50% weight reduction envisioned in the MMLV-II design, significant use of Mg alloy sheet metal as body-in-white (BIW) and closure components, such as doors, fenders, outer hood, roof, and trunk lid, has been proposed [1]. Mg alloy sheet metal is used in higher levels because it exhibits improved mechanical properties relative to than their cast counterparts by eliminating the problematic defects intrinsic to casting [2,3]. Both strength and ductility vary with the sheet direction (orientation), thus yielding anisotropic properties [4]. The number of commercially available Mg sheet metal alloys is very limited. The most commonly used alloy is the AZ31B (3% Al, 1% Zn, 0.5% Mn, balance Mg) since it exhibits a suitable balance between strength, ductility and corrosion performance [5]. However, ZEK100 (1.3% Zn, 0.2% Nd, 0.25% Zr, balance Mg) has been selected in the MMLV-II design given its improved lower temperature formability [6,7].

Both sheet metal alloys are single phase alloys with a distribution of second phase particles. AZ31B is typically provided in the H24 temper, which involves strain hardening during rolling and then partial annealing to half hardness. Second phase particles in AZ31B are predominantly of the course and fine Al-Mn type with circular and rod-like shaped particle [2,8]. The beta (β-$Mg_{17}Al_{12}$) phase is not typically observed in AZ31B. The Al-Mn particles observed are most commonly reported as Al_8Mn_5 with sizes ranging from nanometers to micrometers [9,10]. ZEK100 is typically provided in the fully annealed O temper. Second phase particles in ZEK100 are also near-globular in shape, but include ternary Mg-Zn-Nd and Zr-rich particles [11-13]. The microstructure of both alloys and as well the etched surfaces to show the grains and grain boundaries are shown in Figure 2.1.

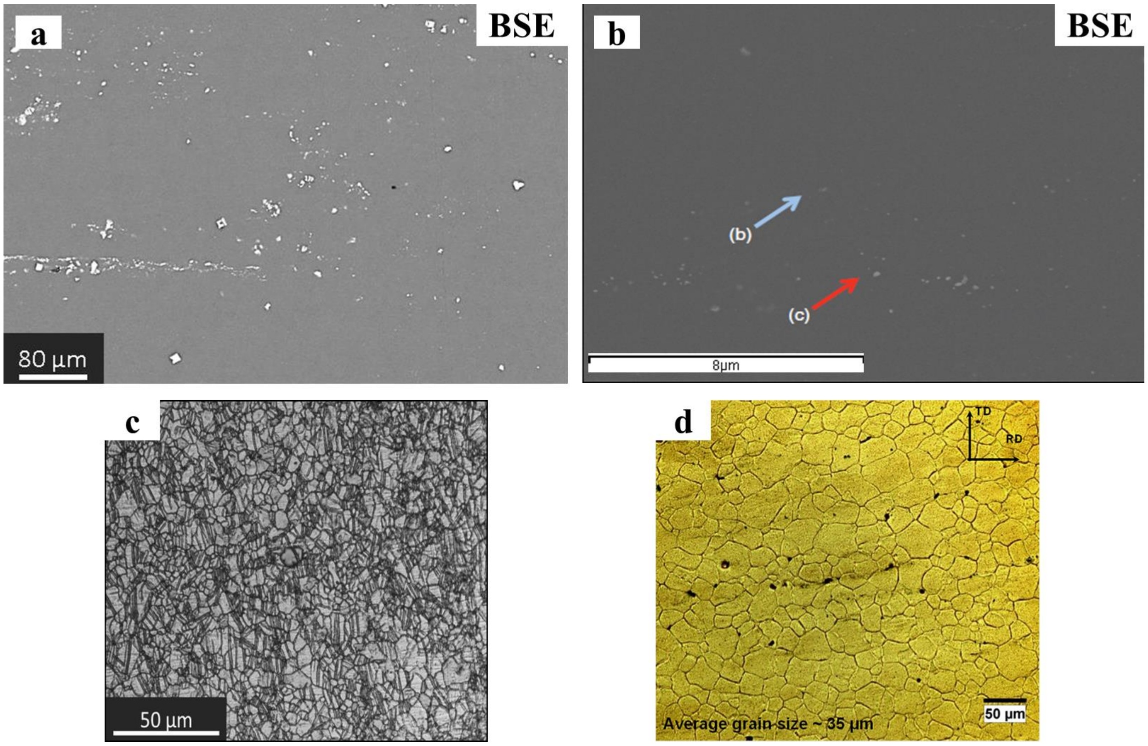

Figure 2.1. Backscattered electron cross-sectional images of (a) AZ31B-H24 [2]and (b) ZEK100-O [11] microstructure showing the coarse intermetallic phase with a bright contrast being aligned along the rolling direction in each case. optical micrographs of the mechanically polished and etched surface of (a) AZ31B-H24 and (b) ZEK100-O.

2.2 Localized Filament-Like Corrosion

The corrosion of Mg in water involves the conversion of Mg metal to $Mg(OH)_2$ according to the overall reaction: $Mg + 2H_2O \rightarrow Mg(OH)_2 + H_2$. Elementary steps of this process include: (i) anodic dissolution of Mg to Mg^{2+}, (ii) cathodic reduction of H_2O to H_2, and (iii) precipitation of $Mg(OH)_2$ from a supersaturated, locally alkaline solution near the cathode sites. $Mg(OH)_2$ is the thermodynamically stable product, but film formation is more complex and involves the additional formation of MgO [8,14,15]. The film is quasi-stable in neutral aqueous solutions and loses integrity in the presence of aggressive anions such as chloride ions [2,16].

The corrosion of AZ31B and ZEK100 involves a rather unique localized filament-like mode that is driven by the so-called cathodic activation (enhanced H_2 gas evolution) of the dissolving surface (anodic activation) [8,17-20]. Local anodes initiate, likely at secondary phase particles that serve as active cathodes [21,22], and propagate laterally across the filmed surface (akin to a filament) driven by cathodic activation, mostly alongside anodic dissolution at the filament head, but with some contribution from the porous oxide/hydroxide corrosion products left behind in the tail [23-25]. The source of cathodic activation continues to be strongly debated [26], with current proposed theories involving an active cathode such as the bare dissolving surface itself [27], noble metal enrichment due to selective dissolution of Mg [15,28] or re-deposition [29][30] or formation of $Mg(OH)_2$ as a corrosion product [31] and the formation and subsequent dissolution of MgH_2 [32].

Both AZ31B [11] and ZEK100 [33] are susceptible to the unique localized corrosion mode that spreads laterally as filaments underneath an intact surface film, in a manner similar to that exhibited by commercially pure Mg [17]. The actual image showing the filament corrosion on the surface for AZ31 immersed in 0.05 M NaCl (aq) for 3.5 h and for ZEK100 immersed in 0.03 M NaCl (aq) for 0.5 h are shown in Figure 2.2a and 2.2b, respectively.

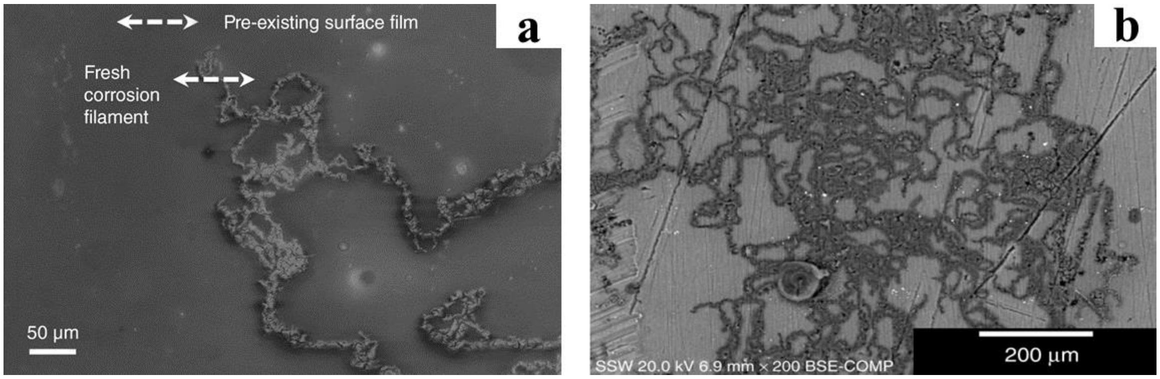

Figure 2.2. (a) Backscattered electron images showing the typical appearance of the localized filament-like corrosion exhibited by Mg alloys: (a) AZ31B immersed in 0.05 M NaCl (aq) for 3.5 h [8] and (b) ZEK100 immersed in 0.03 M NaCl (aq) for 0.5 h [32].

One of the most beneficial methods for monitoring localized corrosion for Mg alloys is the scanning vibrating electrode technique (SVET), also known as the scanning vibrating probe (SVP) technique. Williams *et al.* [17] studied the localized filament-like corrosion of AZ31 under galvanostatic anodic polarization in different NaCl (aq) and investigated the effect of bulk electrolyte pH using SVET. They found that, after starting the anodic polarization, the appearance of dark spots on the surface coincided with a local anodic current, as shown in Figure 2.3. The local anode is shown to move laterally across the surface leaving behind a path that coincides with a local cathodic current. This conversion is the so-called cathodic activation exhibited by dissolving Mg. The intensity of local anodes decreases with decreasing NaCl (aq) concentration at near-neutral pH after 4 h immersion time. For the pH effect, the spread of localized filament-like corrosion is more noticeable at pH > 12, as it slows down considerably.

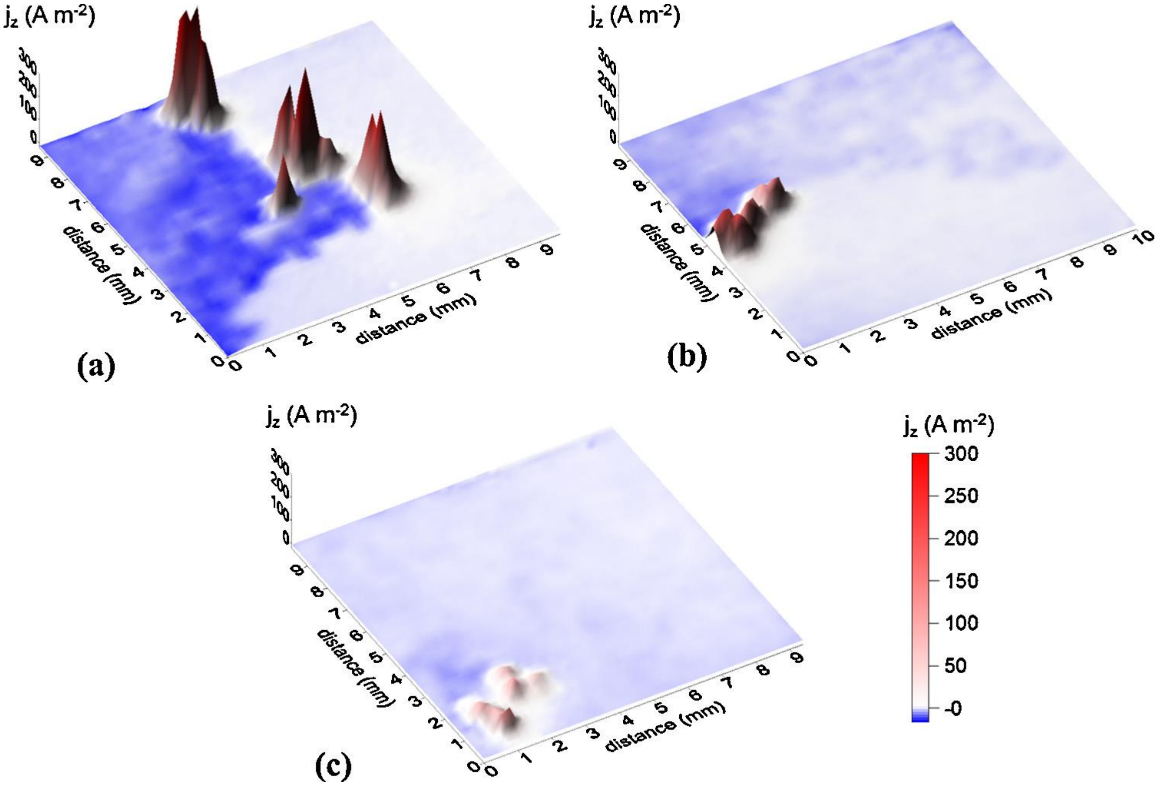

Figure 2.3. SVET-derived current density surface maps of unpolarised AZ31 obtained after 4 h immersion in aerated NaCl (aq) at concentrations (% w/v) of (a) 20%, (b) 1% and (c) 0.2% [17].

The onset of the localized filament-like corrosion requires a breakdown of the intact surface film, which is demarked by a distinct small, but distinct drop in the OCP. The time to breakdown increases with decreasing NaCl (aq) concentration. For 0.05% w/v concentration of NaCl (aq), there is no breakdown potential during this time. As well, it is shown that the amount of filament depends on pH and NaCl (aq) concentration [34].

Kousis *et al*. [35] studied the effect of chloride ion concentration on the initiation and propagation of localized filament corrosion on E717 (ZEK100) in aerated solutions of NaCl (aq) using SVET. Figure 2.4 shows their set of current density distribution maps and associated photographic images recorded for a corroding, recorded after various immersion times. Corrosion initiates as a local anode, which ten propagates along the surface leaving behind a cathode activated trail. They demonstrated that the initiation of localized filament-like corrosion depends on the Cl^{-} concentration in NaCl (aq). The time needed for passivation breakdown potential is delayed and the localized anodic current density is decreased with decreasing the Cl^{-} concentration.

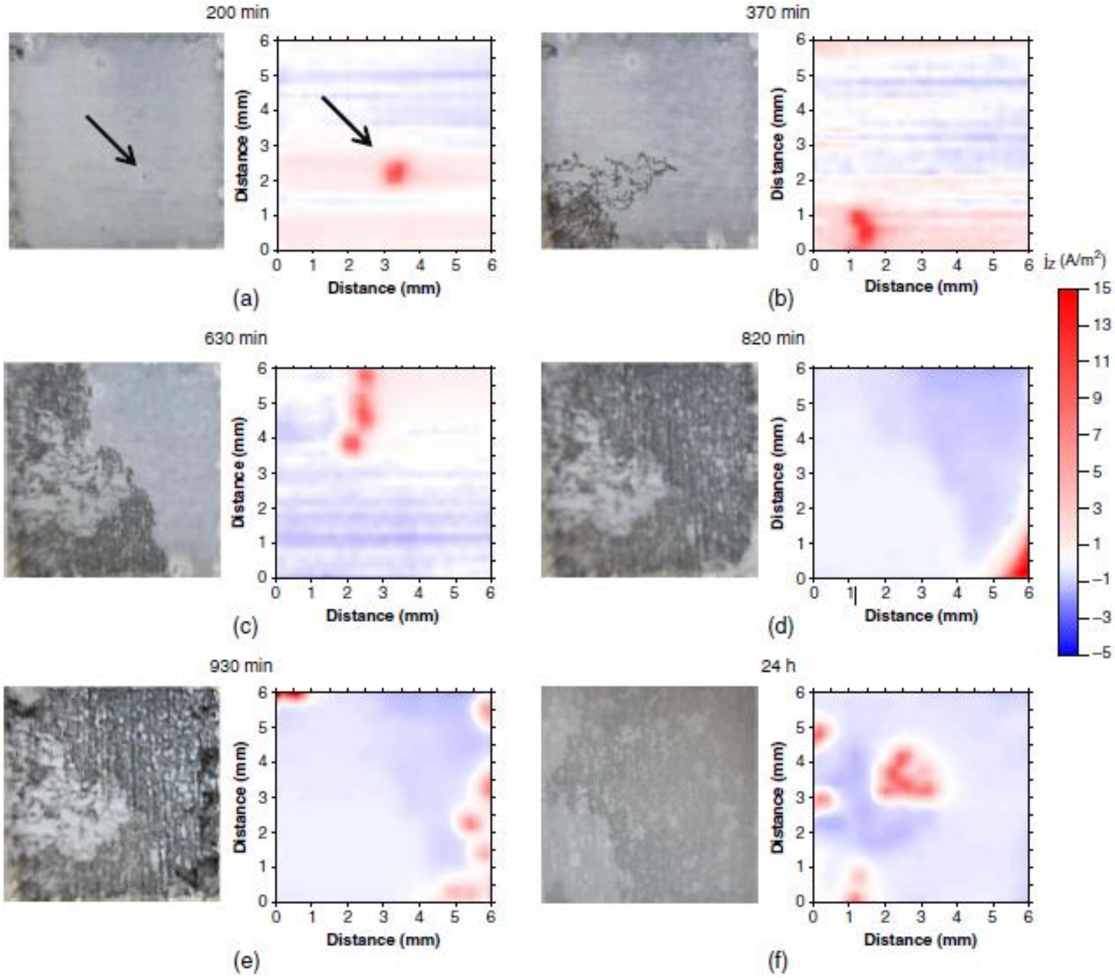

Figure 2.4. SVET current density distribution maps with associated photographic images recorded for E717 corrosion obtained after (a) 200 minutes, (b) 370 minutes, (c) 630 minutes, (d) 820 minutes, (e) 930 minutes, and (f) 24 h immersion in aerated 0.034 M NaCl (aq) [35].

Cano *et al*. [8] used a TEM examination of FIB-prepared cross-sectional samples to provide a physical description of the cathode activation of the corrosion filament trails formed on AZ31B-H24 immersed in NaCl (aq). Their proposed physical description of the filament corrosion is shown in Figure 2.5. The filament is a laterally propagating corrosion process that involves a local dissolving anode head (anode activation) that is coupled to a cathode activated tail. The filament, which is a $MgO/Mg(OH)_2$ mixture. is significantly thicker and more defective than the intact film it propagates underneath. They showed that the presence of through-thickness cracks in the corrosion filament could enable three active cathodes, including: (i) the $Mg(OH)_2$ corrosion product itself, (ii) Al-Mn particles in the form of $Al_{11}Mn_4$ (as determined by STEM-EDS analysis) that are in exposed on the crack wall, (iii) the bare metal surface (with or without noble metal (Zn) enrichment) that is exposed at eth base of the crack.

.

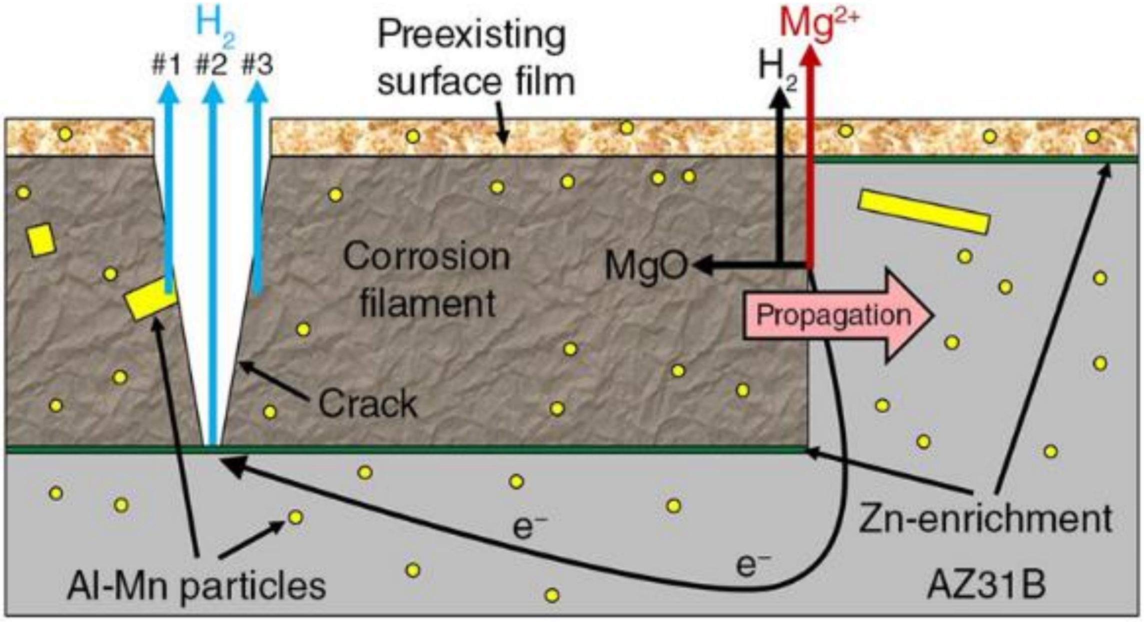

Figure 2.5. Schematic representation of the localized filament-like corrosion exhibited by AZ31B immersed in NaCl (aq) [8].

Binns *et al.* [32] also provided a physical description of the localized filament-like corrosion process: one based on the formation and subsequent dissolution of MgH_2. Their model is shown in Figure 2.6. They propose that that the unstable MgH_2 forms during activated anodic dissolution occurring at the filament head and serves as an active cathode for hydrogen evolution. The effect is greatest at the filament head as the MgH_2 formed is fresh. As MgH_2 is unstable, it transforms to insulating (unreactive) $Mg(OH)_2$ in the aged filament tail, thereby losing its effectiveness as an active cathode. Formation of MgH_2 was concluded based on evidence provided by XRD and dynamic secondary ion mass spectrometry (SIMS).

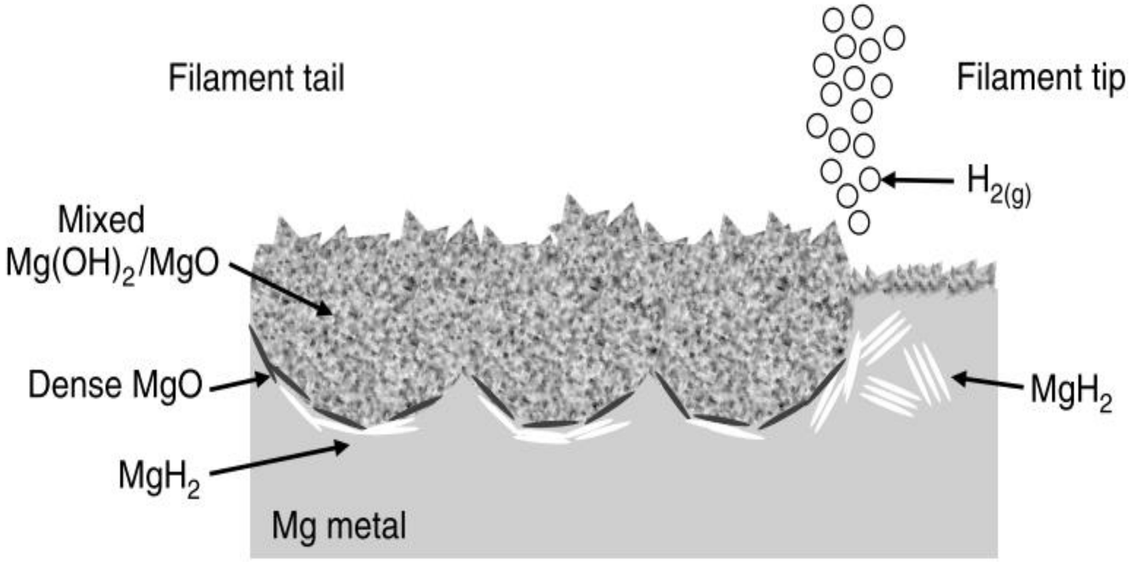

Figure 2.6. Schematic representation of the localized filament-like corrosion exhibited by ZEK100 immersed in NaCl (aq) [32].

2.3 Protective Coating Scheme for Automotive Applications

As mentioned in the Introduction, applying a protective coating scheme consisting of an inner pre-treatment layer and a polymer over-layer sealant is the minimum requirement for corrosion control of Mg alloy components. The current North American automotive benchmark protective coatings scheme consists of a hexafluro-titanate/ zirconate-polymer conversion coating (Bonderite® M-NT 5200™ by Henkel Corporation), with a black cationic epoxy E-coating over-layer sealant applied (POWERCON® 600CX by PPG Industries or equivalent) [1],[36]-[39]. The conversion coating is a more favorable surface on which the epoxy E-coating can be applied. Given that it is applied as a continuous layer, it is expected to provide some contribution to corrosion control by serving as a physical barrier. However, a chemical inhibition contribution to corrosion control is not expected. A possible leachable inhibiting component would be F^- (aq) anions, formed by dissolution of the MgF_2 component (k_{sp} = 5.16×10^{-11} at 25 °C [40]. However, no significant level of corrosion inhibition of Mg [41] or AZ31B [42] is observed in NaCl (aq) with relative small additions (10 mM) F^- (aq).

Brady *et al*. [43] examined the corrosion performance of Bonderite® M-NT 5200™-coated AZ31B and E717 (ZEK100) with and without an epoxy E-coating over-layer applied in saturated $Mg(OH)_2$ (aq) with 1 wt.% NaCl (aq) at ambient temperature. SEM cross-sectional images of the Bonderite® M-NT 5200™ conversion coating on the two alloys are shown in Figure 2.7a and 2.7b, respectively. The thickness of the coating on both layers ranges from 0.6 to 1 μm. Continuous coating forms on both alloys, but the cracks are observed in the coating formed on AZ31B, whereas pores are observed in the coating formed on E717 (ZEK100). The thickness of the epoxy E-coating applied on each conversion-coated alloy is ~10 μm, as shown in Figure 2.7c and 2.7d.

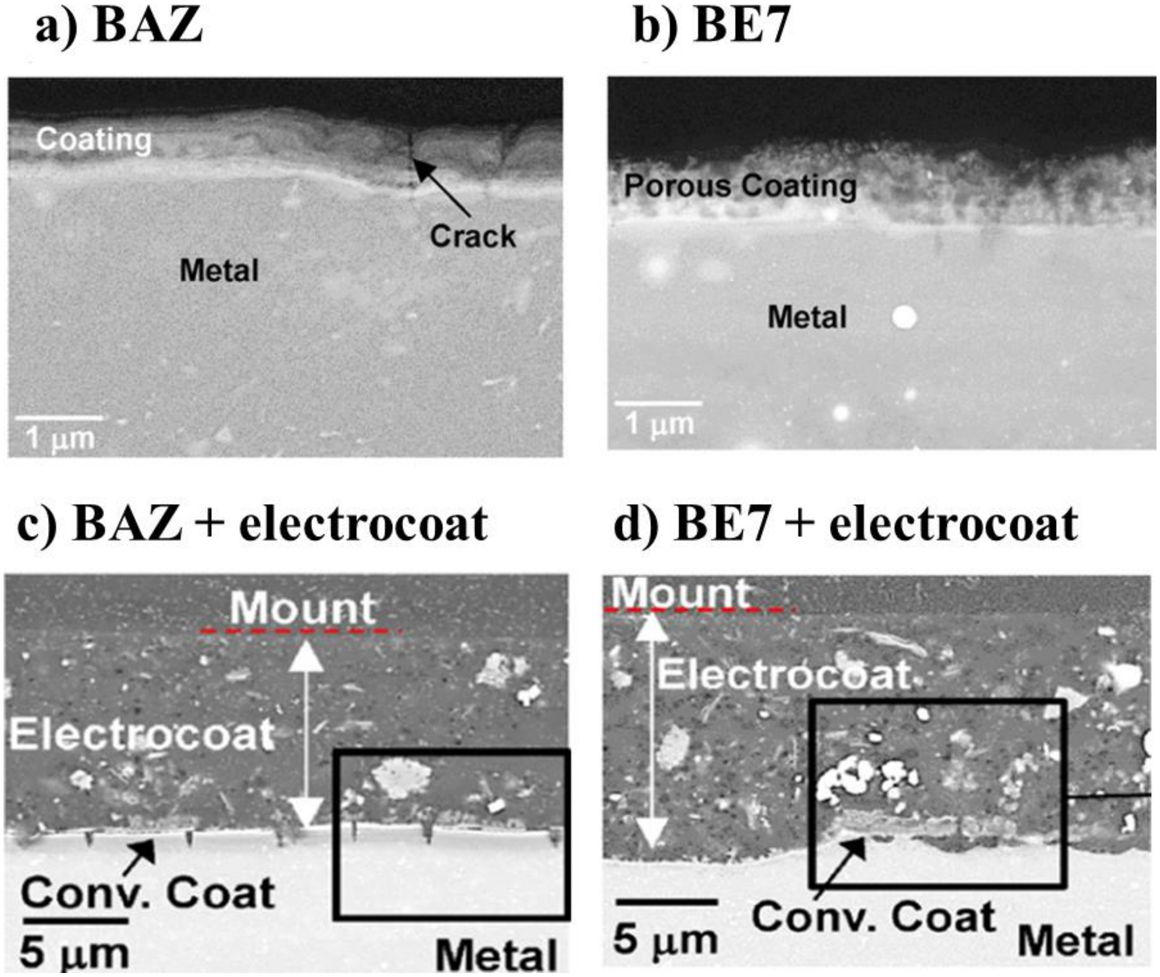

Figure 2.7. Backscattered electron cross-sectional images of the as-conversion coated surfaces (Bonderite® M-NT 5200™) formed on (a) AZ31B (BAZ) and (b) E717 (ZEK100) (BE7). Backscattered electron cross-sectional images of conversion coating (Bonderite® M-NT 5200™) with epoxy E-coating (electrocoat) applied on (c) AZ31B and (d) E717 (ZEK100) [43].

Potentiodynamic polarization measurements of the conversion-coated surfaces, relative to bare metal surfaces, are shown in shown in Figure 2.8. The effect of the conversion coating on the polarization response is more pronounce for AZ31B. The conversion coating causes a significant reduction in the anode kinetics, with little effect on the cathode kinetics. A similar effect on the conversion coating on the polarization response on E717 (ZEK100) is also observed, the effect seems to be not very reproducible.

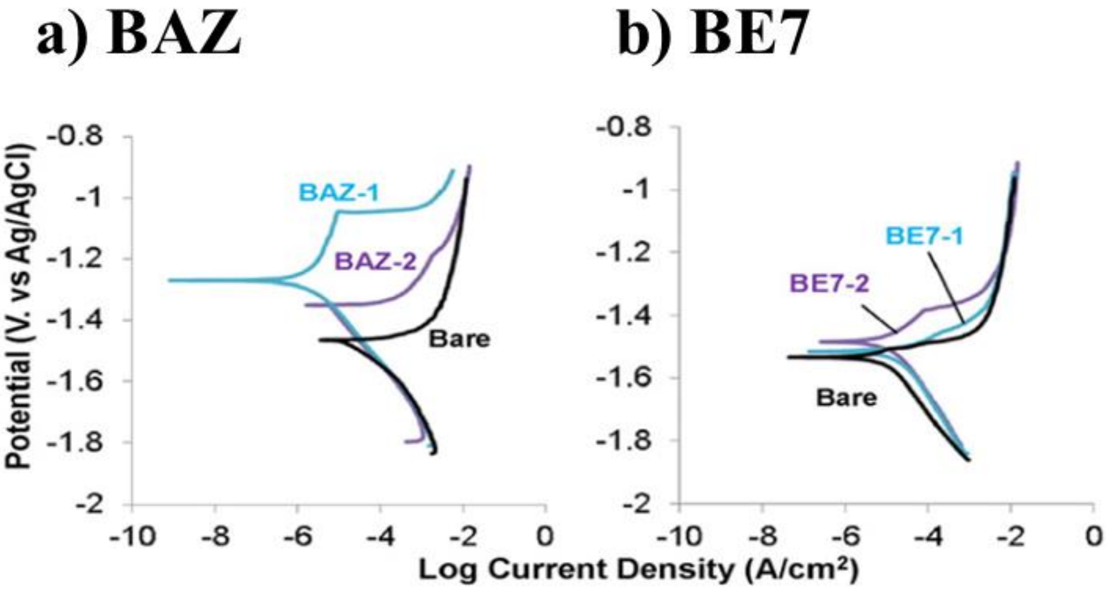

Figure 2.8. Potentiodynamic polarization response for (a) AZ31B (BAZ) and (b) E717 (ZEK100) (BE7) with and without conversion coating (Bonderite® M-NT 5200™) applied in saturated $Mg(OH)_2$ (aq) with 1 wt.% NaCl (aq) at ambient temperature [43].

Figure 2.9a and 2.9b show that the STEM-EDS of AZ31B and E717 (ZEK100) after application of epoxy E-coating over the Bonderite® M-NT 5200™ conversion coating. For both alloys, there is an enrichment of F in the inner layer, presumably from the insoluble MgF_2 formation, which provides barrier layer protection. The epoxy E-coating process is very aggressive towards the conversion coating, causing significant physical damage to the conversion coating on both alloys, as shown in Figure 2.9. No corrosion assessment of the E-coated samples was provided.

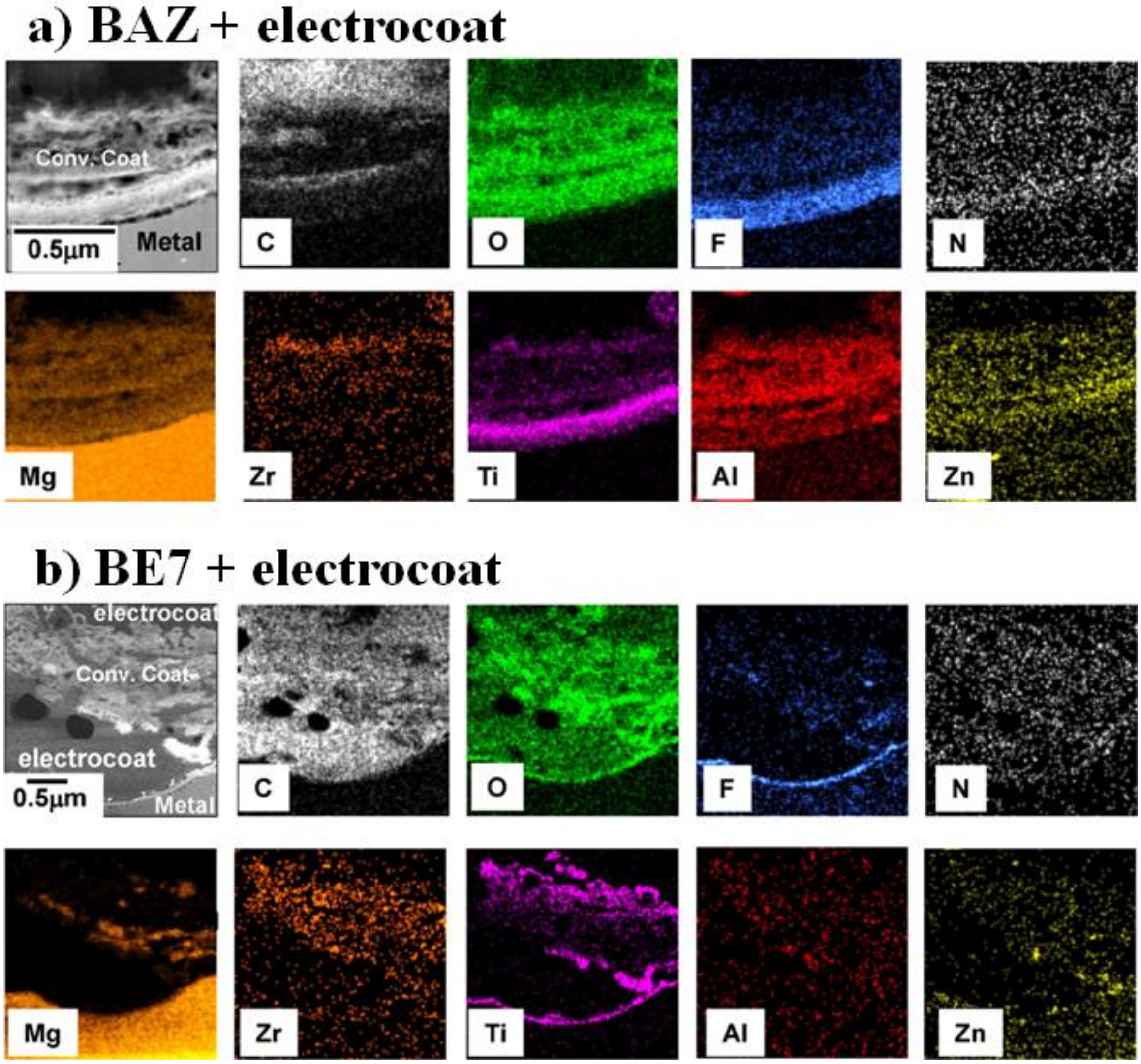

Figure 2.9. Cross-section dark field STEM images and corresponding elemental maps of the E-coated (electrocoat) surface after conversion coating (Bonderite® M-NT 5200™) for (a) AZ31B (BAZ) and (b) E717 (ZEK100) (BE7) [43].

Song *et al*. [37] investigated the effect of mechanical abrasion surface treatment on the relative corrosion performance of AZ31B with a novel electroless E-coating applied directly onto the bare metal surface. The study is relevant since they used a Bonderite® M-NT 5200™ conversion coated surface as a comparative basis. Significant corrosion damage on the conversion-coated sample was observed after 20 h salt spray (ASTM B117) exposure. Unfortunately, bare metals samples were not exposed. Figure 2.10(a) shows the electrochemical polarization response of the conversion-coated surface relative to the electroless E-coated surfaces. The conversion coating does not inhibit the anodic kinetics to any great extent, as very little polarizability is observed in the current response. The impedance response, shown in Figure 2.10(b), also reveals very little corrosion protection given the relatively small size of the capacitance loop in the Nyquist plot. The additional slope observed in the low frequency range in the Bode plot (Figure 2.10(c)) for the conversion-coated surface was attributed to the breakdown of the surface film and subsequent localized corrosion.

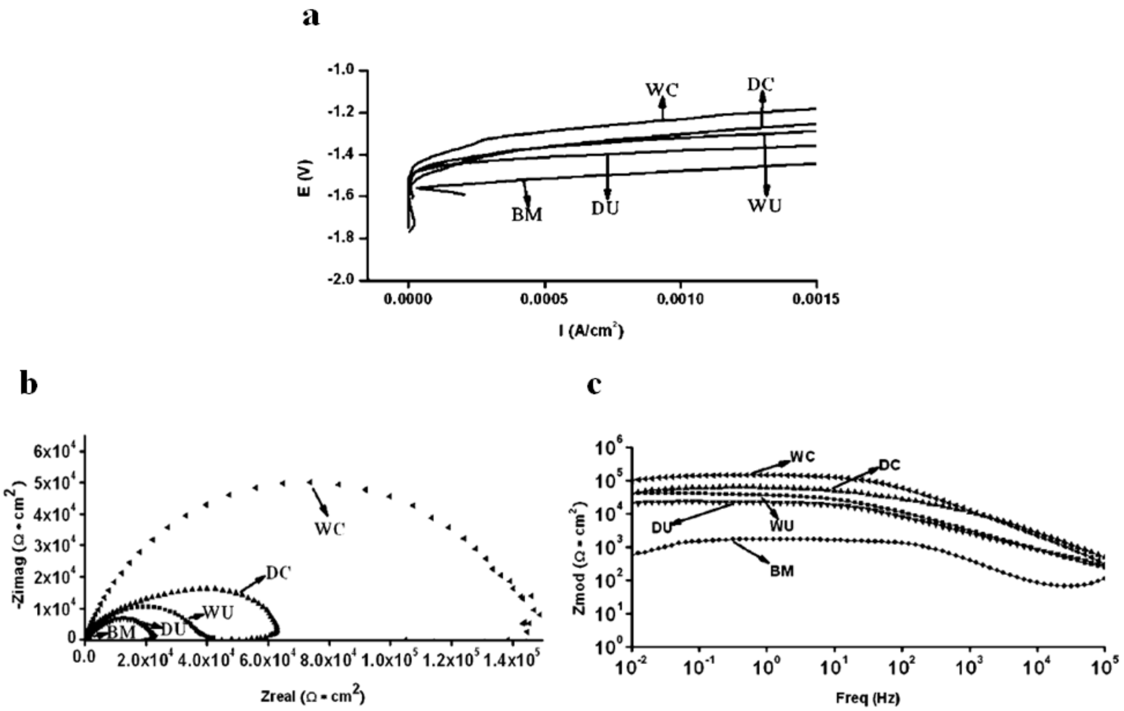

Figure 2.10. Electrochemical response of Bonderite® M-NT 5200™ conversion-coated AZ31B (BM) in 5 wt.% NaCl (aq) at ambient temperature: (a) potentiodynamic polarization, (b) Nyquist plot (immediately after immersion) and (c) Bode plot (immediately after immersion) [37].

Song *et al.* [39] also investigated the relative corrosion performance of epoxy E-coated and powder-coated AZ31 and AZ61 (6% Al, 1% Zn, 0.15% Mn, balance Mg) after pre-treating the surface with by applying the Bonderite® M-NT 5200™ conversion coating. Salt spray (ASTM B117) testing revealed that E-coating provides improved corrosion protection compared to powder coating when applied as the sealant over-layer on the conversion-coated surface (Figure 2.11(a)). The impedance response, shown in Figure 2.11(b), also reveals improved corrosion protection of Bonderite® M-NT 5200™

with the E-coating rather than the powder coating applied as the sealant over-layer. They proposed a six step corrosion process of a coated Mg alloy: (i) corrosive solution penetrates the organic coating through the pores or micro-cracks in the coating and reaches the bare metal substrate, (ii) corrosion of the bare metal surface then begins, (iii) corrosion produces both $Mg(OH)_2$ and H_2 gas bubbles products of the reaction, (iv) corrosion products then promote localized coating blistering or cracking (v) continued corrosion occurs underneath coating, which causes undermining or undercut damage and (vi) copious corrosion product generation coupled with local high pressure of H_2 gas causes visible coating breakdown.

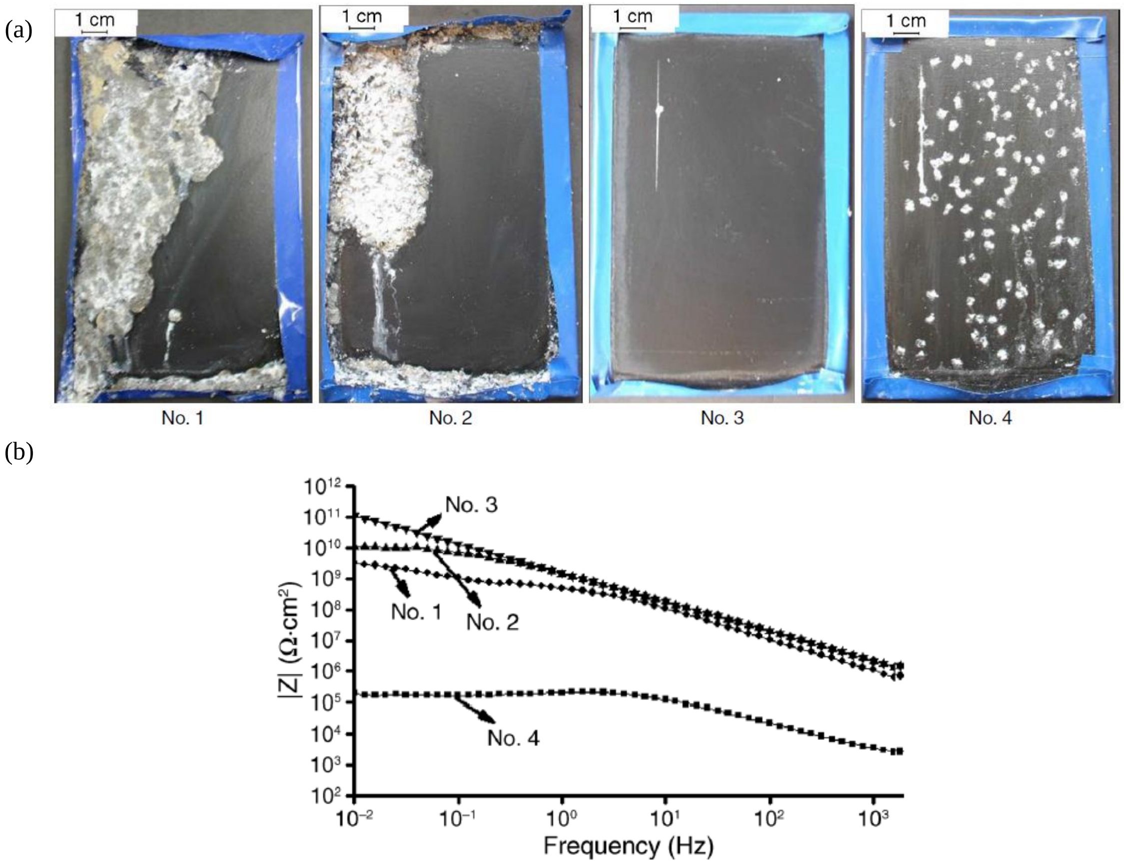

Figure 2.11. (a) Photographs of samples after 1,000 h salt spray (ASTM B117) exposure. (b) Bode plot for samples 1 to 4 after 30 days immersion in 5 wt.% NaCl (aq). (No. 1) powder-coated AZ31, (No. 2) powder-coated AZ61, (No. 3) E-coated and powder-coated AZ31 and (No. 4) E-coated AZ31. [39].

2.4 Inhibitors for Corrosion Control

The storage of inhibiting (inorganic or organic) compounds for controlled release at coating defects sites, however initiated, is a key design criterion for the development of next generation coating schemes. The concept is exemplified by the improved corrosion control of Mg alloys coated with inhibitor intercalated ion-exchangeable hydrotalcite (HT) or layered double hydroxide (LDH) surface pre-treated layers [44]-[50]. It follows that a well-developed understanding of a given inhibitor's efficiency in controlling corrosion of bare Mg alloys in NaCl (aq) is critical to inhibitor selection and, thus coating design. Inhibitor types studied in this context include anode/cathode site specific adsorption and barrier/blocking effects of anionic surfactants [51]-[54], complexing of dissolved noble metal (relative to Mg) to prevent re-deposition and associated cathode activation [55][56], and sparingly soluble anions to promote surface film formation [41],[42],[57]. The focus of this thesis is on the latter: sparingly soluble anions to promote surface film formation.

Williams *et al.* [42] investigated the influence of Na_3PO_4, Na_2CrO_4, NaF, $CeCl_3$ and YCl_3 as a corrosion inhibitor for casting AZ31 in unstirred 5% w/v NaCl (aq) at pH 6.5 and 20 °C. SVET measurements showed that the number density of local anodes had approximately doubled for both Ce and Y salt, the reason for which is not clear. In addition, the addition of NaF (aq) remains ineffective in inhibiting the localized corrosion of AZ31. Moreover, the addition of phosphate and chromate confirm that both types promote a significant level of corrosion inhibition. Figure 2.12 shows the SEM-EDS elemental map of (a) P and (b) Cr distribution over AZ31 after immersion for 4 h in 5 % NaCl (aq) containing the addition of phosphate and chromate. The SEM-EDS maps indicates that $Mg_3(PO_3)_2$ and $Cr(OH)_3$, likely forms over noble Al-Mn particles (active cathodes) in each case, but does form as a continuous layer that completely covers the AZ31 surface. This demonstrates incomplete surface film formation inhibition.

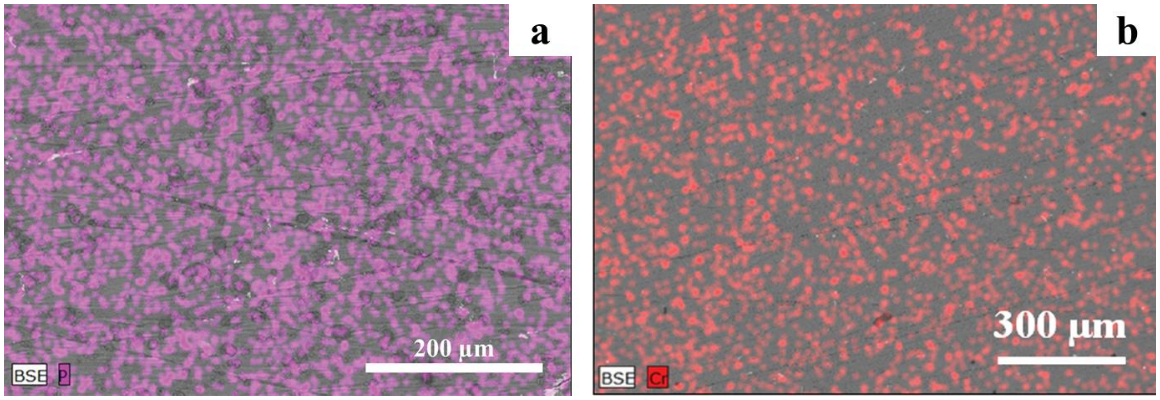

Figure 2.12. SEM-EDS elemental map showing relative abundance of (a) P and (b) Cr (b) for a post-corrosion AZ31 surface after immersion for 4 h in 5% NaCl (aq) containing a 10^{-2} Na_3PO_4 and Na_2CrO_4 addition, respectively [42].

Feng *et al*. [57] investigated the electrochemical response of AZ31 in NaCl (aq) with various Na_2SeO_3 (aq) additions, as a corrosion inhibitor, ranging from 0.5 mM to 50 mM. They separated the inhibition effect to an anodic and cathodic effect. Anodic inhibition depends on of SeO_3^{2-} (aq) concentration and the better corrosion resistance obtained from potentiodynamic polarization and EIS by using 1 mM Na_2SeO_3 (aq). Higher concentrations (10 and 50 mM) or longer periods resulted in thicker film, but unfortunately less protective due to having voids, cracks and was not compact compared to lower concentration (1 mM). This was also confirmed with STEM analysis (Figure 2.13), which showed that the highest concentration of SeO_3^{2-} (aq) (50 mM) coincides with a film that is more porous (contains more voids). They claimed that the cathode H_2 evolution reaction is suppressed due to the formation of hydroxide double layer on Al and Mn particles which does not depend on the SeO_3^{2-} (aq) concentration.

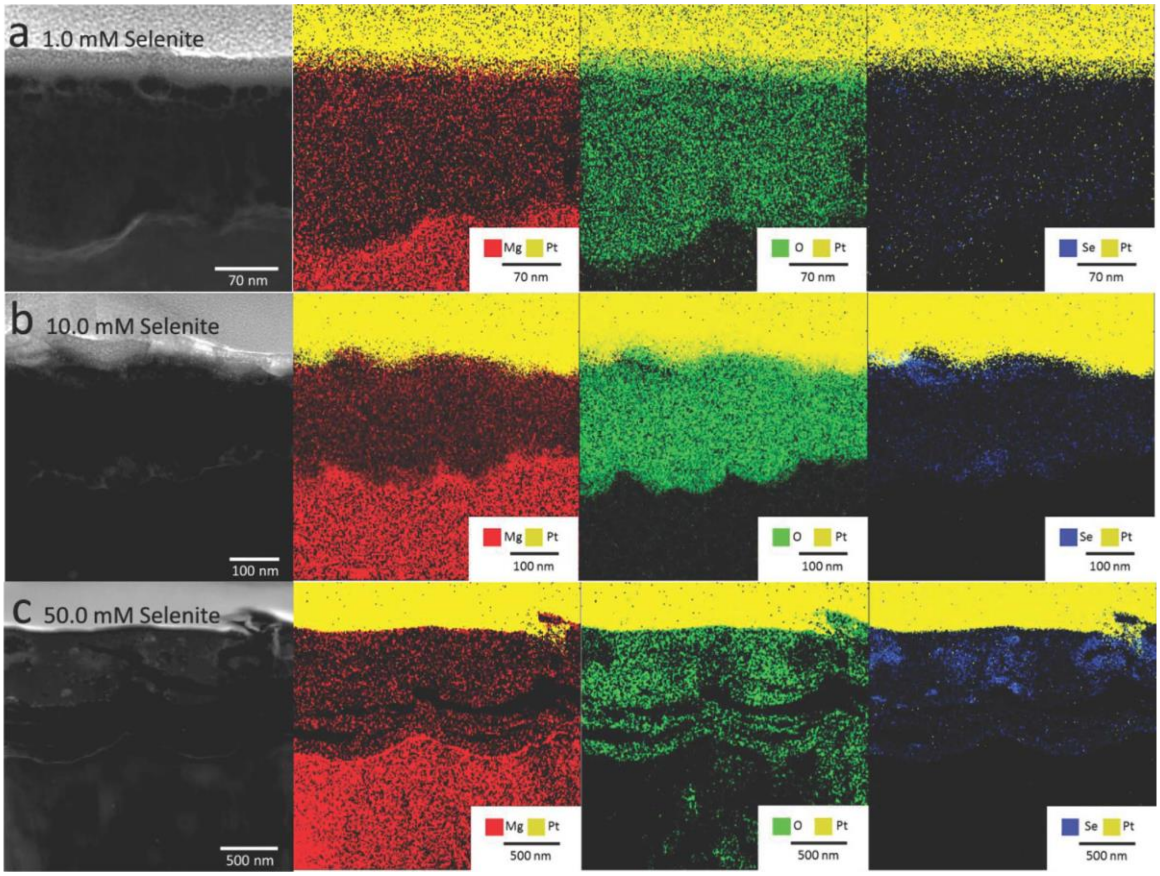

Figure 2.13. STEM images and associated EDS maps of the surface film formed on AZ31 after 24 h immersion 0.1 M NaCl (aq) with various additions of Na_2SeO_3 as a corrosion inhibitor [57].

The formation of protective surface films on Mg alloys by immersion in aqueous carbonate (CO_3^{2-}) solutions as received some attention. Prince *et al.* [58] showed the effect of different concentration of Na_2CO_3 (aq), added as a corrosion inhibitor, for AZ31 immersed in 0.1 M NaCl (aq) saturated with $Mg(OH)_2$, which stabilized the pH at 10.3. They presented that the inhibition efficiency using H_2 evolution test reach 76% using 50 mM Na_2CO_3. As well, they showed that the inhibition effect using Na_2CO_3 from potentiodynamic polarization is anodic and cathodic effect. They showed the formation of uniform and continuous film after immersion for 7 days in the solution with 50 mM Na_2CO_3 (aq), a much improved situation relative to that observed without the inhibitor added (Figure 2.14). Using XPS measurements, they showed that the protective layer is composed of $Mg(OH)_2$, $MgCO_3$ and $Mg_2(OH)_2CO_3$. This protective layer, which is the key for improved the corrosion inhibition of Mg alloys, is sufficient to decrease the i_{corr} with 50 mM Na_2CO_3 (aq) relative to case without.

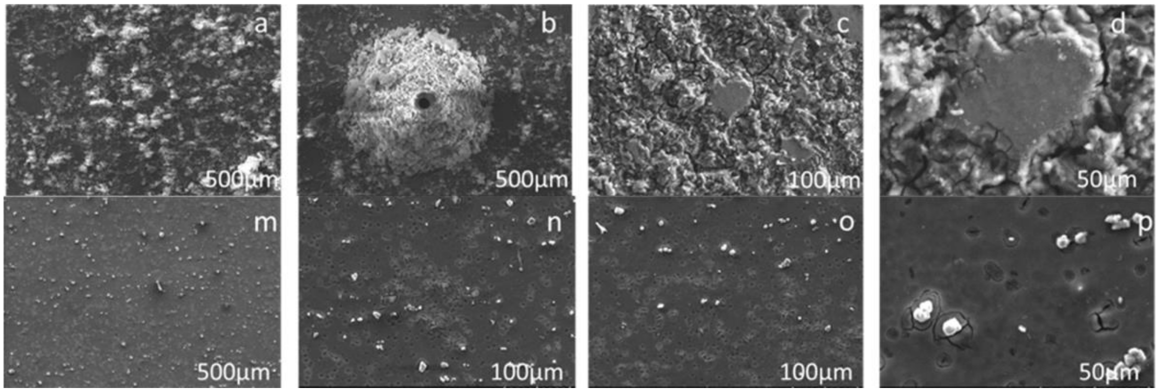

Figure 2.14. Plan view SEM images of the corroded AZ31 surface after 7 days immersion in 0.1 M NaCl (aq) saturated with $Mg(OH)_2$ (a-d) without Na_2CO_3 (aq) addition, and (m-p) with 50 mM Na_2CO_3 (aq) addition [58].

Gulbrandsen *et al*. [59] studied the anodic polarization response of high purity Mg in buffered HCO_3^-/CO_3^{2-} (aq) (pH 9-11). They showed that the corrosion rate depends on HCO_3^- concentration and at higher concentration thicker porous film was observed which provides a pathway for corrosive species interaction with Mg surface.

Fazal *et al*. [60] investigated the effect of 0.01 M (aq) Na salts of Cl^-, F^-, NO_3^-, $CH3COO^-$, SO_4^{2-}, CO_3^{2-} and PO_4^{3-} on the thin native oxide layer formed over AZ31 using OCP, potentiodynamic polarization and EIS. They showed that CO_3^{2-} and PO_4^{3-} dissolve the native oxide layer and promote the formation of a replacement passive layer $MgCO_3$ and $Mg_3(PO_4)_2$. However, the rest of anions promoted the growth of the native oxide film. In addition, they showed the anodic passive behavior using CO_3^{2-} and PO_4^{3-} relative to the rest of anions that show no passivation occurred as shown in Figure 2.15.

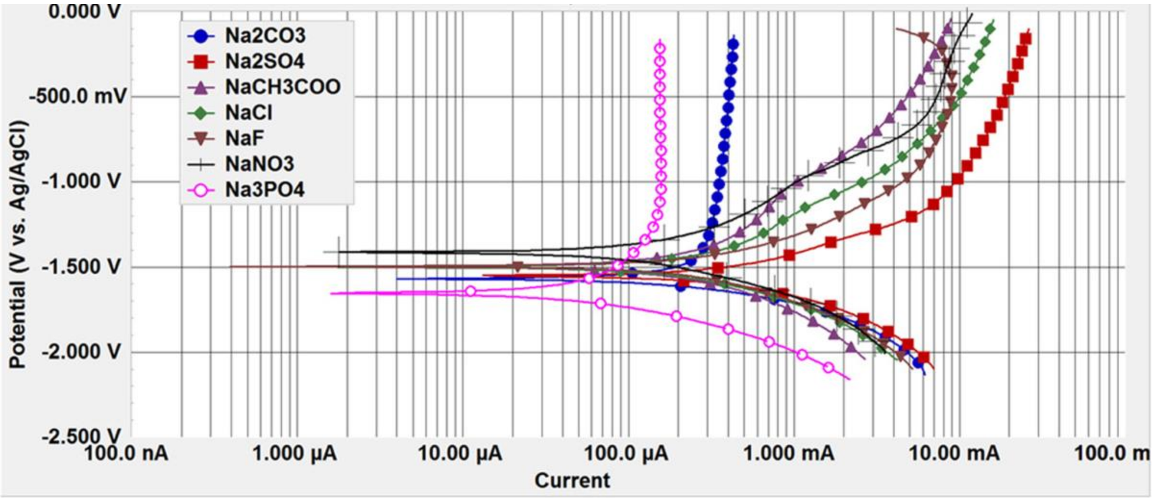

Figure 2.15. Potentiodynamic polarization curves of AZ31 Mg alloy in seven different electrolytes [60].

2.5 Corrosion Resistant Mg-Li Alloys

The tendency for the native oxide/hydroxide surface film to breakdown locally and for the solid oxide/hydroxide corrosion product (cathodic activation) and secondary intermetallic phases to serve as cathodes for H_2 evolution has inspired various alloying, processing and surface modification strategies for improved corrosion control [61]-[63]. Li alloying significantly stifles the anodic kinetics of the Mg matrix, with no concomitant effect on the cathodic kinetics: a unique kinetic combination not observed in other Mg alloys [64]. This, combined with inhibiting effect of dissolved carbonate (CO_3^{2-}/HCO_3^-/

OH^-) on inhibiting both the anode and cathode kinetics of Mg [58]-[60], underpins the interest in Li_2CO_3 as a dissolvable inhibitor for Mg alloys.

Xu *et al*. [64] designed an ultralow density Mg-Li alloy (1.4 g/cm^3). The conventional extruded alloy exhibits a corrosion current density similar to other Mg alloys, such as AZ31B and ZEK100. However, by alloying modification and thermo-mechanical processing, the corrosion current density is significantly reduced, as shown in Figure 2.16. Improved corrosion resistance is attained without sacrificing mechanical properties.

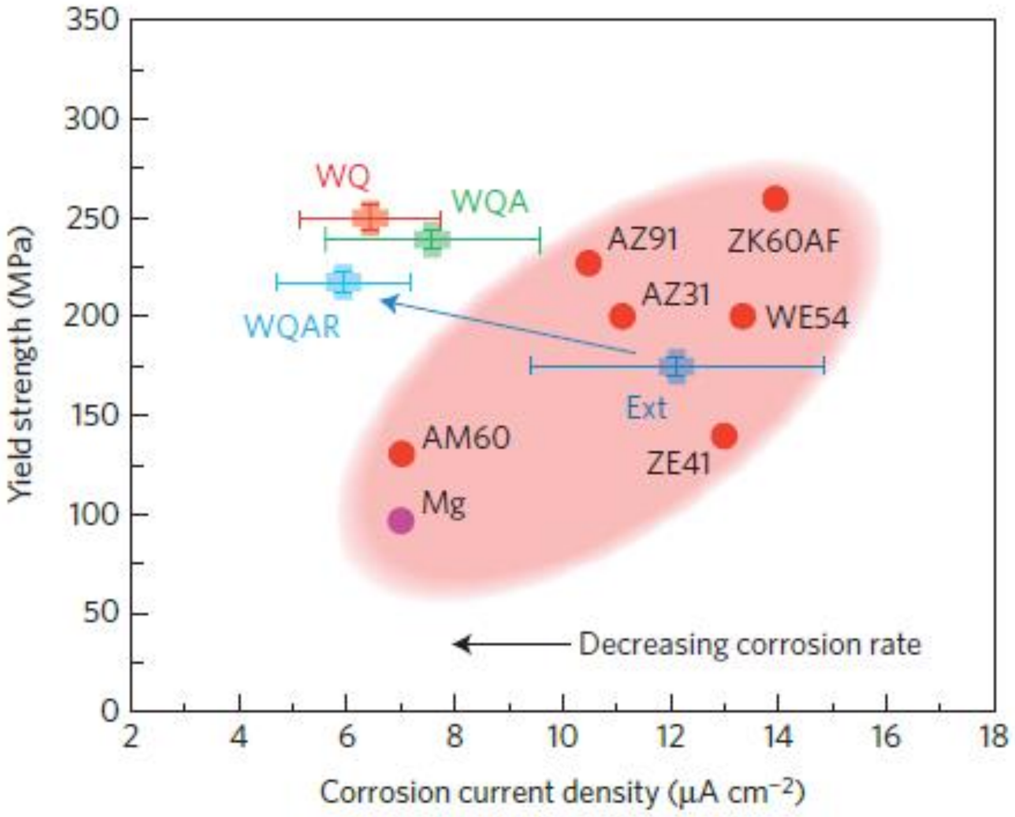

Figure 2.16. Plot of yield strength versus corrosion current density for Mg-Li alloys relative to conventional Mg alloys [64].

Figure 2.17 shows the schematic diagram of increasing Li content effect on the stability of the film that forms on Mg-Li alloys under atmospheric exposure conditions. The conventional HCP Mg matrix phase forms a defective oxide and hydroxide bi-layered film, as shown in Figure 2.17(a). An increase in the Li content promotes the formation of a Li_2CO_3 layer. Protection is compromised since the presence of secondary phases prevents the formation of a continuous layer, as shown in Figure 2.17(b). Figure 2.17(c) shows that the complete coverage with a relative thick and continuous Li_2CO_3 layer forms with a further increase in the Li content.

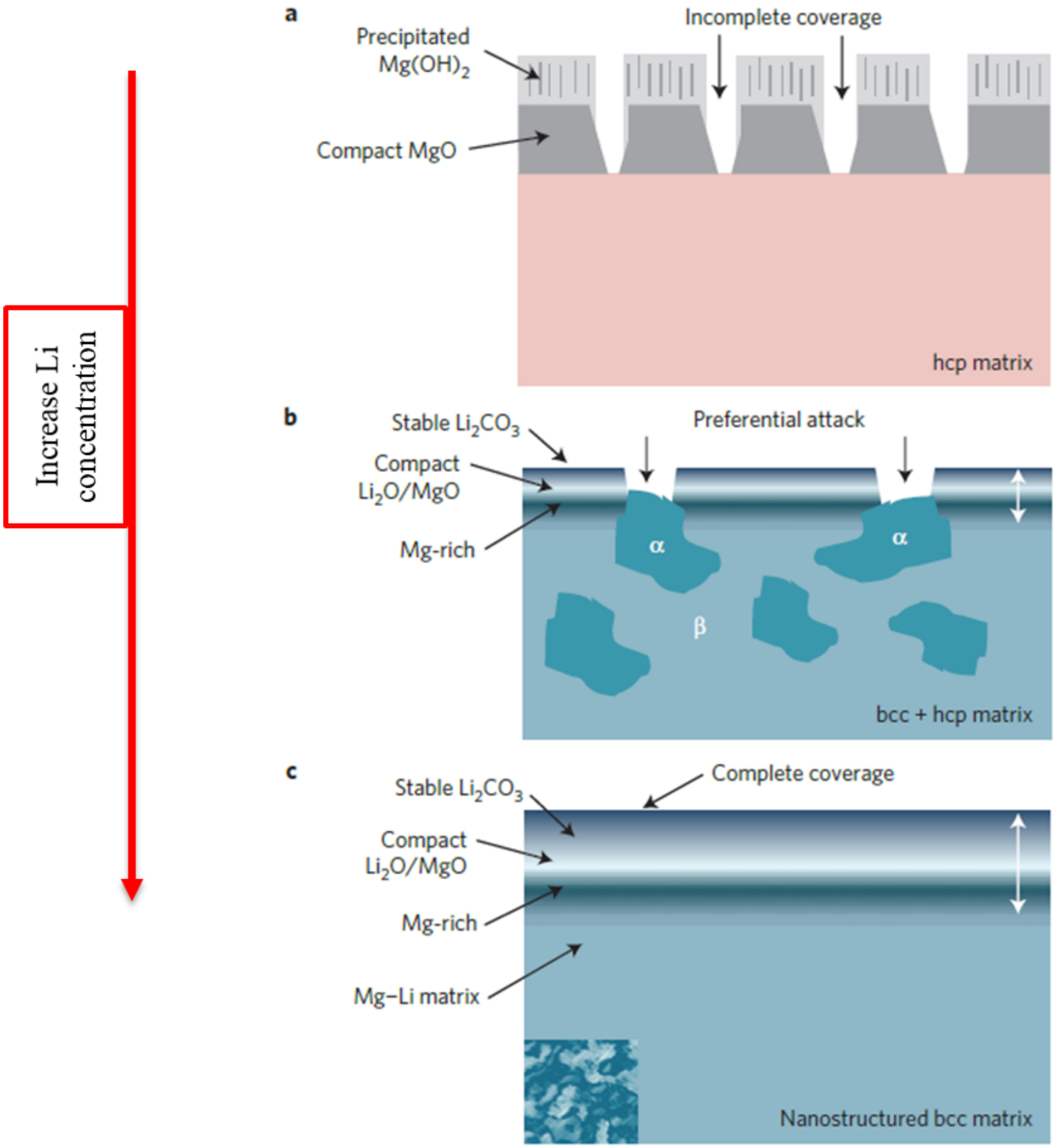

Figure 2.17. Surface layer formation on HCP Mg and BCC Mg–Li after exposure to atmospheric exposure conditions: (a) incomplete coverage of the surface film developed on conventional hcp Mg alloys, (b) thin surface film on the extruded Mg–Li alloy and potential reaction sites due to the conventional two-phase structure and (c) complete coverage of the thicker surface film on the solute nanostructured bcc Mg–Li alloy. [64].

Yan *et al*. [65] investigated the aqueous stability of Mg-Li (30.3 % at.) and showed that the Li_2CO_3 layer formed after atmospheric exposure, and associated Li and C surface enrichment is removed after exposure in aqueous solution, as shown is Figure 2.18(a and b). Figure 2.18c shows that the eventual corrosion inhibition by Li alloying is achieved by selectively dissolving of Mg and Li at anodic areas followed by the formation of Li-doped MgO layer, which hinder the transformation of MgO to $Mg(OH)_2$ and, this active localized dissolution. Film formation involves: (i) selective dissolution of Li^+, (ii) diffusion of Mg^{2+} via MgO and dissolution of Mg^{2+}, (iii) doping of MgO by Li^+ and (iv) corrosion products formation around cathodic sites.

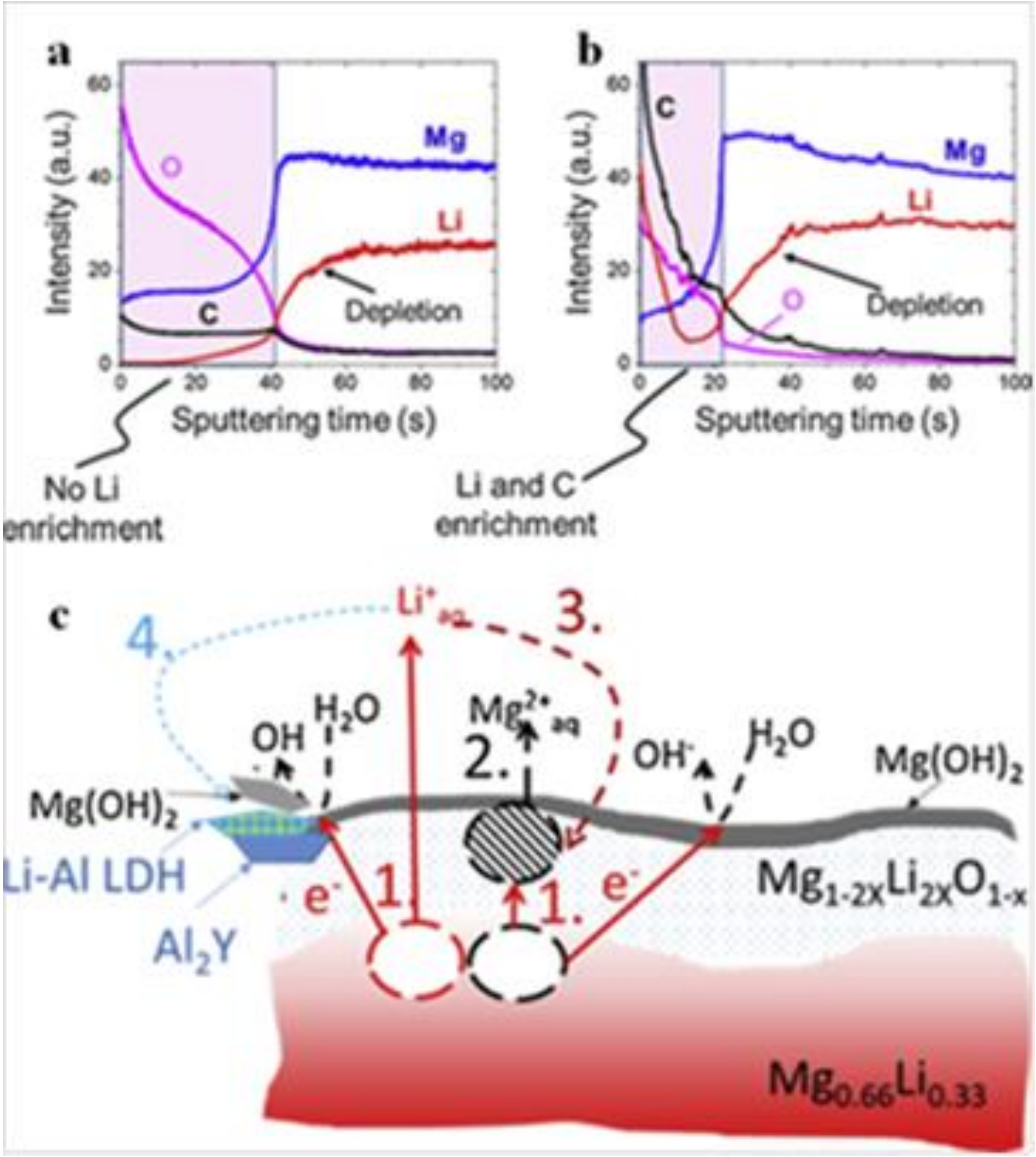

Figure 2.18. GDOES elemental depth profiles obtained for Mg-Li-(Al-Y-Zr) sample after immersion in 0.1 M NaCl (aq) for 20 h: (a) immediately after immersion and (b) air-exposed for 3 h between immersion and GDOES profiling. (c) Schematic representation of steps of aqueous corrosion of Mg-Li alloy [65].

Yan *et al*. [66] showed a re-passivation tendency of the protective Li_2CO_3 film formed on Mg-Li alloys in aqueous solution as anodic dissolution is rapidly suppressed at mechanically-damaged (scribed) sites. They showed that, after scribing, the anodic dissolution rates of Mg and Li increased significantly and then returned to the original pre-scratch value, thus demonstrating a self-healing ability. A similar trend was observed in the OCP transient: an initial drop followed by full recovery of the pre-scribed value.

Li *et al.* [67] studied the increasing Li amount as an alloying element with Mg ranging from (4, 7.5 14 wt. %) on the negative difference effect (cathode activation with increased H_2 gas evolution while under anodic polarization). They showed that the negative difference effect is reduced with an increase in the alloyed Li content. The observed reduction is linked to the microstructure of Mg-Li alloy as it changes from HCP α-Mg to BCC β-Li as the alloyed Li content increases, shown in Figure 2.19A. In addition, Mg-14Li alloy has the lowest cathodic current density (H_2 gas evolution reaction) relative to the other alloys. XPS was used to compare the composition of the surface film of the three alloys formed after immersion in 0.1 M NaCl (aq) for 2 h. As Figure 2.19B shows, the $Mg(OH)_2$ peak is reduced and the Li 1s is strengthened with an increase in the alloyed Li content. The Li 1s peak can be deconvoluted into Li_2CO_3 and LiOH. The C 1s peak intensity is increased, which is attributed to Li_2CO_3. They attributed the improved inhibition to an absence of a cracked surface film.

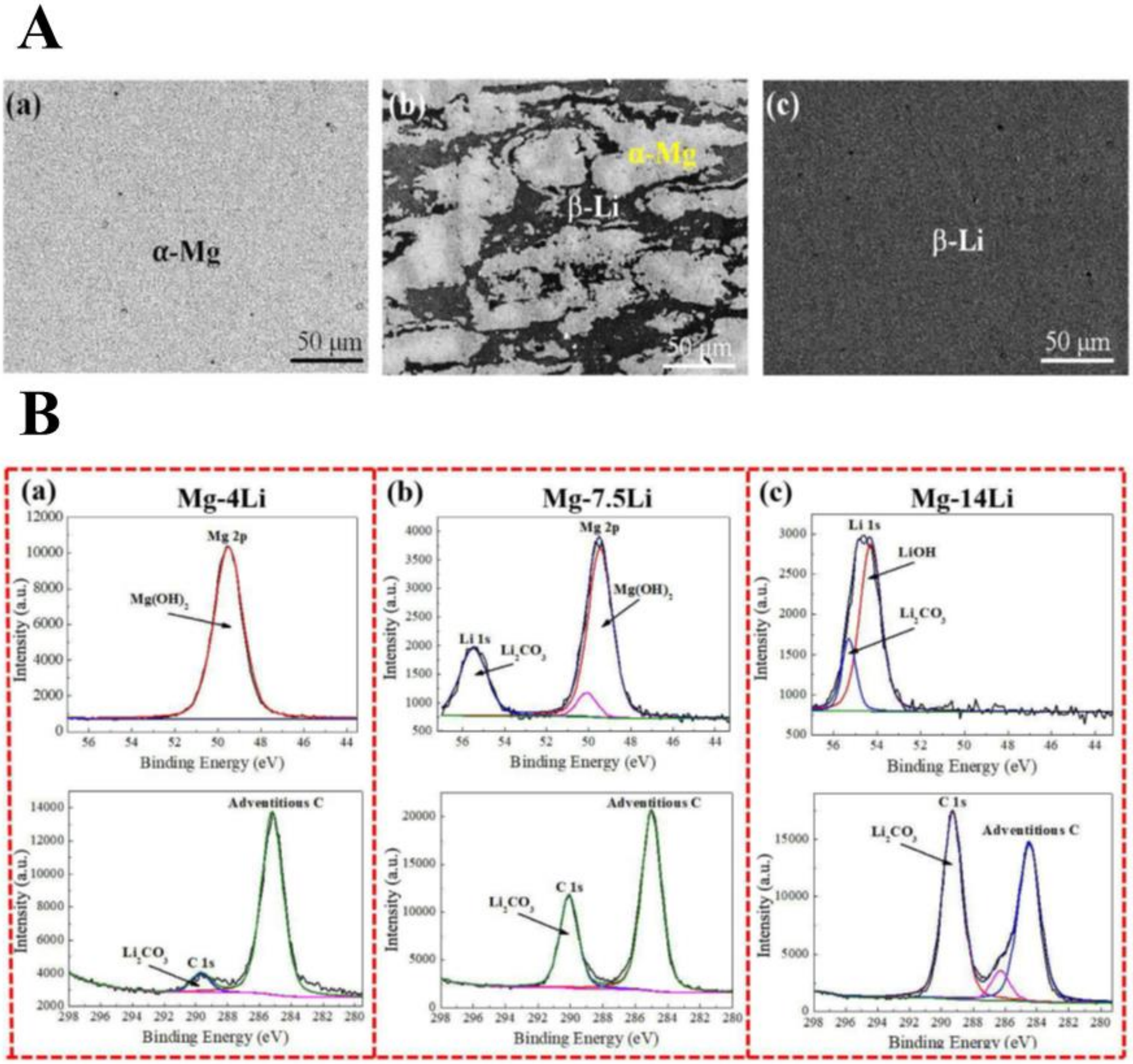

Figure 2.19. (A) SEM images of (a) Mg-4Li, (b) Mg-7.5Li and (c) Mg-14Li alloys. (B) XPS analysis of the surface film on Mg-4Li, Mg-7.5Li and Mg-14Li alloys after immersion in 0.1 M NaCl solution for 2 h [68].

Li *et al*. [68] continued the assessment of Mg-14Li alloy relative to pure Mg. They showed that pure Mg (99.95 wt. %) exhibits less corrosion than Mg-14Li alloy using potentiodynamic polarization, EIS, H_2 evolution and mass loss. They assumed that this contradiction of lower corrosion of pure Mg due to the absence of second phase. The difference is linked to differences in the morphology and composition of intact surface film formed after immersion in 0.1 M NaCl (aq) for 8 h, as shown in Figure 2.20. The thinner intact surface film (~600 nm) formed on pure Mg is composed of oxide/ hydroxide. In contrast, the thicker intact surface film (4 µm) formed on Mg-14Li is comprised of Li_2CO_3, which includes cavities. The latter is argued to be responsible for the increase corrosion observed. They conclude that Li_2CO_3 is not an ideal surface film for the protection of Mg alloys.

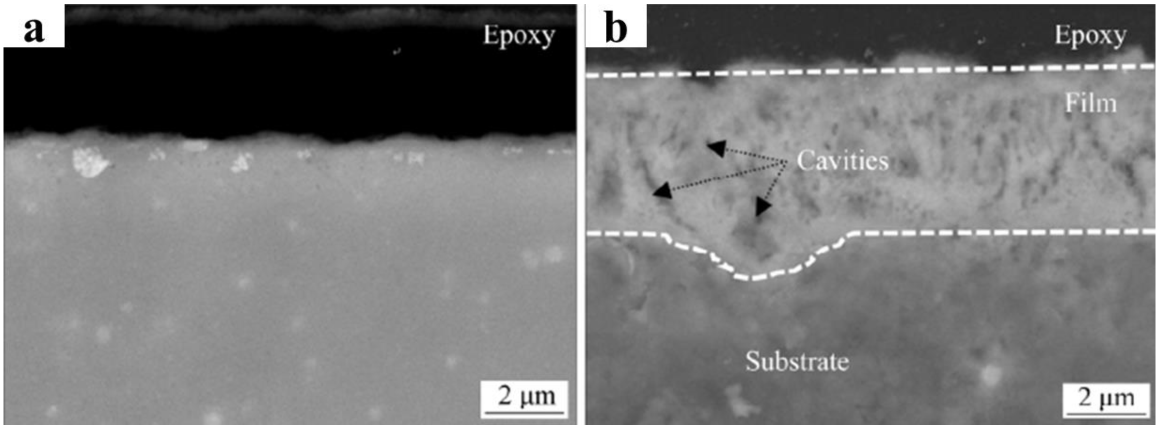

Figure 2.20. Cross-sectional SEM images of the surface film formed (a) pure Mg (b) and Mg-14Li alloy immersed in 0.1 M NaCl (aq) for 8 h [68].

2.6 Leachable Li_2CO_3 Inhibitor for Protective Coatings on Al Alloys

Leachable Li salts have been considered as a promising replacement for the corrosion inhibiting chromate salts for inclusion in protective coatings applied on Al alloys. Visser *et al*. [69] developed a designed using a polyester resin and an aliphatic polyisocyanate that incorporates Li_2CO_3 and other Li salts to improve corrosion control of Al alloy AA2024-T3. Such coatings were artificially damaged to determine the extent of protection provided. Figure 2.21 (b) shows the harmful corrosion effect (formation of white Al-rich oxide/hydroxide corrosion products) when the applied coating has no leachable inhibiting Li salt. However, the scribe shows no evidence corrosion products when the coating included a leachable inhibiting Li carbonate or oxalate, as shown in Figure 2.21 (c and d). Figure 2.22 shows a SEM image of the scribed region in cross-section. The region was covered with a protective deposit about 0.5 to 1.5 μm thick that consisted of three layers, namely: (i) a dense inner layer at metal/coating interface, (ii) a porous intermediate layer and (iii) a porous columnar outer layer. STEM-EELS maps demonstrated the presence of Al, O and Li throughout the deposited layer, which indicates a uniform distribution of Li throughout the entire layer including the dense layer. The STEM-EELS examination revealed that Li ions were leached from the coating into scribe and re-deposited as a polycrystalline outer layer that could be an Al/Li layered double hydroxide and a dense barrier layer that is composed of Li/Al hydroxide to form a protective layer on AA2024-T3 metal surface exposed within the scribed region. However, it remains unclear in which form.

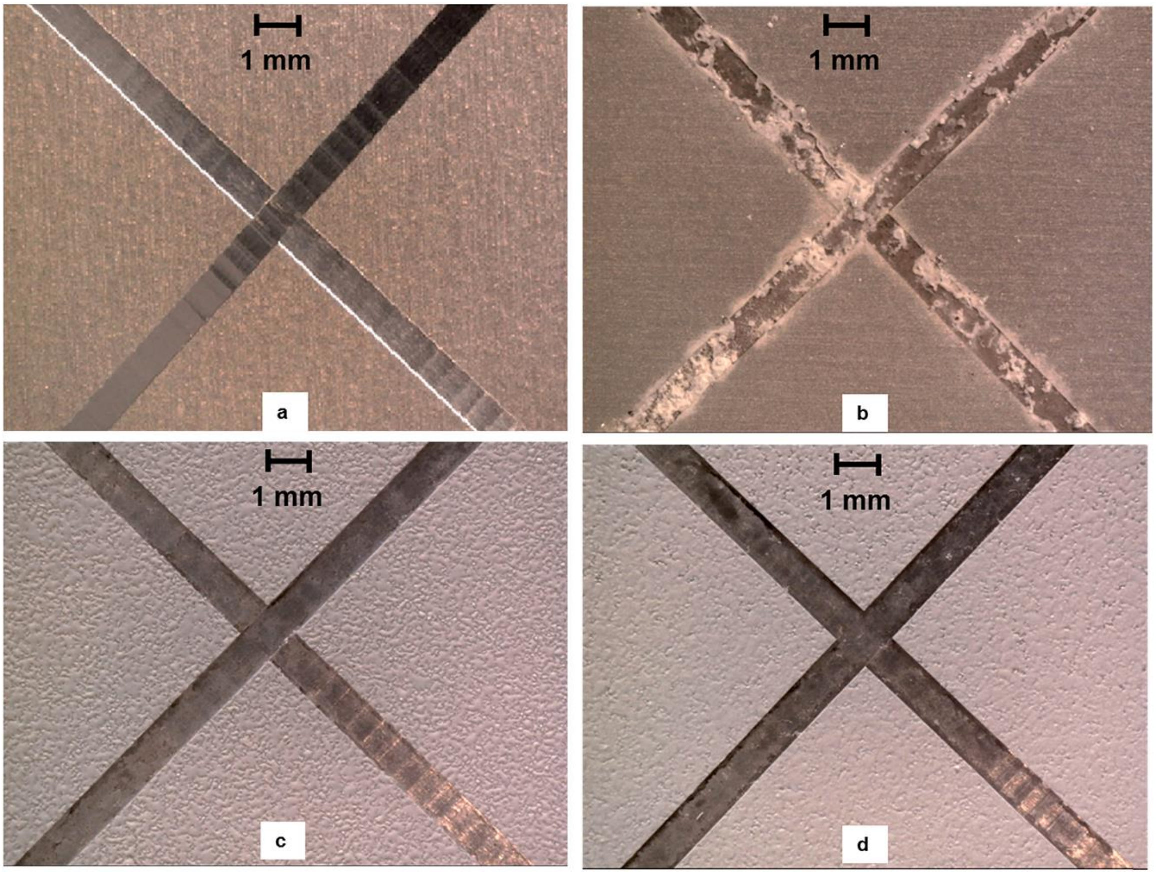

Figure 2.21. Optical images of coated and scribed AA2024-T3 panels before and after 168 h salt spray exposure (ASTM B-117) (a) unexposed (b) no inhibitor, (c) lithium carbonate, and (d) lithium oxalate [69].

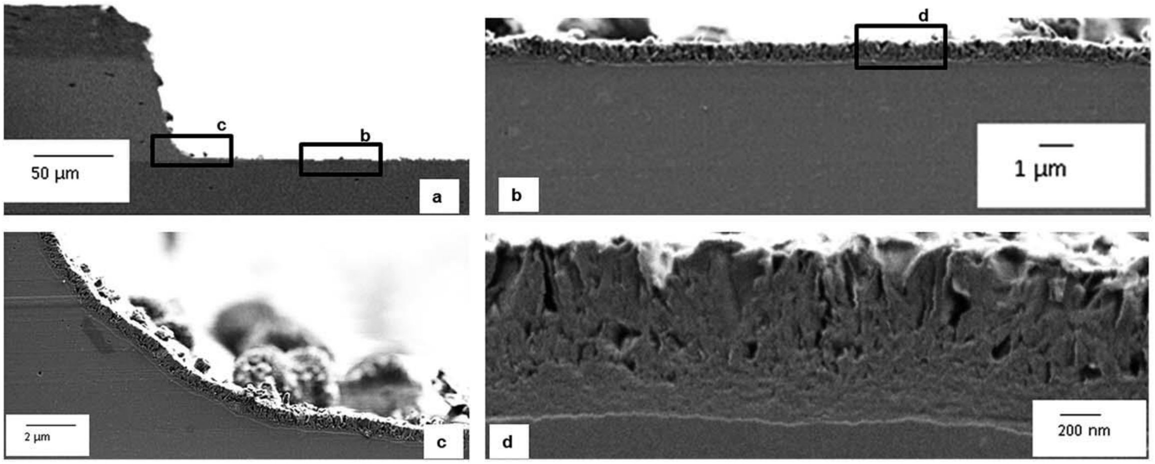

Figure 2.22. SEM cross-cut images of protective layers generated from a Li_2CO_3 loaded coating after 168 h ASTM B-117 exposure (a) scribed area, (b) middle section of the scribe, (c) curved area of bottom of the scribe, (d) detailed morphology of layer (middle section of the scribe) [69].

Meeusen *et al*. [70] studied the effect of incorporating leachable Li_2CO_3 into a polyurethane based model coating for improving corrosion control of AA2024-T3. In addition, to study the active corrosion protective properties of these coatings, an artificial damage site was made of 1 mm width and approximately 100-150 mm depth followed with exposing to the salt spray test according to ASTM B-117 for 168 h. They showed that the polarization resistance of the applied coating with Li_2CO_3 using 0.05 M NaCl (aq) is three times higher than that for the applied coating without Li_2CO_3.

Visser *et al*. [71] elucidated the mechanism for the formation of protective layer produced on AA2024-T3 during immersion in Li_2CO_3 containing NaCl (aq). They revealed that the passive layer formed consists of amorphous inner layer and a crystalline outer layer, with formation involving: (1) oxide thinning, (2) anodic dissolution and film formation and (3) film growth through a competitive growth-dissolution process.

Visser *et al*. [72] also studied the leachability of Li_2CO_3 from a polymer coating to reform rapidly at defect sites providing continuous protective layer. They used polyurethane model coatings with a total pigment volume concentration (PVC) of 30% and respective loadings of 15 and 2.5% PVC Li salt as leachable corrosion inhibitor and demonstrated that this coating provides continuous corrosion protection if the defect location up to 6 mm width. Figure 2.23 shows the effect of different Li_2CO_3 concentration on the scribe corrosion of coated AA2024-T3 after salt spray exposure (ASTM B117). Both coatings show the successful corrosion protection, except for 6 mm scribe that shows some corrosion product with the low Li_2CO_3 content.

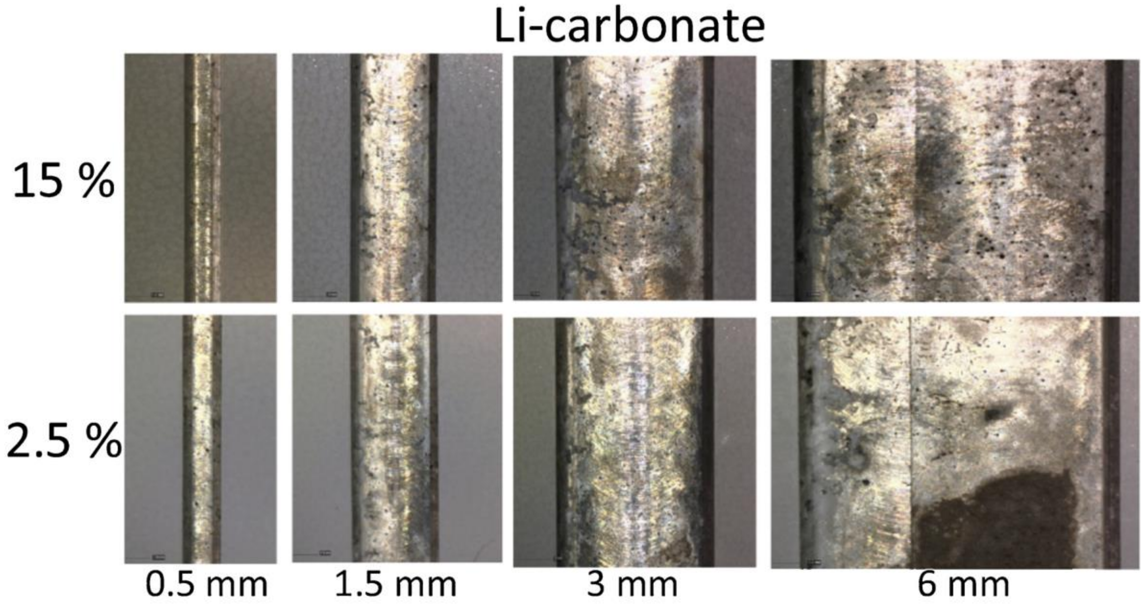

Figure 2.23. Light optical microscopy images of different scribe widths (0.5 mm, 1.5 mm, 3.0 mm and 6.0 mm) in a polymer coating with two Li_2CO_3 contents applied on AA2024-T3 taken after 168 h salt spray exposure [72].

Finally, Visser *et al*. [73] demonstrated the effective corrosion protection of a polymer coating with and without Li_2CO_3 added as a leachable inhibitor on a range of Al alloys namely: AA2024, AA7075, AA5083, and AA6014. SEM and electrochemical measurements revealed that the leachable Li_2CO_3 containing coating provides improved corrosion control through inhibition of corrosion process at defect sites.

Hydrotalcite ($Mg_6Al_2(OH)_{16}CO_3 \times 4H_2O$) conversion coatings applied on Mg alloys to control corrosion have received considerable attention [74]-[76], whereas simple carbonate conversion coatings for the same have received far less attention. Yu *et al*. [77] applied carbonate as a conversion coating for AZ91. They found that via SEM cross sectional area the coating involves a two-layer coating structure. The outer one consists of calcite ($CaCO_3$) and the inner layer consists of hydrotalcite ($Mg_6A_{l2}(OH)_{16}CO_3 \times 4H_2O$). SEM and TEM cross-sectional images confirmed that the hydrotalcite inner layer contained fine particles. The corrosion current density of the coated sample was approximately two orders of magnitude lower than that of the untreated one.

2.7 Research Hypothesis/Objectives

From the synthesis of the literature as presented above, the idea to use leachable Li_2CO_3 as an effective inhibitor as a part of a protective coating applied to Mg alloy sheet metal for improved corrosion control in automotive applications shows significant promise. The overarching hypothesis is that dissolved Li_2CO_3 can impart effectively inhibit corrosion of Mg alloy sheet metal when immersed in NaCl (aq) by combining the inhibiting capability of dissolved Li^+, albeit based on an alloyed Li effect, and carbonate ($CO_3^{2-}/HCO_3^-/OH^-$) on both anode and cathode kinetics and protective surface film formation.

Arguably, the major scientific question here is how the localized filament-like corrosion, and associated activation (anode and cathode), is controlled to yield effective inhibition. Key aspects in need of study include, intact surface film stability, anode and cathode kinetics and surface film formation during anodic (and associated cathodic) activation. Consequently, the research objectives were defined as follows:

i. Determine the extent to which Li_2CO_3 (aq) serves as an effective corrosion inhibitor for AZ31B (H24 temper) sheet metal when immersed in 0.1 M NaCl (aq) using bulk immersion, conventional and scanning electrochemical measurements in combination with an XPS analysis of the intact surface film formed.

ii. Determine the combinatory effects of dissolved dissolved Li^+ and carbonate (CO_3^{2-}/HCO_3^-/OH^-) on corrosion inhibition of ZEK100 (O-temper) sheet metal when immersed in 0.1 M NaCl (aq) using bulk immersion and conventional electrochemical measurements in combination with a TEM analyses of surface films formed during node activation (polarization).

iii. Demonstrate the capability of a leachable Li_2CO_3 (s) surface pre-treatment coating to inhibit corrosion of ZEK100 alloy sheet metal product when immersed in 0.1 M NaCl (aq), relative to the bare surface and one coated with the preferred surface pre-treatment (Bonderite® MNT 5200), using conventional electrochemical measurements, including EIS, in combination with SEM and TEM analysis of the starting surface coatings.

2.8 References

[1] T. Skszek, “Demonstration Project for a Multi-Material Lightweight Prototype Vehicle as Part of the Clean Energy Dialogue with Canada,” United States: N. p., 2015. Web. doi:10.2172/1332277.

[2] Krebs HM, "The microstructure and corrosion performance of AZ31B-H24 magnesium alloy sheet" The University of Manchester (United Kingdom), 2017.

[3] S. W. Lee, S. Kim, and S. H. Park, “Microstructural characteristics of AZ31 alloys rolled at room and cryogenic temperatures and their variation during annealing,” *J. Magnes. Alloy.*, vol. 8, no. 2, pp. 537–545, 2020, doi: 10.1016/j.jma.2020.03.003.

[4] Mallick, Pankaj K., ed. Materials, design and manufacturing for lightweight vehicles. Woodhead publishing, 2020.

[5] E. Ghali, W. Dietzel, and K. U. Kainer, “General and localized corrosion of magnesium alloys: A critical review,” *J. Mater. Eng. Perform.*, vol. 22, no. 10, pp. 2875–2891, 2013, doi: 10.1007/s11665-013-0730-9.

[6] Kurukuri S, Worswick MJ, Bardelcik A, Mishra RK and Carter JT., “Constitutive Behavior of Commercial Grade ZEK100 Magnesium Alloy Sheet over a Wide Range of Strain Rates,” *Metall. Mater. Trans.*, vol. 45, no. 8, pp. 3321–3337, 2014, doi: 10.1007/s11661-014-2300-7.

[7] Melia, M.A., Steiner, P., Birbilis, N., Fitz-Gerald, J.M. and Scully, J.R, “Excimer Laser Surface Modification of AZ31B-H24 for Improved Corrosion Resistance,” *Corrosion*, vol. 72, no. 1, pp. 95-109, 2016, doi.org/10.5006/1851.

[8] Z. P. Cano, M. Danaie, J. R. Kish, J. R. Mcdermid, G. A. Botton, and G. Williams, “Physical Characterization of Cathodically-Activated Corrosion Filaments on Magnesium Alloy AZ31B,” *Corrosion*, vol. 71, no. 2, pp. 146–159, 2015, doi.org/10.5006/1384.

[9] G. Ben Hamu, D. Eliezer, and L. Wagner, “The relation between severe plastic

deformation microstructure and corrosion behavior of AZ31 magnesium alloy," *Journal of alloys and compounds*, vol. 468, no. 1-2, pp. 222–229, 2009, doi: 10.1016/j.jallcom.2008.01.084.

[10] Melia, M.A., Steiner, P., Birbilis, N., Fitz-Gerald, J.M. and Scully, J.R, "Excimer Laser Surface Modification of AZ31B-H24 for Improved Corrosion Resistance," *Corrosion*, vol. 72, no. 1, pp. 95-109, 2016, doi.org/10.5006/1851.

[11] R. M. Asmussen, W. J. Binns, P. Jakupi, and D. Shoesmith, "The Influence of Microstructure on the Corrosion of Magnesium Alloy ZEK100," *Corrosion*, vol. 9312, no. 2, pp. 242–254, 2015, doi.org/10.5006/1387.

[12] A. Javaid and F. Czerwinski, "Effect of hot rolling on microstructure and properties of the ZEK100 alloy," *J. Magnes. Alloy.*, vol. 7, no. 1, pp. 27–37, 2019, doi: 10.1016/j.jma.2019.02.001.

[13] A. Javaid, A. Hadadzadeh, and F. Czerwinski, "Solidification behavior of dilute Mg-Zn-Nd alloys," *J. Alloys Compd.*, vol. 782, pp. 132–148, 2019, doi: 10.1016/j.jallcom.2018.12.134.

[14] Z. P. Cano, J. R. McDermid, and J. R. Kish, "Cathodic Activity of Corrosion Filaments Formed on Mg Alloy AM30," *J. Electrochem. Soc.*, vol. 162, no. 14, pp. C732–C740, 2015, doi: 10.1149/2.0381514jes.

[15] M. Taheri, J. R. Kish, N. Birbilis, M. Danaie, E. A. Mcnally, and J. R. Mcdermid, "Towards a Physical Description for the Origin of Enhanced Catalytic Activity of Corroding Magnesium Surfaces," *Electrochim. Acta*, vol. 116, pp. 396–403, 2014, doi: 10.1016/j.electacta.2013.11.086.

[16] J. R. Kish, Y. Hu, J. Li, W. Zheng, and J. R. Mcdermid, "Technical Note : Examination of Focused Ion Beam-Sectioned Surface Films Formed on AM60B Mg Alloy in an Aqueous Saline Solution," *Corrosion*, vol. 68, no. 6, pp. 468–474,

2012, doi.org/10.5006/i0010-9312-68-6-468.

[17] G. Williams, H. A. L. Dafydd, and R. Grace, “The localised corrosion of Mg alloy AZ31 in chloride containing electrolyte studied by a scanning vibrating electrode technique,” *Electrochim. Acta*, vol. 109, pp. 489–501, 2013, doi: 10.1016/j.electacta.2013.07.134.

[18] Z. P. Cano, J. R. Kish, and J. R. McDermid, “On the Evolution of Cathodic Activity during Corrosion of Magnesium Alloy AZ31B in a Dilute NaCl Solution,” *J. Electrochem. Soc.*, vol. 163, no. 3, pp. C62–C68, 2016, doi: 10.1149/2.0151603jes.

[19] M. A. Melia, T. W. Cain, B. F. Briglia, J. R. Scully, and J. M. Fitz-Gerald, “Evolution of the Corrosion Morphology on AZ31B Tracked Electrochemically and by In Situ Microscopy in Chloride-Containing Media,” *Jom*, vol. 69, no. 11, pp. 2322–2327, 2017, doi: 10.1007/s11837-017-2377-8.

[20] L. Bushi, “Comparative LCA Study of the Magna / Ford MMLV Concept Vehicle Design Comparative LCA Study of Lightweight Auto parts of MMLV Mach-I Vehicle as per ISO 14040 / 44 LCA Standards and CSA Group 2014 LCA Guidance Document for Auto Parts,” 2016.

[21] Krebs, H.M., Chirazi, A., Lechner, L., Gelb, J., Zhou, X., Thompson, G.E. and Withers, P.J, “Time-Lapse Correlative 3D Imaging Applied to the Corrosion Study of AZ31 Mg Alloy in a Saline Environment,” *Front. Mater. Process. Appl. Res.Technol.*, Springer, Singapore, pp. 165−177, 2018, doi: 10.1007/978-981-10-4819-7_15.

[22] L. G. Bland, N. Birbilis, and J. R. Scully, “Exploring the Effects of Intermetallic Particle Size and Spacing on the Corrosion of Mg-Al Alloys Using Model Electrodes,” *J. Electrochem. Soc.*, vol. 163, no. 14, pp. C895–C906, 2016, doi: 10.1149/2.1151614jes.

[23] D. Rossouw, D. Fu, D. N. Leonard, M. P. Brady, G. A. Botton, and J. R. Kish, "Characterization of localized filament corrosion products at the anodic head on a model Mg-Zn-Zr alloy surface," *Corrosion*, vol. 73, no. 5, pp. 518–525, 2017, doi: 10.5006/2268.

[24] S. Fajardo, C. F. Glover, G. Williams, and G. S. Frankel, "The evolution of anodic hydrogen on high purity magnesium in acidic buffer solution," *Corrosion*, vol. 73, no. 5, pp. 482–493, 2017, doi: 10.5006/2247.

[25] E. Michailidou, H. N. McMurray, and G. Williams, "Quantifying the Role of Transition Metal Electrodeposition in the Cathodic Activation of Corroding Magnesium," *J. Electrochem. Soc.*, vol. 165, no. 5, pp. C195–C205, 2018, doi: 10.1149/2.0251805jes.

[26] S. Thomas, N. V. Medhekar, G. S. Frankel, and N. Birbilis, "Corrosion mechanism and hydrogen evolution on Mg," *Curr. Opin. Solid State Mater. Sci.*, vol. 19, no. 2, pp. 85–94, 2015, doi: 10.1016/j.cossms.2014.09.005.

[27] G. S. Frankel, A. Samaniego, and N. Birbilis, "Evolution of hydrogen at dissolving magnesium surfaces," *Corros. Sci.*, vol. 70, pp. 104–111, 2013, doi.org/10.1016/j.corsci.2013.01.017.

[28] T. Cain, S. B. Madden, N. Birbilis, and J. R. Scully, "Evidence of the Enrichment of Transition Metal Elements on Corroding Magnesium Surfaces Using Rutherford Backscattering Spectrometry," *J. Electrochem. Soc.*, vol. 162, no. 6, pp. C228–C237, 2015, doi: 10.1149/2.0541506jes.

[29] D. Höche, C. Blawert, S. V. Lamaka, N. Scharnagl, C. Mendis, and M. L. Zheludkevich, "The effect of iron re-deposition on the corrosion of impurity-containing magnesium," *Phys. Chem. Chem. Phys.*, vol. 18, no. 2, pp. 1279–1291, 2015, doi: 10.1039/c5cp05577f.

[30] J. Li, W. Sun, B. Hurley, A. A. Luo, and R. G. Buchheit, "Cu redistribution study

during the corrosion of AZ91 using a rotating ring-disk collection experiment," *Corros. Sci.*, vol. 112, pp. 760–764, 2016, doi: 10.1016/j.corsci.2016.08.011.

[31] S. H. Salleh, S. Thomas, J. A. Yuwono, K. Venkatesan, and N. Birbilis, "Enhanced hydrogen evolution on Mg $(OH)_2$ covered Mg surfaces," *Electrochim. Acta*, vol. 161, pp. 144–152, 2015, doi: 10.1016/j.electacta.2015.02.079.

[32] W. J. Binns, F. Zargarzadah, V. Dehnavi, J. Chen, J. J. Noël, and D. W. Shoesmith, "Physical and Electrochemical Evidence for the Role of a Mg Hydride Species in Mg Alloy Corrosion," *Corrosion*, vol. 75, no. 1, pp. 58−68, 2019, doi.org/10.5006/2918.

[33] A. Samaniego, I. Llorente, and S. Feliu, "Combined effect of composition and surface condition on corrosion behaviour of magnesium alloys AZ31 and AZ61," *Corros. Sci.*, vol. 68, pp. 66–71, 2013, doi: 10.1016/j.corsci.2012.10.034.

[34] D. Thirumalaikumarasamy, K. Shanmugam, and V. Balasubramanian, "Comparison of the corrosion behaviour of AZ31B magnesium alloy under immersion test and potentiodynamic polarization test in NaCl solution," *J. Magnes. Alloy.*, vol. 2, no. 1, pp. 36–49, 2014, doi: 10.1016/j.jma.2014.01.004.

[35] C. Kousis, N. McMurray, P. Keil, and G. Williams, "The Influence of Chloride Ion Concentration on the Localized Corrosion of E717 Magnesium Alloy," *Corrosion*, vol. 77, no. 2, pp. 156–167, 2021, doi: 10.5006/3601.

[36] G. G. Wang, K. Stewart, R. Berkmortel, and J. I. Skar, "Corrosion prevention for external magnesium automotive components," *SAE Tech. Pap.*, vol. 110, pp. 397–405, 2001, doi: 10.4271/2001-01-0421.

[37] S. Song, W. D. Shen, M. H. Liu, and G. L. Song, "Corrosion study of new surface treatment/ coating for AZ31B magnesium alloy," *Surf. Eng.*, vol. 28, no. 7, pp. 486–490, 2012, doi: 10.1179/1743294411Y.0000000056.

[38] Logan, S.D., Forsmark, J.H. and Osborne, R, "Development and Demonstration of a Magnesium-Intensive Vehicle Front-End Substructure," United States Automotive Materials Partnership LLC, Southfield, MI (United States), 2016.

[39] S. Song, G. L. Song, W. Shen, and M. Liu, "Corrosion and electrochemical evaluation of coated magnesium alloys," *Corrosion*, vol. 68, no. 1, pp. 1–12, 2012, doi: 10.5006/1.3674295.

[40] *The Handbook of Chemistry and Physics, 82nd Edition by David R. Lide*. CRC Press LLC, 2002.

[41] G. Williams, H. N. McMurray, and R. Grace, "Inhibition of magnesium localised corrosion in chloride containing electrolyte," *Electrochim. Acta*, vol. 55, no. 27, pp. 7824–7833, 2010, doi: 10.1016/j.electacta.2010.03.023.

[42] G. Williams, R. Grace, and R. M. Woods, "Inhibition of the localized corrosion of mg alloy AZ31 in chloride containing electrolyte," *Corrosion*, vol. 71, no. 2, pp. 184–198, 2015, doi: 10.5006/1376.

[43] Brady, M.P., Leonard, D.N., Meyer III, H.M., Thomson, J.K., Unocic, K.A., Elsentriecy, H.H., Song, G.L., Kitchen, K. and Davis, B, "Advanced characterization study of commercial conversion and electrocoating structures on magnesium alloys AZ31B and ZE10A," *Surf. Coatings Technol.*, vol. 294, pp. 164–176, 2016, doi: 10.1016/j.surfcoat.2016.03.066.

[44] J. K. Lin and J. Y. Uan, "Formation of Mg,Al-hydrotalcite conversion coating on Mg alloy in aqueous HCO_3^-/CO_3^{2-} and corresponding protection against corrosion by the coating," *Corros. Sci.*, vol. 51, no. 5, pp. 1181–1188, 2009, doi: 10.1016/j.corsci.2009.02.007.

[45] J. Chen, Y. Song, D. Shan, and E. H. Han, "In situ growth of Mg-Al hydrotalcite

conversion film on AZ31 magnesium alloy," *Corros. Sci.*, vol. 53, no. 10, pp. 3281–3288, 2011, doi: 10.1016/j.corsci.2011.06.003.

[46] R. C. Zeng, Z. G. Liu, F. Zhang, S. Q. Li, H. Z. Cui, and E. H. Han, "Corrosion of molybdate intercalated hydrotalcite coating on AZ31 Mg alloy," *J. Mater. Chem. A*, vol. 2, no. 32, pp. 13049–13057, 2014, doi: 10.1039/c4ta01341g.

[47] V. Zahedi Asl, J. Zhao, M. J. Anjum, S. Wei, W. Wang, and Z. Zhao, "The effect of cerium cation on the microstructure and anti-corrosion performance of LDH conversion coatings on AZ31 magnesium alloy," *J. Alloys Compd.*, vol. 821, p. 153248, 2020, doi: 10.1016/j.jallcom.2019.153248.

[48] Zhang, G., Jiang, E., Wu, L., Ma, W., Yang, H., Tang, A. and Pan, F., "Corrosion protection properties of different inhibitors containing PEO/LDHs composite coating on magnesium alloy AZ31," *Sci. Rep.*, vol. 11, no. 1, pp. 1–14, 2021, doi: 10.1038/s41598-021-81029-6.

[49] J. K. E. Tan, P. Balan, and N. Birbilis, "Advances in LDH coatings on Mg alloys for biomedical applications: A corrosion perspective," *Appl. Clay Sci.*, vol. 202, pp. 105948, 2021, doi: 10.1016/j.clay.2020.105948.

[50] Tabish, M., Yasin, G., Anjum, M.J., Malik, M.U., Zhao, J., Yang, Q., Manzoor, S., Murtaza, H. and Khan, W.Q., "Reviewing the current status of layered double hydroxide-based smart nanocontainers for corrosion inhibiting applications," *J. Mater. Res. Technol.*, vol. 10, pp. 390‒421, 2021, doi: 10.1016/j.jmrt.2020.12.025.

[51] H. Gao, Q. Li, Y. Dai, F. Luo, and H. X. Zhang, "High efficiency corrosion inhibitor 8-hydroxyquinoline and its synergistic effect with sodium dodecylbenzenesulphonate on AZ91D magnesium alloy," *Corros. Sci.*, vol. 52, no. 5, pp. 1603–1609, 2010, doi: 10.1016/j.corsci.2010.01.033.

[52] D. Eaves, G. Williams, and H. N. McMurray, “Inhibition of self-corrosion in magnesium by poisoning hydrogen recombination on iron impurities,” *Electrochim. Acta*, vol. 79, pp. 1–7, 2012, doi: 10.1016/j.electacta.2012.05.148.

[53] A. Frignani, V. Grassi, F. Zanotto, and F. Zucchi, “Inhibition of AZ31 Mg alloy corrosion by anionic surfactants,” *Corros. Sci.*, vol. 63, pp. 29–39, 2012, doi: 10.1016/j.corsci.2012.05.012.

[54] N. Dinodi and A. N. Shetty, “Alkyl carboxylates as efficient and green inhibitors of magnesium alloy ze41 corrosion in aqueous salt solution,” *Corros. Sci.*, vol. 85, pp. 411–427, 2014, doi: 10.1016/j.corsci.2014.04.052.

[55] S. V. Lamaka, D. Höche, R. P. Petrauskas, C. Blawert, and M. L. Zheludkevich, “A new concept for corrosion inhibition of magnesium: Suppression of iron re-deposition,” *Electrochem. commun.*, vol. 62, pp. 5–8, 2016, doi: 10.1016/j.elecom.2015.10.023.

[56] S. V. Lamaka, B. Vaghefinazari, D. Mei, R. P. Petrauskas, D. Höche, and M. L. Zheludkevich, “Comprehensive screening of Mg corrosion inhibitors,” *Corros. Sci.*, vol. 128, pp. 224–240, 2017, doi: 10.1016/j.corsci.2017.07.011.

[57] Z. Feng, B. Hurley, M. Zhu, Z. Yang, J. Hwang, and R. Buchheit, “ Corrosion Inhibition of AZ31 Mg Alloy by Aqueous Selenite (SeO_3^{2-}) ,” *J. Electrochem. Soc.*, vol. 166, no. 14, pp. C520–C529, 2019, doi: 10.1149/2.0911914jes.

[58] L. Prince, M. A. Rousseau, X. Noirfalise, L. Dangreau, L. B. Coelho, and M. G. Olivier, “Inhibitive effect of sodium carbonate on corrosion of AZ31 magnesium alloy in NaCl solution,” *Corros. Sci.*, vol. 179, pp. 109131, 2021, doi: 10.1016/j.corsci.2020.109131.

[59] E. Gulbrandsen, “Anodic behaviour of Mg in HCO_3^-/CO_3^{2-} buffer solutions. Quasi-steady measurements,” *Electrochim. Acta*, vol. 37, no. 8, pp. 1403−1412,

1992, doi.org/10.1016/0013-4686(92)87014-Q.

[60] B. Raza and S. Moon, "Electrochemical Properties of Air-Formed Oxide Film-Covered AZ31 Mg Alloy in Aqueous Solutions Containing Various Anions," *J. Korean Inst. Surf. Eng.*, vol. 50, no. 3, pp. 147−154, 2017, doi.org/10.5695/JKISE.2017.50.3.147

[61] Esmaily, M., Svensson, J.E., Fajardo, S., Birbilis, N., Frankel, G.S., Virtanen, S., Arrabal, R., Thomas, S. and Johansson, L.G., "Fundamentals and advances in magnesium alloy corrosion," *Prog. Mater. Sci.*, vol. 89, pp. 92−193, 2017, doi: 10.1016/j.pmatsci.2017.04.011.

[62] X. B. Chen, H. Y. Yang, T. B. Abbott, M. A. Easton, and N. Birbilis, "Magnesium: Engineering the surface," *Jom*, vol. 64, no. 6, pp. 650–656, 2012, doi: 10.1007/s11837-012-0331-3.

[63] K. Gusieva, C. H. J. Davies, J. R. Scully, and N. Birbilis, "Corrosion of magnesium alloys: The role of alloying," *Int. Mater. Rev.*, vol. 60, no. 3, pp. 169–194, 2015, doi: 10.1179/1743280414Y.0000000046.

[64] Xu, W., Birbilis, N., Sha, G., Wang, Y., Daniels, J.E., Xiao, Y. and Ferry, M., "Ahigh-specific-strength and corrosion-resistant magnesium alloy," *Nat. Mater.*, vol. 14, pp. 1229−1236, 2015, doi: 10.1038/NMAT4435.

[65] Yan, Y.M., Maltseva, A., Zhou, P., Li, X.J., Zeng, Z.R., Gharbi, O., Ogle, K., La Haye, M., Vaudescal, M., Esmaily, M. and Birbilis, N., "On the in-situ aqueous stability of an Mg-Li- (Al-Y-Zr) alloy : Role of Li," vol. 164, pp. 108342, 2020, doi: 10.1016/j.corsci.2019.108342.

[66] Yan, Y., Zhou, P., Gharbi, O., Zeng, Z., Chen, X., Volovitch, P., Ogle, K. and Birbilis, N, "Investigating ion release using inline ICP during in situ scratch testing of an Mg-Li (-Al-Y-Zr) alloy," *Electrochem. commun.*, vol. 99, pp. 46–50, 2019, doi: 10.1016/j.elecom.2019.01.001.

[67] C. Q. Li, D. K. Xu, Z. R. Zhang, and E. H. Han, "Influence of the lithium content on the negative difference effect of Mg-Li alloys," *J. Mater. Sci. Technol.*, vol. 57, pp. 138–145, 2020, doi: 10.1016/j.jmst.2020.03.046.

[68] C. qiang LI, Z. pei TONG, Y. bin HE, H. pei HUANG, Y. DONG, and P. ZHANG, "Comparison on corrosion resistance and surface film of pure Mg and Mg−14Li alloy," *Trans. Nonferrous Met. Soc. China (English Ed.*, vol. 30, no. 9, pp. 2413–2423, 2020, doi: 10.1016/S1003-6326(20)65388-2.

[69] Visser, P., Liu, Y., Zhou, X., Hashimoto, T., Thompson, G.E., Lyon, S.B., van der Ven, L.G., Mol, A.J. and Terryn, H.A, "The corrosion protection of AA2024-T3 aluminium alloy by leaching of lithium-containing salts from organic coatings," *R. Soc. Chem.*, vol. 180, pp. 511–526, 2015, doi.org/10.1039/C4FD00237G.

[70] M. Meeusen, P. Visser, L. Fernández Macía, A. Hubin, H. Terryn, and J. M. C. Mol, "The use of odd random phase electrochemical impedance spectroscopy to study lithium-based corrosion inhibition by active protective coatings," *Electrochim. Acta*, vol. 278, pp. 363–373, 2018, doi: 10.1016/j.electacta.2018.05.036.

[71] P. Visser, Y. Gonzalez-Garcia, J. M. C. Mol, and H. Terryn, "Mechanism of Passive Layer Formation on AA2024-T3 from Alkaline Lithium Carbonate Solutions in the Presence of Sodium Chloride," *J. Electrochem. Soc.*, vol. 165, no. 2, pp. C60–C70, 2018, doi: 10.1149/2.1011802jes.

[72] Visser P, Marcoen K, Trindade GF, Abel ML, Watts JF, Hauffman T, Mol JM, Terryn H.,

"The chemical throwing power of lithium-based inhibitors from organic coatings on AA2024-T3," *Corros. Sci.*, vol. 150, pp. 194–206, 2019, doi: 10.1016/j.corsci.2019.02.009.

[73] P. Visser, H. Terryn, and J. M. C. Mol, "Active corrosion protection of various aluminium alloys by lithium-leaching coatings," *Surf. Interface Anal.*, vol. 51, no. 12, pp. 1276–1287, 2019, doi: 10.1002/sia.6638.

[74] J. E. Gray and B. Luan, "Protective coatings on magnesium and its alloys — a critical review," *J. Alloys Compd.*, vol. 336, no. 1-2, pp. 88−113, 2002, doi.org/10.1016/S0925-8388(01)01899-0

[75] X. B. Chen, N. Birbilis, and T. B. Abbott, "Review of corrosion-resistant conversion coatings for magnesium and its alloys," *Corrosion*, vol. 67, no. 3, pp. 1–16, 2011, doi: 10.5006/1.3563639.

[76] J. Wang, X. Pang, and H. Jahed, "Surface protection of Mg alloys in automotive applications: A review," *AIMS Mater. Sci.*, vol. 6, no. 4, pp. 567–600, 2019, doi: 10.3934/matersci.2019.4.567.

[77] B. L. Yu, X. L. Pan, and J. Y. Uan, "Enhancement of corrosion resistance of Mg-9 wt.% Al-1 wt.% Zn alloy by a calcite ($CaCO_3$) conversion hard coating," *Corros. Sci.*, vol. 52, no. 5, pp. 1874–1878, 2010, doi: 10.1016/j.corsci.2010.01.014.

Chapter 3

Inhibiting Corrosion of Mg Alloy AZ31B-H24 Sheet Metal with Lithium Carbonate

B. Zaghloul[*], C.F. Glover[**], J.R. Scully[**], J.R. Kish[‡, *]

[*]Department of Materials Science and Engineering, McMaster University, Hamilton, ON, Canada
[**]Department of Materials Science and Engineering, University of Virginia, Charlottesville, VA

[‡]Corresponding Author: (905) 525-9140, extension 21492, kishjr@mcmaster.ca

(1) UNS numbers are listed in Metals & Alloys in the Unified Numbering System, published by the Society of Automotive Engineers (SAE International) and cosponsored by ASTM International.

Submitted on 26 June 2020. Published on 3 October 2020

Reprinted with Permission from Corrosion Journal Published by NACE International

3.1 Abstract

The objective of this work was to determine the effectiveness of dissolved Li_2CO_3 as a corrosion inhibitor for AZ31B-H24 sheet metal when immersed in NaCl (aq) at ambient temperature. Corrosion rates were determined by gravimetric mass loss and volumetric H_2 evolution measurements and the observed inhibition was investigated further using potentiodynamic polarization, scanning vibrating electrode technique, and x-ray photoelectron surface analytical measurements. It is shown that dissolved Li_2CO_3 significantly inhibits corrosion as it reduces the corrosion rate by a factor of 10. The manner in which inhibition is achieved is rationalized by the role played by the surface film produced during corrosion in inhibiting both the anode (anodic dissolution) and cathode (H_2 evolution) kinetics. Inhibition involves the suppression of the filament-like corrosion mode, albeit on the macroscale, and associated cathodic activation. By process of elimination, it is proposed that the Li^+ cations play a key role in inhibiting the anodic dissolution and associated cathodic activation that is required to drive the filament-like corrosion.

Keywords: aqueous environments, corrosion inhibitor, film, magnesium

3.2 Introduction

As a sheet metal product, Mg alloy AZ31B (Mg-3Al-1Zn; UNS M11311(1)) remains of great interest to the automotive industry with its lightweighting potential when incorporated into multimaterial structural assemblies.[1-2] However, the alloy is prone to corrosion, particularly when in contact with aqueous chloride-containing solutions, which has stifled increased utilization to a large extent.[3-5] The corrosion of AZ31B involves a rather unique localized filament-like mode that is driven by the so-called cathodic activation (enhanced H_2 gas evolution) of the dissolving surface.[6-10] Local anodes initiate, likely at secondary phase particles that serve as active cathodes,[11-12] and propagate laterally across the filmed surface (akin to a filament) driven by cathodic activation, mostly alongside anodic dissolution at the head, but with some contribution from the porous oxide/hydroxide corrosion products left behind in the tail.[13-15] The source of cathodic activation has been strongly debated,[16] with current proposed theories involving an active cathode such as the bare dissolving surface itself,[17] noble metal enrichment due to selective dissolution of Mg[18-20] or redeposition, [21-22] formation of $Mg(OH)_2$ as a corrosion product,[23] and the formation and subsequent dissolution of MgH_2.[24] Application of a multilayered protective coating scheme, including a pretreatment inner layer and a polymer sealant over-layer as a minimum, is currently the preferred corrosion control strategy within the automotive industry.[4,25-26] Inorganic-based coatings applied either through chemical conversion or electrolytic deposition processes have been extensively researched for this purpose, without any one particular combination of processes being a clear cut favorite.[25-28] Li alloying is known to significantly stifle the anodic kinetics of the

Mg matrix, with no concomitant effect on the cathodic kinetics, which is a unique kinetic combination not observed in other Mg alloys.[29] The improved corrosion control is attributed to the formation of a more protective surface film, the exact composition of which is currently being delineated. Initially, it was suggested that a protective Li_2CO_3 outer layer formed during ambient atmosphere exposure was responsible,[29] as supported by results from x-ray photoelectron spectroscopy (XPS), grazing incident x-ray diffraction (GIXRD), and transmission electron microscopy (TEM) and associated techniques.[29-31] However, the air-formed Li_2CO_3 layer has been shown very recently, using a suite of surface analysis techniques, to dissolve during bulk immersion in NaCl (aq),[32] which is expected based on a chemical stability analysis for the corrosion of Mg-Li alloys.[33] Yan, et al.,[32] argue that the improved corrosion control stems from the formation of a Li-doped MgO inner layer within the intact surface film, which exhibits improved chemical stability relative to MgO, and of a Li-Al layered double hydroxide (LDH) on active cathode sites associated with secondary phase particles; both formations being effective in inhibiting cathodic activation. Regardless of the controlling Li film chemistry, the protective surface film that forms exhibits a self-healing capability when mechanically damaged.[34] Thus, there is merit in the idea of utilizing the improved corrosion control imparted by a Li and/or Li_2CO_3 surface film as an applied self-healing pretreatment coating for Mg alloys rather than relying on Li alloying for its formation. Li_2CO_3 has been added as a leachable inhibitor additive in coating schemes applied to Al alloys for improved corrosion control.[35-37] Dissolved Li ions promote the fast formation of a protective multilayered film comprised of Al, Li, and O.[38-40]

The objective of this work was to determine the extent to which dissolved Li_2CO_3 (aq) inhibits corrosion of AZ31B-H24 when immersed in NaCl (aq) as a precursor feasibility study to applying Li_2CO_3 (s) as a pretreatment layer within a protective coating scheme. The experimental approach combines electrochemical polarization, scanning vibrating electrode technique (SVET), volumetric H_2 evolution, gravimetric mass loss, and XPS techniques for this purpose. Such an experimental approach has been successfully applied in previous investigations to determine the extent to which inorganic inhibitor components (other than Li_2CO_3) dissolved in NaCl (aq) can stifle corrosion of AZ31B, as well as providing mechanistic insight to surface film formation.[41-43]

3.3 Experimental Procedures

Commercial AZ31B-H24 sheet metal product 1.5 mm thick was provided by Luxfer MEL Technologies (formerly Magnesium Elecktron) through Magna International. The chemical composition, as determined by inductively-coupled plasma optical emission spectroscopy (ICP-OES), is presented in Table 3.1. The composition reported is in compliance with that specified in ASTM B90/B90M-15 (“Standard Specification for Magnesium-Alloy Sheet and Plate”). The H24 temper implies the sheet product was strain hardened during rolling and then partially annealed to half hardness. No further processing was applied to the as-received sheet product. An isometric image of the AZ31B-H24 sheet product microstructure is shown in Figure 3.1. The material is a single phase alloy complete with a random distribution of secondary phase Al-Mn intermetallic particles. The composition of these particles are most commonly reported as Al_8Mn_5 with sizes ranging from 2 μm to 20 μm,[44] although Al-Mn particles with sizes on the order of tens of nanometers have also been resolved with TEM.[45] The average grain size in the rolling direction-transverse direction (RD-TD) plane is 6.5±0.4 μm, which was determined using the Heyn lineal intercept procedure described in ASTM E112-13 (“Standard Test Methods for Determining Average Grain Size”).

Table 3.1. Chemical Composition (wt%) of AZ31B-H24 Sheet Metal

Mg	**Al**	**Zn**	**Mn**	**Si**	**Fe**	**Cu**	**Ni**
Bal.	3.01	1.03	0.30	0.01	<0.005	<0.01	<0.005

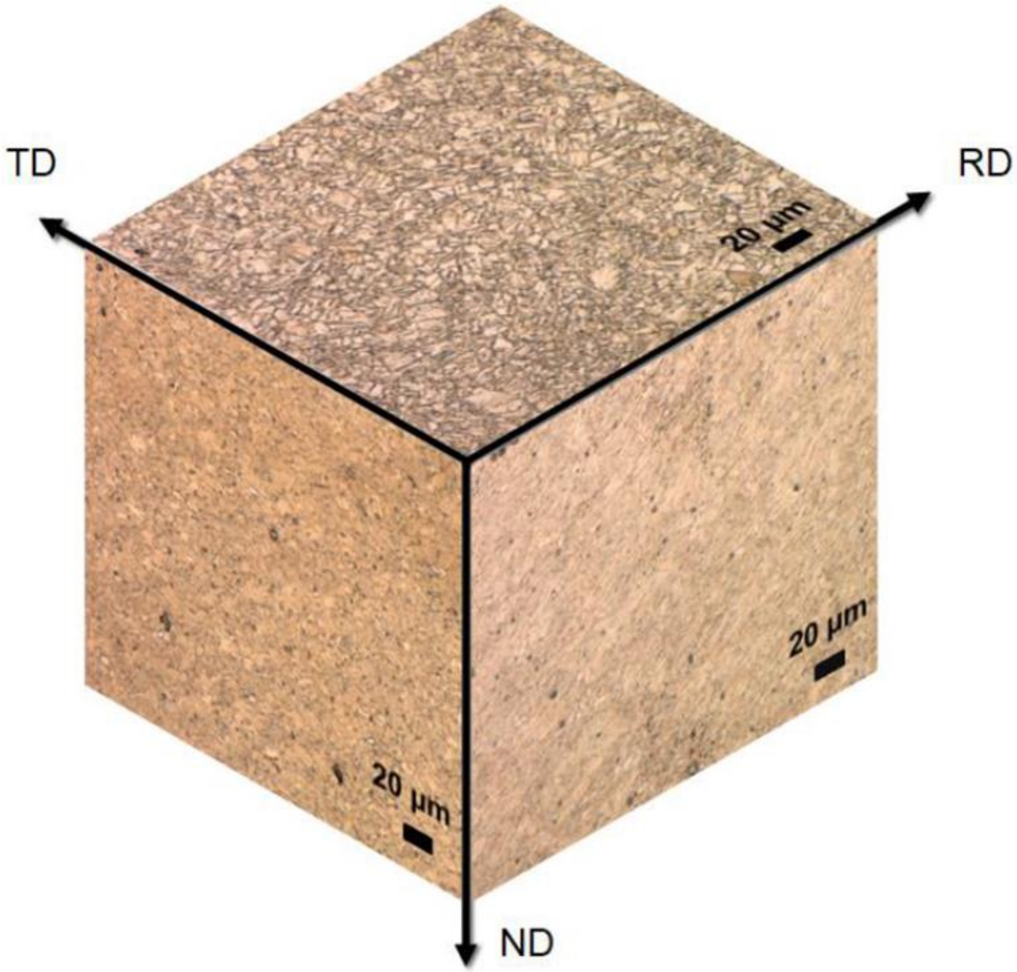

Figure 3.1. Three-dimensional microstructure of the AZ31B-H24 sheet metal reconstructed using light optical microscopy images. The black dots indicate Al-Mn particles.

The effectiveness of dissolved Li_2CO_3 to inhibit corrosion of AZ31B-H24 immersed in bulk 100 mM NaCl (aq) was evaluated using electrochemical polarization, volumetric H_2 evolution, and gravimetric mass loss with two concentrations: 1 mM (pH 10.3) and 100 mM (pH 11.1). The 100 mM solution is just below saturation, which has been measured to 12.75 g/L (172.5 mM) at 25°C.[46] An equivalent set of tests was evaluated with two concentrations of dissolved LiOH, added in sufficient quantity to produce the same pH achieved with the two dissolved Li_2CO_3 concentrations, to help differentiate a dissolved carbonate ion ($CO_3^{\ 2-}$) effect from the pH effect. Reagent grade NaCl (s), Li_2CO_3 (s), and LiOH (s) were used along with distilled water to make the corrosive solutions. A freshly prepared solution was used at ambient temperature for each experiment. No attempt was made to aerate or deaerate the solution either before or during immersion.

Open-circuit potential (OCP) and potentiodynamic polarization measurements were performed using a conventional three-electrode cell that used AZ31B-H24 as the working electrode, a saturated calomel electrode (SCE) as the reference electrode, and a graphite rod as a counter electrode. Potentiodynamic polarization measurements were initiated after a 1 h conditioning at the OCP. A scan rate of 1 mV/s was used starting at a potential −250 mV relative to the steady-state OCP measured after the 1 h conditioning step. Each measurement was repeated at least three times for reproducibility. A computer-controlled Gamry Reference 600™† potentiostat was used to record the OCP response and perform the polarization measurements. Working electrodes were prepared by attaching a coated Cu wire to the rear face of a square (10 mm× 10 mm) sample and then cold mounting in epoxy resin with the front face (RD-TD plane) boldly exposed. The working (front face) surface was mechanically abraded using silicon carbide (SiC) paper up to a 2400 grit surface finish, using an ethylene glycol:ethanol mixture as a lubricant, and then rinsed with ethanol and dried with an absorbent wipe.

Longer term (96 h) bulk immersion tests were also conducted to enable volumetric

H_2 evolution measurements as a function of immersion time and an overall secant mass loss measurement for the exposure. Somewhat larger (15 mm× 15 mm) square AZ31B-H24 samples were used in these tests with all exposed (face and edge) surfaces prepared by mechanical abrasion using the procedure described earlier. Volumetric H_2 evolution measurements were made using the inverted burette method.[47] The inverted burette was centered above the sample, which was placed flat on a rubber stopper at the bottom of a 2,000 mL beaker containing 1,500 mL of the corrosive solution. A glass funnel was attached to the end of the burette to aid, with a diameter much larger than the dimensions of the sample to help with the efficient collection of H_2 bubbles. Gravimetric mass loss measurements were made using a digital balance with 0.1 mg precision. Descaling of corrosion products was achieved using the procedure described in ASTM G1 ("Standard Practice for Preparing, Cleaning, and Evaluating Corrosion Test Specimens"), involving the immersion of the corroded sample in a solution comprised of 200 g CrO_3, 10 g $AgNO_3$, and 20 g $Ba(NO_3)_2$ dissolved in 1,000 mL water for 60 s at room temperature. Each immersion test was repeated three times for reproducibility.

SVET measurements were made using a Uniscan Instruments Model 370[†] scanning electrochemical workstation with an associated Environmental TriCell[†]. Working electrodes were prepared in the same manner as that described above for the polarization measurements with the only difference being the use of a smaller square (5 mm× 5 mm) sample. Voltages were measured between the scanning Pt tip and a graphite ground/reference electrode. The diameter of the Pt tip was specified by the manufacturer to be in the range of 5 μm to 50 μm. Scans were performed after various immersion times up to 24 h in: (i) 100 mM NaCl (aq) with pH ~7, (ii) 100 mM NaCl (aq) + 100 mM Li_2CO_3 with pH 11.1, and (iii) 100 mM NaCl (aq) + 3 mM LiOH with pH 11.1. The probe outputs were measured using a series of sweeping line scans across the scan area with a velocity 1,000 µm/s with a height and width step size 100 µm and return velocity 2,000 µm/s. The probe was vibrated in the vertical direction with an amplitude of 30 µm and a frequency of 80 Hz. The gain of the electrometer was set to 1,000, and the full-scale sensitivity of the lock-in amplifier was set to 16 mV. The peak-to-peak SVET voltage signal (Vpp) is related to the current flux density along the axis of probe vibration (i_z) by:

$$V_{pp} = i_z \left(A_{pp} / \kappa \right) \qquad (1)$$

where κ is solution conductivity. SVET was used to help provide a qualitative overview assessment in terms of (i) time to breakdown, (ii) formation of mobile anodes, and (iii) cathodic activation associated with the mobile anodes.

Post-exposure XPS surface analyses were conducted on intact surface films that formed during short-term immersion (2.5 h) in the same solutions used for the SVET measurements. Square (10 mm× 10 mm) samples that were mechanically abraded using the procedure described earlier were used for this purpose. The XPS analysis was conducted using a PHI Quantera II[†] scanning XPS microprobe instrument. Spectra were acquired using monochromatic Al Ka x-rays at 1,487 eV. A pass energy of 224 eV was used for the survey and 26 eV for high-resolution peaks of elements of interest. The step size was 0.8 eV for the survey and 0.1 eV for the high-resolution measurements. The take-off angle was 45°. Sputter depth profiles were acquired from a 1mm× 1mmsquare region using an Ar^+ ion beam operated with voltage of 1 kV.

3.4 Results

Figures 3.2(a) and (b) compare the OCP response of AZ31B-H24 measured after immersion in 100 mM NaCl (aq) containing dissolved Li_2CO_3 and LiOH, respectively. All OCP responses show similar features, which includes an initial increase to a local maximum value followed by a decay toward an eventual steady-state value. However, the time it takes to reach the local maximum in the OCP, the associated value, and the steady-state value vary with the dissolved Li_2CO_3 and LiOH concentration. The breakdown point of the native surface film formed on Mg and selected alloys immersed in NaCl (aq) can be identified by a local maximum in the OCP transient following immersion, marking the breakdown potential (E_b).[48] Thus, the value of E_b can be used as a measure of the relative chemical stability of the native surface film toward staving off corrosion. Values of the time required to reach E_b in 100 mM NaCl (aq) containing dissolved Li_2CO_3 and LiOH are listed in Table 3.2 for comparison. The trend is the same with both dissolved compounds; the time required for breakdown of the native surface film increases with an increase in the concentration added. Li_2CO_3 is less effective at extending the time for breakdown at pH 10.3, but is as effective as LiOH at extending the time for breakdown at pH 11.1. The value of E_b becomes more positive with the greater dissolved Li_2CO_3 and LiOH concentration Similarly, the steady-state OCP attained after breakdown becomes more positive with the additions in both cases. The increase is more pronounced with Li_2CO_3, as it coincides with the most positive (noble) steady-state OCP attained after breakdown.

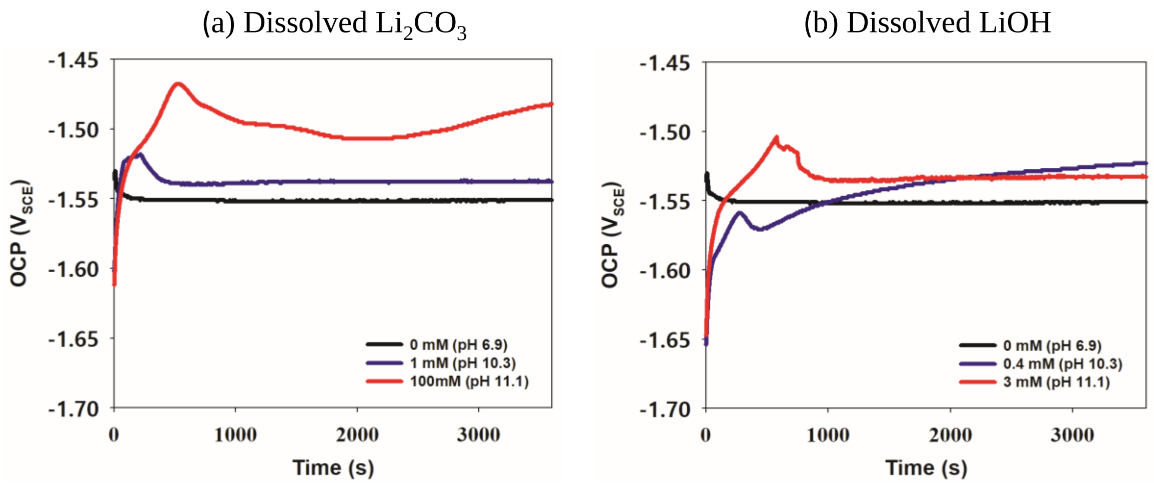
(a) Dissolved Li_2CO_3

(b) Dissolved LiOH

Figure 3.2. OCP response measured immediately after immersion on 0.1 M NaCl (aq) at ambient temperature: (a) with dissolved Li_2CO_3 and (b) with dissolved LiOH.

Table 3.2. Time Required for Surface Film Breakdown (Eb) in 100 mM NaCl (aq)

pH	**Li_2CO_3 (mM)**	**Time (s)**	**E_b (V_{SCE})**	**LiOH (mM)**	**Time (s)**	**E_b (V_{SCE})**
~7	0	15 ± 3	−1.53 ± 0.05	0	15 ± 3	−1.53 ± 0.05
10.3	1	220 ± 16	−1.52 ± 0.09	0.4	265 ± 4	−1.56 ± 0.11
11.1	100	585 ± 15	−1.47 ± 0.12	3	570 ± 10	−1.50 ± 0.05

Figures 3.3(a) and (b) show the typical potentiodynamic polarization response of AZ31B-H24 measured after 1 h condition at the OCP in 100 mM NaCl (aq) containing dissolved Li_2CO_3 and LiOH, respectively. Both dissolved compounds affect the polarization response in a similar manner. The increase in the dissolved Li_2CO_3 and LiOH concentration coincides with a significant reduction in global anodic and cathodic kinetics. The reduction in global cathodic kinetics by both dissolved compounds is progressively larger with increasing concentration coinciding with lower global kinetics. A similar progressive decrease in the global anodic kinetics is observed with dissolved

Li_2CO_3. The global anodic kinetics associated with dissolved LiOH exhibit an inflection point that occurs at different potentials, where this potential is found to be less positive potential with the higher concentration addition. However, the global anodic kinetics converge at higher overpotentials, the magnitude of which being significantly lower than exhibited without dissolved LiOH. Unlike the case for global anodic and cathodic kinetics, the effect of the dissolved compounds on the corrosion potential (E_{corr}) is distinctly different. Dissolved Li_2CO_3 causes a progressive decrease in E_{corr}, whereas dissolved LiOH has no effect on E_{corr}.

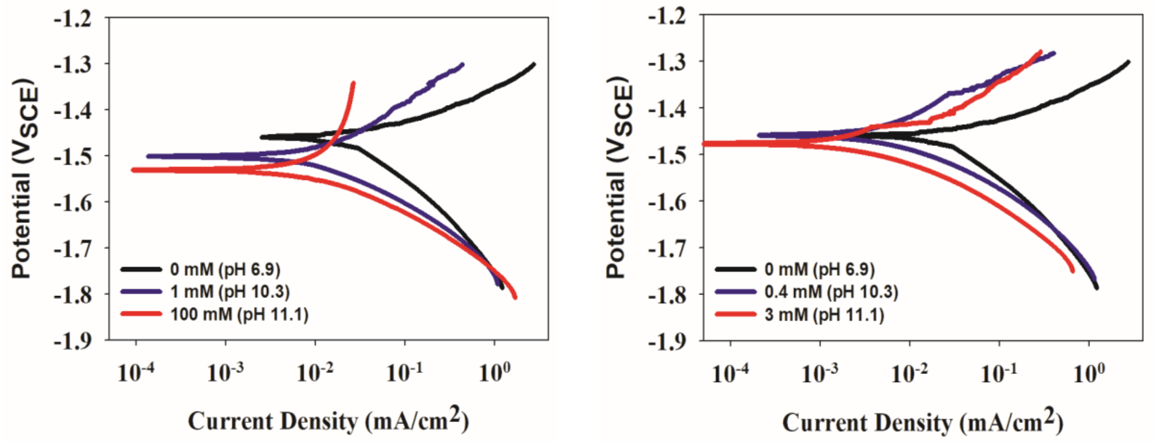
(a) Dissolved Li_2CO_3

(b) Dissolved LiOH

Figure 3.3. Potentiodynamic polarization response measured after conditioning at the OCP for 1 h in 0.1 M NaCl (aq) at ambient temperature: (a) with dissolved Li_2CO_3 and (b) with dissolved LiOH.

The amount of H_2 evolved during corrosion of AZ31B-H24 immersed in 100 mM NaCl (aq) with dissolved Li_2CO_3 and LiOH is shown in Figures 3.4(a) and (b), respectively. The H_2 evolution kinetics follows a linear rate law, with the corresponding rate (slope of the line) decreasing with an increase in the dissolved concentration of both compounds. The extent of inhibition observed at pH 11.1 is greater for the Li_2CO_3 addition. The observation of a linear rate law is consistent with reported literature for AZ31 immersed in NaCl (aq).[6] Figures 3.4(c) and (d) compare the corrosion rate determined from the 96 h mass loss measurement with that determined from the H_2 evolution measurements for dissolved Li_2CO_3 and LiOH, respectively. To calculate the corrosion rate from the H_2 evolution measurements, the total volume of H_2 evolved after the exposure was converted to moles of H_2 evolved. It was assumed that 1 mole of Mg was oxidized for every mole of H_2 gas evolved (100% efficiency) according to:

$$Mg\,(s) + 2H_2O\,(l) \rightarrow Mg\left(OH\right)_2(aq) + H_2\,(g) \qquad (2)$$

The moles of Mg oxidized were converted to a mass of Mg oxidized which, in turn, were adjusted by dividing by the nominal composition of Mg in the alloy to capture the mass of the alloy oxidized. The corresponding corrosion rate ($mg/cm^2/d$) was calculated by dividing the oxidized mass by the exposed surface area and the exposure time. The mass loss value is consistently higher than H_2 evolution value. This is an expected observation based on corrosion rate measurements reported for AZ31B in NaCl (aq).[47] The likely explanation for the discrepancy is that the rate of H_2 gas collection is not 100% efficient. Gas bubbles were observed to stick to the corroding AZ31B-H24 surface, as well as to the glass surfaces used to construct the collection apparatus (inverted funnel and upside-down burette). This is one of the main limitations of this technique.[49] A contribution from the oxygen reduction reaction is unlikely as the pH in the solutions under study are less 13, which seems to be required during corrosion of AZ31B when immersed in aqueous alkaline solutions.[50] Despite the discrepancy between the mass loss and the volumetric H_2

gas rate, the trend with both metrics is the same: corrosion rate decreases with increasing dissolved Li_2CO_3 and LiOH concentrations. It is clear that dissolved Li_2CO_3 inhibits corrosion to a greater extent at pH 11.1: 0.08±0.03 (mass loss) and 0.03±0.01 (H_2 evolution) mg/cm^2/d for dissolved Li_2CO_3 versus 0.32±0.06 (mass loss) and 0.17±0.07 (H_2 evolution) mg/cm^2/d for dissolved LiOH.

(a) Dissolved Li_2CO_3

(b) Dissolved LiOH

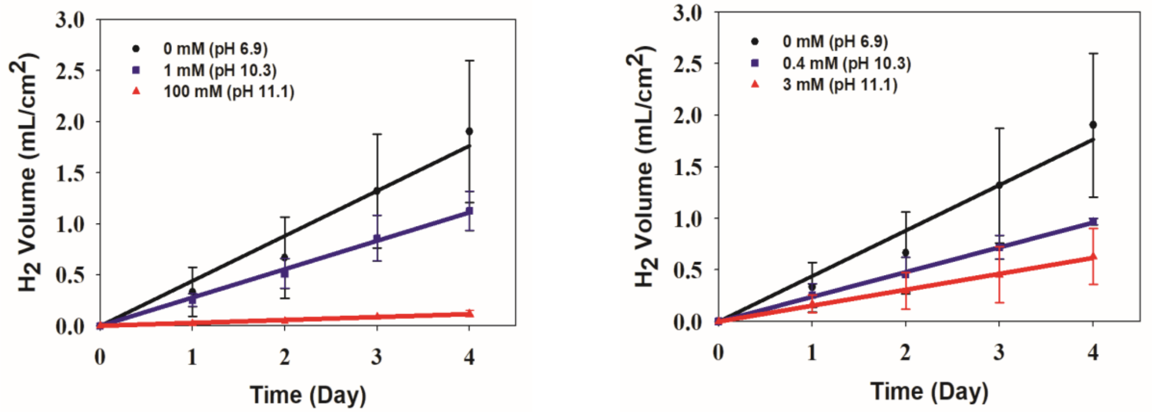

(c) Dissolved Li_2CO_3

(d) Dissolved LiOH

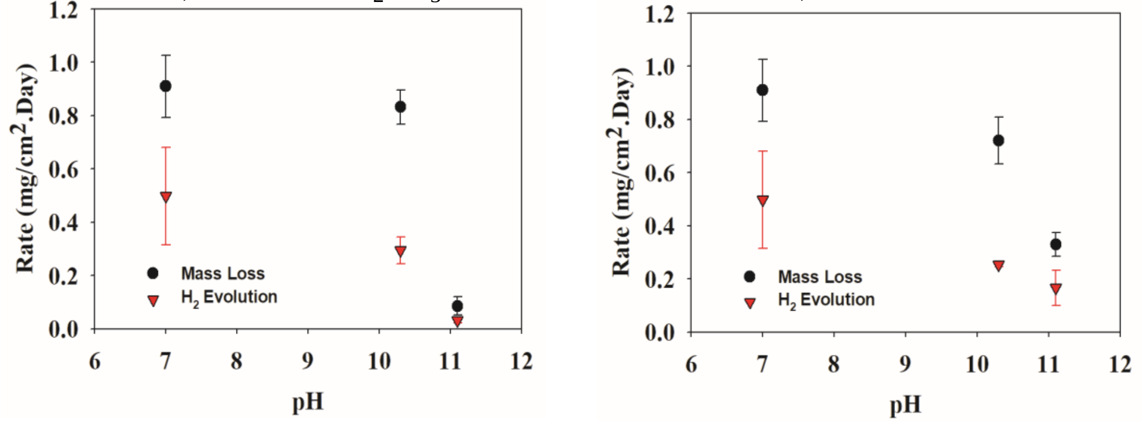

Figure 3.4. H_2 evolution measurements as a function of immersion time in 0.1 M NaCl (aq): (a) with dissolved Li_2CO_3 and (b) with dissolved LiOH. Corrosion rate comparison between mass loss and H_2 evolution after 96 h immersion: (c) with dissolved Li_2CO_3 and(d) with dissolved LiOH.

Figure 3.5 shows a set of photographic images of the AZ31B-H24 samples taken after 96 h immersion in 100 mM NaCl (aq) without and with dissolved Li_2CO_3 and LiOH. Figure 3.5(a) shows the surface after immersion in 100 mM NaCl (aq) without additions. Approximately 70% of sample area is covered with corrosion products associated with the filament-like corrosion mode. Dissolved Li_2CO_3 coincides with a significant reduction in the surface area covered with filament-like corrosion products (Figures 3.5[b] and [d]). In fact, filament corrosion product is not observed (with the unaided eye) on the surface immersed in the solution with 100 mM dissolved Li_2CO_3 (pH 11.1) (Figure 3.5[d]). Dissolved LiOH also coincides with a significant reduction in surface area covered by the filament-like corrosion product (Figures 3.5[c] and [e]). Filament-like corrosion product is visibly observed after immersion in the presence of 3 mM dissolved LiOH (pH 11.1) (Figure 3.5[e]).

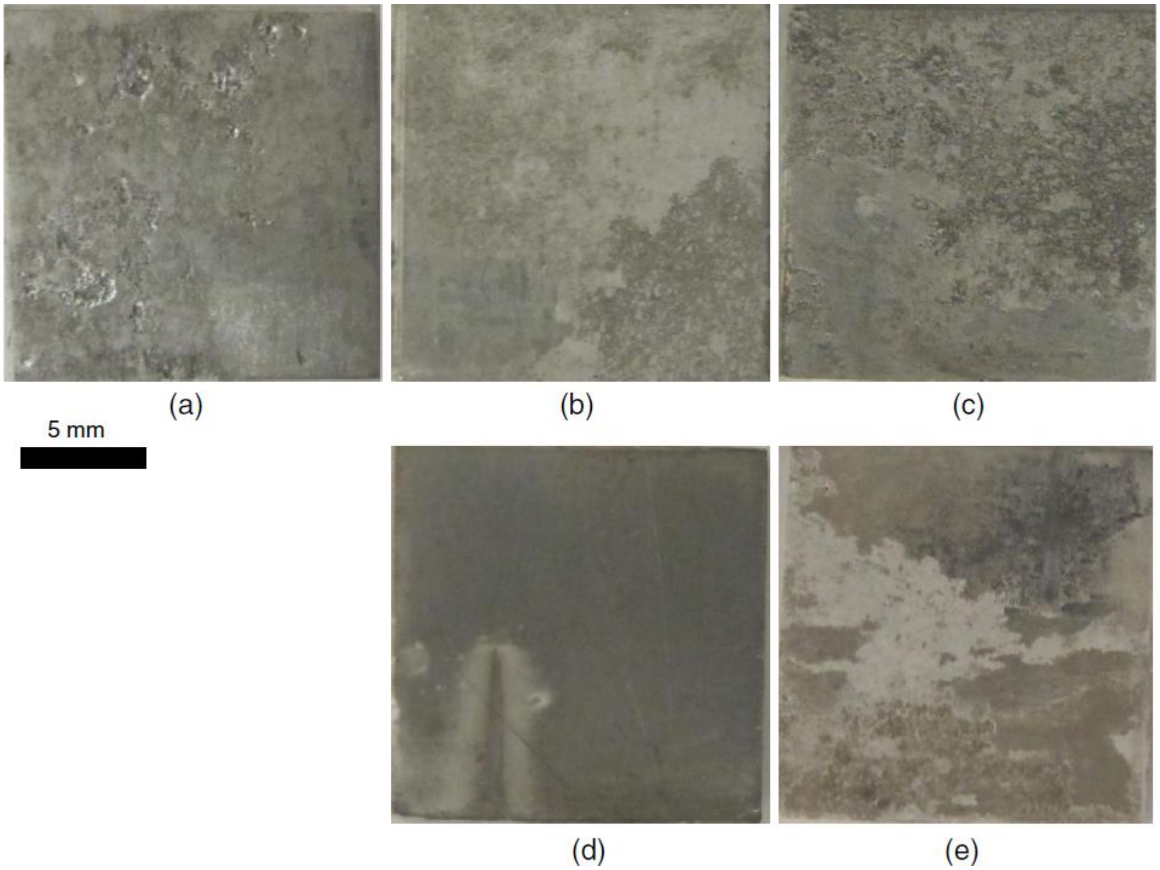

Figure 3.5. Photographic images of the typical surface appearance after 96 h immersion in 0.1 M NaCl (aq) at ambient temperature without (a) and with dissolved 10 mM (b) and 100 mM (d) Li_2CO_3 and dissolved 0.4 mM (c) and 3 mM (e) LiOH.

A set of SVET current density distribution maps acquired from AZ31B-H24 during immersion in 0.1 M NaCl (aq) over a 12 h period are shown in Figure 3.6 to give baseline measurements. The results plotted are considered typical from the replicate set measurements recorded. After 0.5 h of immersion, the presence of the focal anode located in the top left corner indicates that localized corrosion had already initiated before this time. This observation is consistent with the relatively short time required for breakdown of the native surface film indicated by the OCP response (15 s) shown in Figure 3.2. This focal anode is surrounded by a less intense and more diffuse cathode that occupies the remainder of the surface. The cathode current density is somewhat more intense along the top edge, directly to the right of the anode. With increased immersion time, this focal anode tends to separate into a cluster of anodes with similar current density that traverses laterally together across the surface: initially toward the bottom right corner (as measured after 2 h) and then across toward the right edge, where the cluster separates into two distinct focal anodes, again with similar current density (as measured after 4 h). These focal anodes are surrounded by a less intense and a more diffuse net cathode that is the remainder of the surface. After 6 h of immersion, only one focal anode can be observed, which has a significantly higher current density than the focal anodes that preceded it. Further immersion times show this focal anode also traverses laterally across the surface: initially toward the bottom left corner (as measured after 9 h) and then toward the top right corner (as measured after 12 h). This more intense focal anode is accompanied by a more intense cathode (increased current density) that is localized in the region trailing propagating focal anode, which demonstrates cathodic activation of the corroded surface. A photographic image of the corroded surface after 12 h immersion is also included. The majority of the surface is covered by a dark corrosion product. A small portion of the intact film remains at the top right corner of the surface.

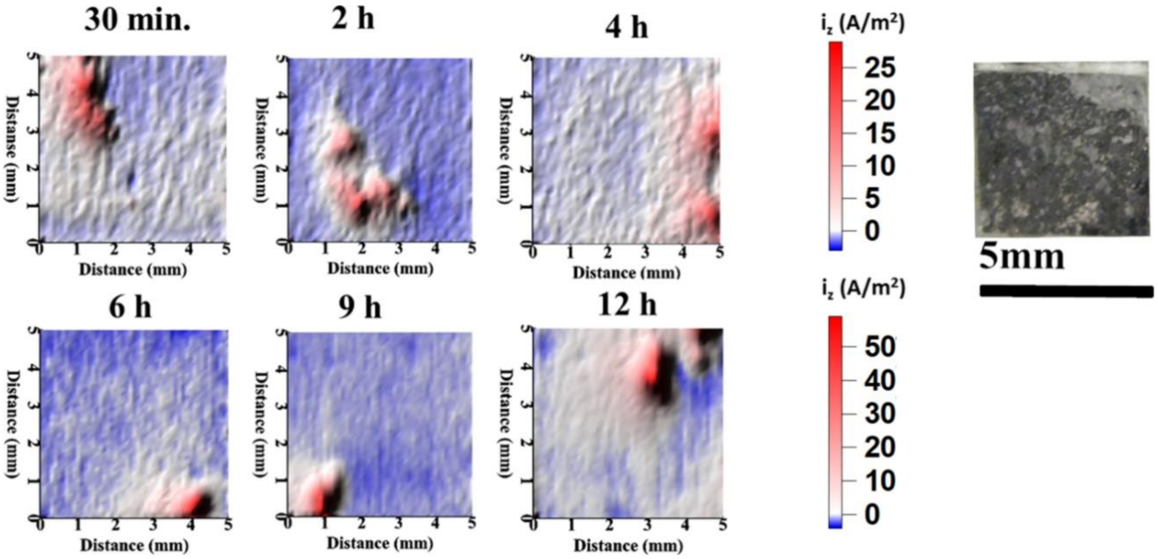

Figure 3.6. Time resolved SVET maps collected during immersion in 0.1 M NaCl (aq) at ambient temperature. Also included is a photographic image of the working surface after 12 h immersion.

Figure 3.7 shows a set of SVET current density distribution maps acquired from AZ31B-H24 during immersion in 0.1 M NaCl (aq) with 100 mM dissolved Li_2CO_3 (pH 11.1) for 24 h. After 0.5 h of immersion, a distinct anode and cathode is revealed in the surface, indicating that corrosion has initiated. The anode is located in the center with a lateral spread toward the bottom right corner and the cathode is located along the perimeter of the right half of the surface. The anode is significantly more diffuse and exhibits a significantly lower current density than that observed without dissolved Li_2CO_3 (Figure 3.6). With an increase in immersion time up to 4 h, the anode region shifts to the lower right corner, with a concomitant shift in the cathode to the upper left corner, with any significant change in the current density of either the anode or cathode. A further increase in immersion time to 8 h shifts the anode toward the bottom right corner, with a concomitant shift in the cathode to include the remainder of the surface. This anode shift coincides with a higher current density, which is consistent with a reduction in surface area occupied by the anode. A further increase in immersion time out to 20 h has little effect on the anode and cathode in terms of location and current density: the anode and cathode sites have become fixed in position. The exception is the development of a weaker anode shoulder that has formed along the bottom edge toward the right corner. The photographic image of the corroded surface after 24 h immersion shows the intact film remains very much intact over the surface save for the few localized dark spots that coincide with the fixed anode.

Figure 3.8 shows a set of SVET current density distribution maps acquired from AZ31B-H24 during immersion in 0.1 M NaCl (aq) with 3 mM dissolved LiOH (pH 11.1) for 24 h. After 0.5 h of immersion, a distinct anode and cathode region is revealed in the surface, indicating that corrosion has initiated in this case as well. The anode is located mostly in the lower right quadrant and the accompanying cathode located mostly in the upper half of the surface. Here too, the anode is significantly more diffuse and exhibits a significantly lower current density than that observed without the 3 mM LiOH addition (Figure 3.6). An increase in the immersion time to 8 h shifts the anode more toward the right half of the surface and the accompanying cathode is shifted more toward the left half of the surface. A further increase in immersion time to 20 h has little effect on the anode and cathode in terms of location and current density. However, after 24 h immersion, three focal anodes with increased current density are revealed in the bottom left corner.

These more intense focal anodes are accompanied by a more intense cathode (increased current density) that is localized in the region, presumably trailing the propagating focal anodes, which demonstrates cathodic activation of the corroded surface. The photographic image of the corroded surface after 24 h immersion shows the presence of dark corrosion product covering a portion. This portion for the surface is significantly smaller than that covering the surface immersed in 0.1 M NaCl (aq) without dissolved LiOH. This smaller portion reveals more clearly the filament-like nature of the corrosion mode. The observation of filament-like corrosion, complete with cathodic activation, in this alkaline solution is consistent with SVET measurements reported in the literature for AZ31 immersed in alkaline NaCl (aq), where pH was shown to significantly affect the filament-like corrosion at values ≥12.[6]

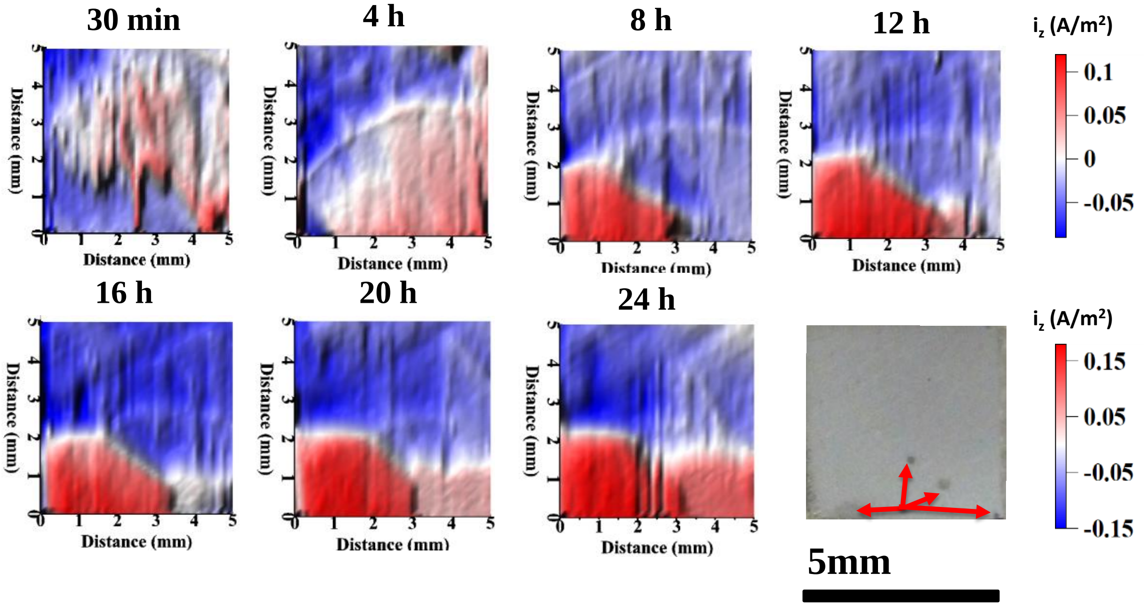

Figure 3.7. Time resolved SVET maps collected during immersion in 0.1 M NaCl (aq) with dissolved 100 mM Li_2CO_3 (pH 11.1) at ambient temperature. Also included is a

photographic image of the working surface after 24 h immersion.on. Localized corrosion indications (dark spots) are identified by the arrows.

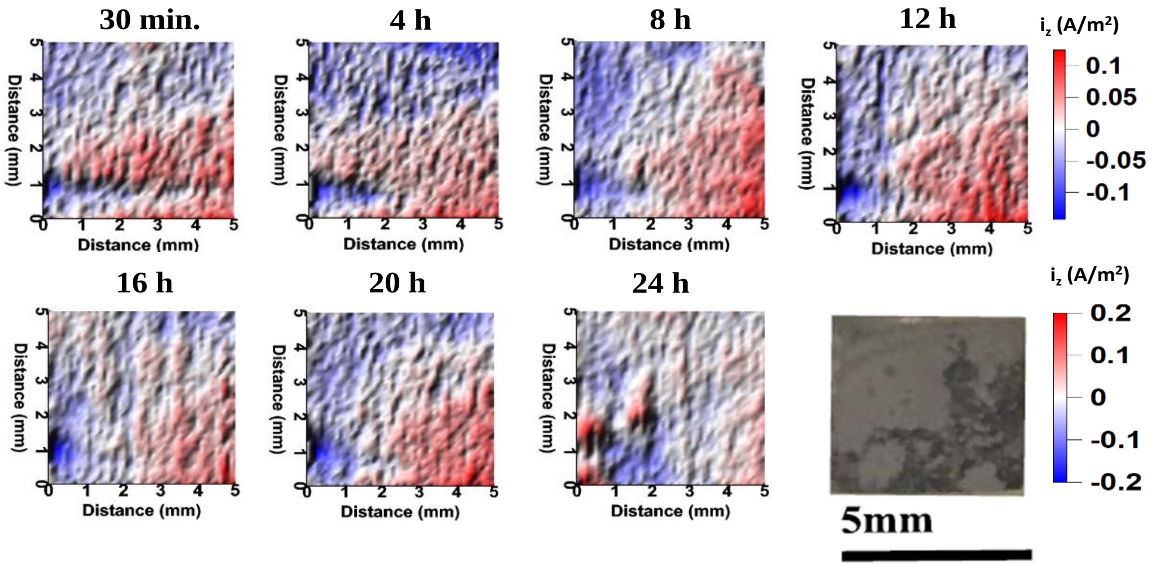

Figure 3.8. Time resolved SVET maps collected during immersion in 0.1 M NaCl (aq) with dissolved 3 mM LiOH (pH 11.1) at ambient temperature. Also included is a photographic image of the working surface after 24 h immersion.

A survey scan from each intact film (data not provided here), acquired after a very gentle sputter cleaning, reveals that the same set of elements are present on the surface: namely C, O, and Mg. Li was not detected in the intact film formed during immersion in 0.1 M NaCl (aq) with either dissolved compound. Figure 3.9 shows the high-resolution C1s, O1s, and Mg1s spectra acquired from the three intact surface films. Each C1s spectrum exhibits two peaks. The lower energy peak, which has a higher intensity, is consistent with adventitious C on the surface. It is this peak that was used to calibrate all spectra acquired by assigning it a binding energy of 284.8 eV.[51] The higher energy peak, which has a lower intensity, is consistent with metal carbonates (288 eV to 290 eV).[51] The intensity of this metal carbonate peak is higher on the intact film formed during immersion in 0.1 M NaCl (aq) with added Li_2CO_3. Given that Li was not detected on the surface, this metal carbonate is likely $MgCO_3$. The formation of $MgCO_3$ over Li_2CO_3 is consistent with the increased thermodynamic stability (lower solubility) of $MgCO_3$.[33] Each Mg1s spectrum exhibits a single peak. The breadth of the peak is consistent with there being overlapping peaks involving $MgO/Mg(OH)_2$ (1,304.5 eV)[51] and $MgCO_3$ (1,305 eV).[51] The O1s peak structure is more complex. The peak for the intact film formed in 0.1 M NaCl (aq) exhibits a distinct lower energy shoulder, clearly indicating overlapping peaks. The higher energy peak is consistent with a metal carbonate (531.5 eV to 532 eV),[51] whereas the lower energy shoulder is consistent with a metal oxide (529 eV to 530 eV).[51] The intact films formed with dissolved Li_2CO_3 and LiOH exhibit a single peak, which is shifted toward metal carbonates. However, the breadth of the peak implies a significant metal oxide contribution.

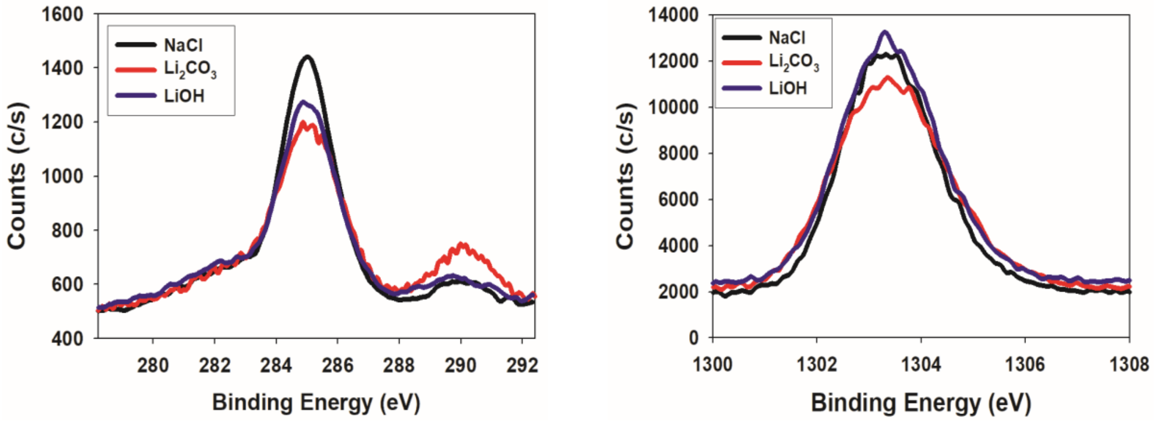
(a) C 1s

(b) Mg 1s

(c) O 1s

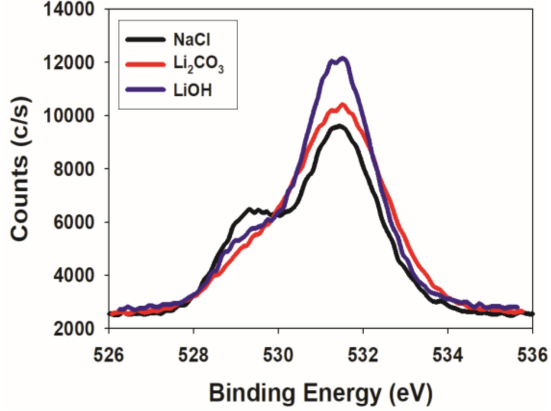

Figure 3.9. High resolution (a) C 1s, (b) Mg 1s and (c) O 1s XPS peaks acquired intact surface as formed after 2.5 h immersion in 0.1 M NaCl (aq) at ambient temperature without and with dissolved Li_2CO_3/LiOH (pH 11.1).

Figure 3.10 shows concentration depth profiles for C and O: the two Mg film-forming elements detected. The set profiles for C show that it is enriched at the film surface relative to the bulk in each case. The C enrichment is significantly higher on the intact film formed with dissolved Li_2CO_3. The thickness of the C enrichment (presumably $MgCO_3$) is relatively thin, as it takes 30 s of sputtering or less to remove in each case. The set of profiles for O show that content within the bulk of the intact film is reasonably similar. The content is about 45 at%, which suggests the film is comprised of MgO rather than $Mg(OH)_2$. Regardless, the more striking feature is the significantly difference in film thickness, with the films formed during immersion with the dissolved Li_2CO_3 and LiOH being much thinner than that formed without (during immersion in 0.1 M NaCl (aq) alone).

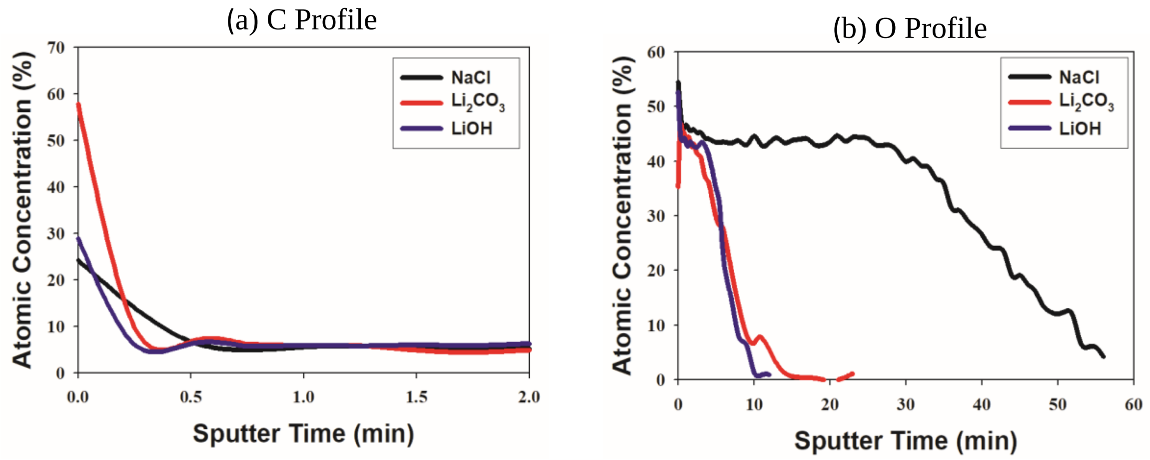

Figure 3.10. Elemental depth profile of the major filming elements (a) C and (b) O comprising the intact surface film as formed 2.5 h immersion in 0.1 M NaCl (aq) at ambient temperature without and with dissolved Li_2CO_3/LiOH (pH 11.1).

3.5 Discussion

The objective of this work was to determine the extent to which dissolved Li_2CO_3 inhibits corrosion of AZ31B-H24 when immersed in NaCl (aq) as a precursor feasibility study to applying Li_2CO_3 (s) as a pretreatment layer within a protective coating scheme. It is clear from Figure 3.4 that dissolved Li_2CO_3 significantly inhibits corrosion, particularly at a concentration (100 mM) approaching the solubility limit (172.5 mM).[46] Corrosion is reduced from 0.91±0.11 (mass loss) and 0.5±0.18 (H_2 evolution) mg/cm^2/d to 0.08±0.03 (mass loss) and 0.03 ±0.01 (H_2 evolution) mg/cm^2/d with 100 mM dissolved Li_2CO_3: an order of magnitude reduction. In comparison, dissolved LiOH at an equivalent pH (11.1) only reduces corrosion to 0.32±0.06 (mass loss) and 0.17±0.07 (H_2 evolution) mg/cm^2/d. The increased inhibition in the presence of dissolved Li_2CO_3 relative to dissolved LiOH, at an equivalent pH, indicates added benefits beyond alkalinity alone. Key aspects of the inhibitions are discussed below.

The chemistry of dissolved Li_2CO_3 can be summarized for the most part by the following set of chemical reactions (equilibrium constants quoted for 298 K):[52]

$$Li_2CO_3(s) \rightarrow 2Li^+(aq) + CO_3^{-2}(aq) \quad k_{sp} = 8.15 \times 10^{-4} \tag{3}$$

$$CO_3^{2-}(aq) + H_2O \rightarrow HCO_3^-(aq) + OH^-(aq) \quad k_b = 2\times 10^{-4} \tag{4}$$

Thus, possible factors affecting corrosion inhibition directly derived from the dissolved Li_2CO_3 include increased pH (alkalinity through OH^- production), Li^+ cation concentration, and/or the total dissolved carbonate concentration. The fact that dissolved Li_2CO_3 inhibits corrosion of AZ31B-H24 to a greater extent than dissolved LiOH at an equivalent pH implies that inhibition beyond alkalinity (pH) is provided by Li^+ cations and/ or dissolved carbonate anions. Figure 3.11 compares the potentiodynamic polarization curves for AZ31B-H24 after conditioning at the OCP for 1 h in 0.1 M NaCl (aq) without and with dissolved Li_2CO_3 and LiOH at pH 11.1. Both additions reduce the global cathode (H_2 evolution) and global anode (anodic dissolution) kinetics. The global cathodic kinetics is reduced by a similar extent, but the global anodic kinetics shows substantial differences. Both additions stifle the global anodic kinetics, but dissolved Li_2CO_3 has the greater effect, consistent with the lower global corrosion rate. It follows that alkalinity alone is likely responsible for the reduced global cathode (H_2 evolution) kinetics, whereas Li^+ cations and/or dissolved carbonate anions are responsible for the reduced global anodic kinetics beyond what alkalinity alone can achieve.

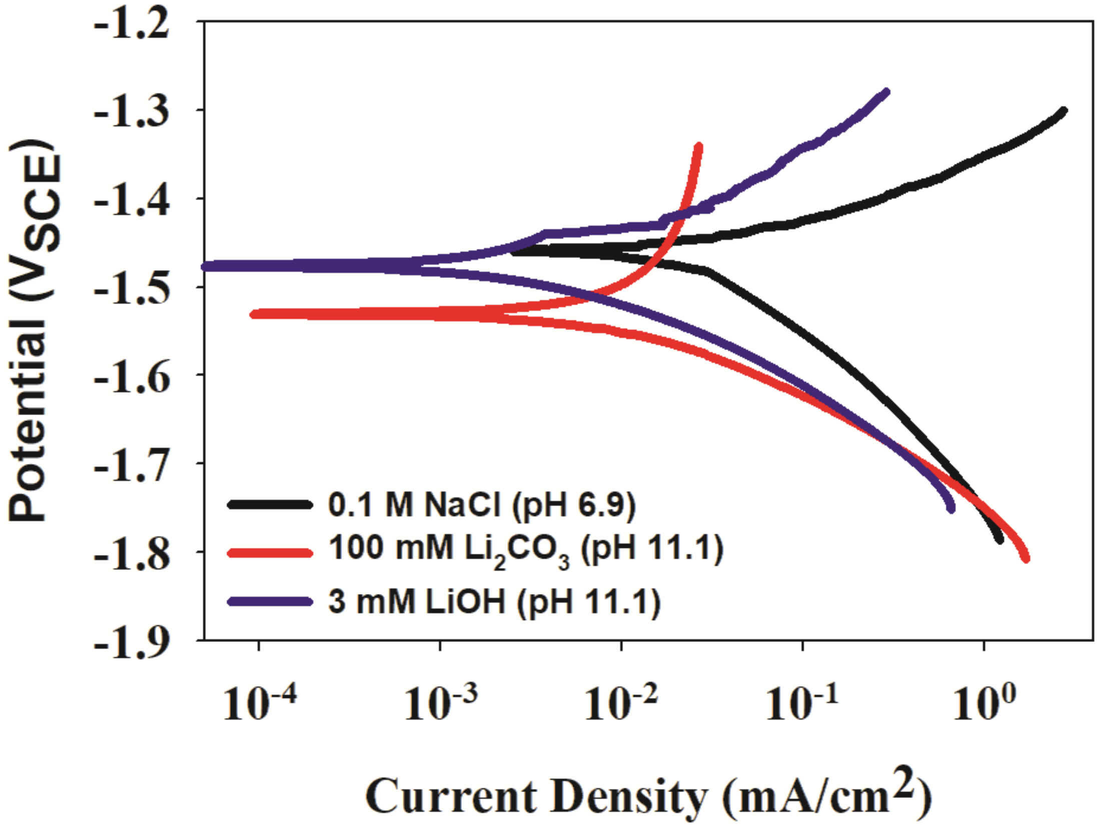

Figure 3.11. Potentiodynamic polarization response measured after conditioning at the OCP for 1 h in 0.1 M NaCl (aq) at ambient temperature without and with dissolved Li_2CO_3/LiOH (pH 11.1).

To help clarify the suspected Li^+ cation effect on the global anode kinetics, replicate potentiodynamic polarization measurements were conducted 0.1 M NaCl (aq) with the addition of 100 mM Na_2CO_3 and 3 mM Na(OH) (aq), respectively, and compared to the measurements made in the counterpart Li salt solutions. The comparison is shown in Figure 3.12. In the 100 mM carbonate solution, it is clear that the global anodic kinetics of AZ31B-H24 is lower with dissolved Li_2CO_3 relative to dissolved Na_2CO_3. In contrast, there is no significant difference in the global anodic kinetics of AZ31B in the hydroxide solution between dissolved LiOH and NaOH. Based on the latter, it is clear that the concentration of Li^+ matters to corrosion inhibition of AZ31B-H24.

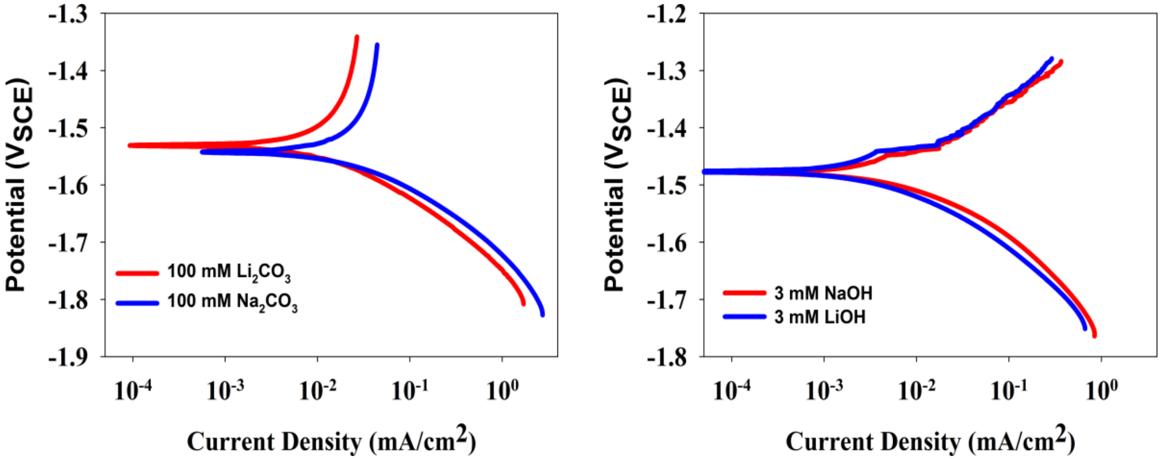
(a) Alkaline Carbonate

(b) Alkaline Hydroxide

Figure 3.12. Potentiodynamic polarization response measured after conditioning at the OCP for 1 h in 0.1 M NaCl (aq) at ambient temperature (a) with dissolved Li_2CO_3 vs. Na_2CO_3 (100 mM) and (b) with dissolved LiOH vs. NaOH (3 mM).

The initial set of time-resolved SVET measurements reveal similar features upon immersion in both alkaline solutions, consistent with corrosion involving a diffuse anode and cathode with limited mobility. Such corrosion is consistent with the OCP transients, which show that the time required for breakdown of the native surface film to occur is considerable short (less than 600 s) despite the longer times being recorded in the alkaline solutions (Table 3.2). This stage has been described as the “film forming” stage, whereby corrosion occurs according to Equation (1) with the formation of $Mg(OH)_2$ surface film through a dissolution-precipitation process.[6] The relatively low anodic current density measured is consistent with the relatively low Mg^{2+} cation concentration required to saturate the solution at pH 11.1 given the relatively low solubility product of $Mg(OH)_2$ (1.24×10^{-11} M at 25°C in 1 M NaCl (aq)).[53] A dissolution-precipitation process for $Mg(OH)_2$ formation on Mg corroding in alkaline NaCl (aq) (pH 9 to 11), the growth of which follows a linear rate law, has been recently verified using in situ Raman spectroscopy (RMS) and associated kinetic Raman mapping (KRM).[54] Sustained anodic dissolution in both cases results from the porous and evolving oxide-hydroxide film that forms in both neutral[55-57] and alkaline solutions[50,58] and the microgalvanic coupling to Al-Mn intermetallic particles that serve as fixed active cathodes.[6,10-12] The absence of filamentlike corrosion in the alkaline solutions after conditioning at the OCP for 1 h precludes any significant cathode activation contribution to the global cathode kinetics (Figure 3.11). The similarity in global cathode kinetics is consistent with this description. The simplest explanation for the lower cathodic kinetics observed in the alkaline solutions then is likely the reduction in the equilibrium half-cell potential of the H_2 evolution reaction at pH 11.1 (with dissolved Li_2CO_3/LiOH) relative to pH 6.9 (without dissolved Li_2CO_3/LiOH), as expected with mixed potential theory.

Significantly reduced anodic kinetics in the Li_2CO_3-alkaline solution, relative to the LiOH-alkaline solution, implies that Li^+ cations and/or dissolved carbonate anions play a key role in anodic dissolution. Alloyed Li is believed to significantly impede the anodic kinetics through the formation of a more stable oxidized surface layer, the precise chemistry of which is still being investigated.[29-32,34] Dissolved carbonate (HCO_3^-/CO_3^{2-}) anions, on the other hand, have a complex effect on anodic kinetics. Significantly more focus has been placed on elucidating the effect of bicarbonate (HCO_3^-) anions on the anodic dissolution of Mg and its alloys when considering dissolved CO_2 effects on corrosion[59-60] and corrosion in simulated bodily fluids.[61-62] Interestingly, deliberate HCO_3^- anion additions (less alkaline) tend to initially increase the anodic kinetics by enhancing dissolution of the air-formed $MgO/Mg(OH)_2$ film (exposing bare metal) and finally inhibiting anodic dissolution after an insoluble $MgCO_3$ corrosion product forms on the bare metal surface.[63] In contrast, deliberate CO_3^{2-} additions (more alkaline) tend to decrease anodic dissolution, presumably by the formation of a $MgCO_3$ corrosion product over-layer that serves as a physical barrier.[64] The XPS results, which show the formation of a thin $MgCO_3$ corrosion product over-layer on the intact $MgO/Mg(OH)_2$ surface film, formed in the Li_2CO_3-alkaline solution, provide some support for a CO_3^{2-} anion-induced inhibition of the anodic dissolution kinetics. However, as argued below, it is believed that Li^+ cations are responsible for the anodic dissolution inhibition observed.

A striking feature associated with the corrosion inhibition observed is the suppression of filament-like corrosion, at least on the macroscale. As discussed earlier, a "film formation" stage is quickly established upon immersion in the alkaline solutions. Initiation of the filament-like corrosion requires the localized breakdown of the intact surface film that forms during the “film formation” stage as a precursor event. The onset of the filament-like corrosion occurs rather quickly in 0.1 M NaCl (aq), as shown by the SVET measurement taken after 2 h of immersion. The onset is significantly delayed in the LiOH-alkaline solution, requiring at least 22 h of immersion to develop, whereas it does not develop within 24 h of immersion in the Li_2CO_3-alkaline solution. However, the localized dark spots are indicative that localized corrosion has initiated.[54]

The delayed breakdown in alkaline solution can be explained by the higher relative stability of the intact surface film in alkaline solutions. As the XPS analysis indicates, this film is comprised of MgO and $Mg(OH)_2$ as major components. Direct imaging and characterization by TEM and associated techniques of the intact film formed on Mg and its alloys during immersion in aqueous solutions consistently shows a layered structure with a thin, compact MgO layer residing at the film/metal interface.[7,54-58] This layer is prone to chemical dissolution (hydration) and associated stress-rupture when in contact with water,[7,65] with the hydration kinetics being much slower in alkaline solutions.[66-67] It is expected that bare metal is exposed at these hydration-induced stress-rupture sites that trigger localized corrosion initiation, which is the mode being dictated by solution chemistry. If we can take a cue from what is known about filament propagation, then it is reasonable to consider that cathodic activation of the dissolving bare metal site plays a key role in filament initiation. In the LiOH-alkaline solution, cathodic activation occurs and filament-like corrosion initiates, albeit with a lower anodic and cathodic current density relative to the 0.1 M NaCl (aq) case. In contrast, in the Li_2CO_3-alkaline solution, it is proposed that cathodic activation is effectively suppressed by the formation of a Li-containing oxide/hydroxide, with a similar mechanism to that proposed for Mg-Li-(Al-Y-Zr) alloys after the initial dissolution of the air formed Li_2CO_3 layer.[32] More research in the form of site-specific surface analysis of the breakdown site (dark regions in Figure 3.7) is necessary to confirm this hypothesis.

An alternative theory for the suppression of cathodic activation involves the formation of $MgCO_3$ on the dissolving bare metal surface, as suggested for Mg anodically dissolving in 0.1 M Na_2CO_3 (aq).[64] However, such formation is ruled unlikely considering the chemical stability for $Mg(OH)_2$ relative to $MgCO_3$ at pH 11.1, with the former being more stable at the CO_3^{2-} concentration of ∼100 mM used in this study.[33] Without cathodic activation, localized corrosion likely occurs with the continued anodic dissolution through the surface films formed with the necessary cathodic current being supplied by nearby Al-Mn intermetallic particles, which serve as active cathodes. There is clearly a need for more research to elucidate the underlying dissolved Li_2CO_3 inhibition mechanism. Planned studies include pretreating AZ31B-H24 with Li_2CO_3 coating applied via a chemical deposition process that will be coupled with site-specific surface analysis of focused ion beam sample preparation for characterization by TEM and associated techniques.

3.6 Conclusions

- Dissolved Li_2CO_3 significantly inhibits corrosion of AZ31B-H24 in 0.1 M NaCl (aq) at ambient temperature. The addition of 100 mM, which is below the solubility limit at 25°C, reduces corrosion by a factor of 10. Inhibition involves both the anode (anodic dissolution) and the cathode (H_2 evolution) processes. The increased inhibition in the presence of dissolved Li_2CO_3, relative to dissolved LiOH at an equivalent pH, indicates added benefits of dissolved Li beyond alkalinity alone.

- Corrosion inhibition is directly tied to the suppression of the filament-like corrosion mode and associated cathodic activation. Corrosion in the presence of dissolved Li_2CO_3 still involves initial "film formation," where corrosion involves the growth of an oxide/hydroxide surface film. However, the transition to filament-like corrosion, and associated cathodic activation, at a breakdown site is suppressed by the presence of dissolved Li_2CO_3. More research is required to delineate the fine scale electrochemical processes that are responsible for this suppression.

3.7 Acknowledgments

Funding was provided by Natural Science and Engineering Research Council (NSERC) and the Faculty of Engineering. Funding was also provided by the Egyptian Armament Authority (EAA) in the provision of a student stipend (B. Zaghloul).

3.8 References

1. W.J. Joost, JOM 64 (2012): p. 1032.

2. W.J. Joost, P.E. Krajewski, Scr. Mater. 128 (2017): p. 107.

3. R.C. McCune, J. Forsmark, B. Schneider, A. Luo, H. Gu, W. Schumacher, X. Chen, F. Vartolas, SAE Int. J. Mater. Manuf. 6 (2013): p. 242.

4. M.P. Brady, W.J. Joost, C.D. Warren, Corrosion 73 (2017): p. 452.

5. M. Liu, Y. Guo, J. Wang, M. Yergin, npj Mater. Degrad. 2 (2018): article 24.

6. G. Williams, H. ap Llwyd Dafydd, R. Grace, Electrochim. Acta 109 (2013): p. 489.

7. Z.P. Cano, M. Danaie, J.R. Kish, J.R. McDermid, G.A. Botton, G. Williams, Corrosion 71 (2015): p. 146.

8. Z.P. Cano, J.R. Kish, J.R. McDermid, J. Electrochem. Soc. 163 (2016): p. C732.

9. M.A. Melia, T.W. Cain, B.F. Briglia, J.R. Scully, J.M. Fitz-Gerald, JOM 69 (2017): p. 2322.

10. L.G. Bland, L.C. Scully, J.R. Scully, Corrosion 73 (2017): p. 526.

11. H.M. Krebs, A. Chirazi, L. Lechner, J. Gelb, X. Zhou, G.E. Thompson, P.J. Withers, “Time-Lapse Correlative 3D Imaging Applied to the Corrosion Study of AZ31 Mg Alloy in a Saline Environment,” in Frontiers in Materials Processing, Applications, Research and Technology, eds. M. Muruganant, C. Ali, B. Raj (Singapore: Springer, 2018), p. 165-177.

12. L.G. Bland, N Birbilis, J.R. Scully, J. Electrochem. Soc. 163 (2016): p. C895.

13. D. Rossouw, D. Fu, D.N. Leonard, M.P. Brady, G.A. Botton, J.R. Kish, Corrosion 73 (2017): p. 518.

14. S. Fajardo, C.F. Glover, G. Williams, G.S. Frankel, Corrosion 73 (2017): p. 482.

15. E. Michailidou, H.N. McMurray, G. Williams, J. Electrochem. Soc. 5 (2018): p. C195.

16. S. Thomas, N.V. Medhekar, G.S. Frankel, N. Birbilis, Curr. Opin. Solid State Mater. Sci. 19 (2015): p. 85.

17. G.S. Frankel, A. Samaniego, N. Birbilis, Corros. Sci. 70 (2013): p. 104.

18. M. Taheri, J.R. Kish, N. Birbilis, M. Danaie, E.A. McNally, J.R. McDermid, Electrochim. Acta 116 (2014): p. 396.

19. T. Cain, S.B. Madden, N. Birbilis, J.R. Scully, J. Electrochem. Soc. 162 (2015): p. C228.

20. N. Birbilis, T. Cain, J.S. Laird, X. Xia, J.R. Scully, A.E. Hughes, ECS Electrochem. Lett. 4 (2015): p. C34.

21. D. Hoche, C. Blawert, S.V. Lamaka, N. Scharnagl, C. Mendis, M.L. Zheludkevich, Phys. Chem. Chem. Phys. 18 (2016): p. 1279.

22. J. Li, W. Sun, B. Hurley, A.A. Luo, R.G. Buchheit, Corros. Sci. 112 (2016): p. 760.

23. S.H. Salleh, S. Thomas, J.A. Yuwono, K. Venkatesan, N. Birbilis, Electrochim. Acta 161 (2015): p. 144.

24. W.J. Binns, F Zargarzadah, V. Dehnavi, J. Chen, J.J. Noël, D.W. Shoesmith, Corrosion 75 (2019): p. 58.

25. J.E. Gray, B. Luan, J. Alloys Compd. 336 (2002): p. 88. 26. J. Wang, X. Pang, H. Jahed, AIMS Mater. Sci. 6 (2019): p. 567.

27. X.B. Chen, N. Birbilis, T.B. Abbott, Corrosion 67 (2011): p. 035005.

28. M.P. Brady, D.N. Leonard, H.M. Meyer III, J K. Thomson, K.A. Unocic, H.H. Elsentriecy, G-L. Song, K. Kitchen, B. Davis, Surf. Coat. Technol. 294 (2016): p. 164.

29. W. Xu, N. Birbilis, G. Sha, Y. Wang, J.E. Daniels, Y. Xiao, M. Ferry, Nat. Mater. 14

(2015): p. 1229.

30. Y.M. Yan, O. Gharbi, A. Maltseva, X.B. Chen, Z.R. Zeng, S.W. Xu, W.Q. Xu, P. Volovich, M. Ferry, N. Birbilis, Corrosion 75 (2019): p. 80.

31. Y. Yan, Y. Qiu, O. Gharbi, N. Birbilis, P.N.H. Nakashima, Appl. Surf. Sci. 494 (2019): p. 1066.

32. Y.M. Yan, A. Maltseva, P. Zhou, X.J. Li, Z.R. Zeng, O. Gharbi, K. Ogle, M. La Haye, M. Vaudescal, M. Esmaily, N. Birbilis, Corros. Sci. 164 (2020): p. 108342.

33. R.J. Santucci, M.E. McMahon, J.R. Scully, npj Mater. Degrad. 2 (2018): article 1.

34. Y. Yan, P. Zhou, O. Gharbi, Z. Zeng, X. Chen, P. Volovitch, K. Ogle, N. Birbilis, Electrochem. Commun. 99 (2019): p. 46.

35. R.G. Buchheit, M.D. Bode, G.E. Stoner, Corrosion 50 (1994): p. 205.

36. P. Visser, Y. Liu, X. Zhou, T. Hashimoto, G.E. Thompson, S.B. Lyon, L.G. van der Ven, A.J. Mol, H.A. Terryn, Faraday Discuss. 180 (2015): p. 511.

37. P. Visser, Y. Liu, H. Terryn, J.M.C. Mol, J. Coat. Technol. Res. 13 (2016): p. 557.

38. P. Visser, Y. Gonzalez-Garcia, J.M.C. Mol, H. Terryn, J. Electrochem. Soc. 165 (2018): p. 60.

39. P. Visser, M. Meeusen, Y. Gonzalez-Garcia, H. Terryn, J.M.C. Mol, J. Electrochem. Soc. 164 (2017): p. C396.

40. A. Kosari, P. Visser, F. Tichelaar, S. Eswara, J.N. Audinot, T. Wirtz, H. Zandbergen, H. Terryn, J.M.C. Mol, Appl. Surf. Sci. 512 (2020): p. 145665.

41. G. Williams, R. Grace, R.M. Woods, Corrosion 71 (2015): p. 184.

42. Z. Feng, B. Hurley, J. Li, R. Buchheit, J. Electrochem. Soc. 165 (2018): p. 94.

43. Z. Feng, B. Hurley, R. Buchheit, M. Zhu, Z. Yang, J. Hwang, J. Electrochem. Soc. 166 (2019): p. 520.

44. L. Shang, I.H. Jung, S. Yue, R. Verma, E. Essadiqi, J. Alloys Compd. 492 (2010): p. 173.

45. L. Xiao, L. Liu, Y. Zhou, S. Esmaeili, Metall. Mater. Trans. A 41 (2010): p. 1511.

46. W. Cheng, Z. Li, F. Cheng, J. Chem. Thermodyn. 67 (2013): p. 74.

47. A.D. King, N. Birbilis, J.R. Scully, Electrochim. Acta 121 (2014): p. 394.

48. G. Williams, H. ap Llwyd Dafydd, R. Subramanian, H.N. McMurray, Corrosion 73 (2017): p. 471.

49. N.T. Kirkland, N. Birbilis, M.P. Staiger, Acta Biomater. 8 (2012): p. 925.

50. S. Li, A.C. Bacco, N. Birbilis, H. Cong, Corros. Sci. 112 (2016): p. 596.

51. “XPS Reference Table of Elements,” Thermo Fischer Scientific Inc., https://xpssimplified.com/periodictable.php.

52. CRC Handbook for Chemistry and Physics, 93rd ed., ed. W.M. Haynes (Boca Raton, FL: CRC Press, 2013).

53. I. Lambert, H.L. Clever, Alkaline Earth Hydroxides in Water and Aqueous Solutions, IUPAC Solubility Data Series, vol. 52 (Oxford, United Kingdom: Pergamon Press, 1992), p. 104.

54. A. Maltseva, V. Shkirskiy, G. Lefèvre, P. Volovitch, Corros. Sci. 153 (2019): p. 272.

55. M. Taheri, R.C. Phillips, J.R. Kish, G.A. Botton, Corros. Sci. 59 (2012): p. 222.

56. K.A. Unocic, H.H. Elsentriecy, M.P. Brady, H.M. Meyer, G-L. Song, M. Fayek, R.A. Meisner, B. Davis, J. Electrochem. Soc. 161 (2014): p. C302.

57. M.P. Brady, G. Rother, L.M. Anovitz, K.C. Littrell, K.A. Unocic, H.H. Elsentriecy, G.-L. Song, J.K. Thomson, N.C. Gallego, B. Davis, J. Electrochem. Soc. 162 (2015): p. C140-C149.

58. M. Taheri, J.R. Kish, J. Electrochem. Soc. 160 (2013): p. C36.

59. L. Wang, T. Shinohara, B-P. Zhang, J. Alloys Compd. 496 (2010): p. 500.

60. Q. Qu, J. Ma, L. Wang, L. Li, W. Bai, Z. Ding, Corros. Sci. 53 (2011): p. 1186.

61. Y. Jang, B. Collins, J. Sankar, Y. Yun, Acta Biomater. 9 (2013): p. 8761.

62. R.-C. Zeng, Y. Hu, S.-K. Guan, H.-Z. Cui, E.-H. Han, Corros. Sci. 86 (2014): p. 171.

63. P. Gore, V.S. Raja, N. Birbilis, J. Electrochem. Soc. 165 (2018): p. C849.

64. B.R. Fazal, S. Moon, J. Korean Inst. Surf. Eng. 50 (2017): p. 147.

65. H.B. Yao, Y. Li, A.T.S. Wee, Appl. Surf. Sci. 158 (2000): p. 112.

66. D.A. Vermilyea, J. Electrochem. Soc. 116 (1969): p. 1179.

67. O. Fruhwirth, G.W. Herzog, I. Hollerer, A. Rachetti, Surf. Technol. 24 (1985): p. 301.

3.9 Supporting information

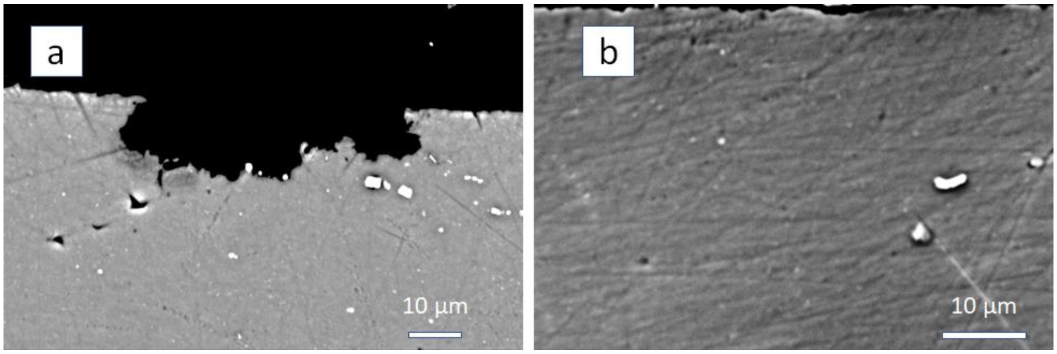

Figure 3.13. Cross-sectional SEM images For AZ31B-H24 of hydrogen evolution and mass loss measurements for 4 days in 0.1 M NaCl (aq) (a) 0 mM and (b) 100 mM (pH 11.1) Li_2CO_3 (aq).

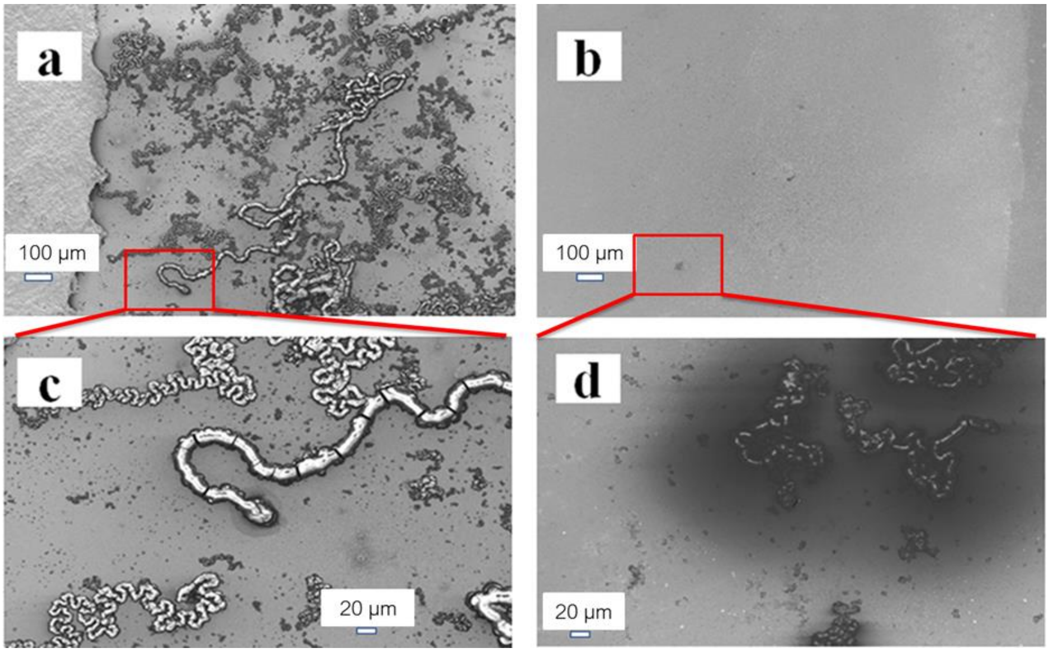

Figure 3.14. (a) Low magnification SEM image for AZ31B in 0.1 M NaCl (aq) after 2.5 h immersion time, (b) Low magnification SEM for AZ31B in 0.1 M NaCl (aq) with 100 mM Li_2CO_3 (aq) after 2.5 h immersion time, (c) Higher magnification of marked area in (a) and (d) Higher magnification of marked area in (b).

Chapter 4

Corrosion Inhibition of Mg Alloy ZEK100 Sheet Metal by Dissolved Lithium Carbonate

B. Zaghloul, J.R. Kish*

Centre for Automotive Materials and Corrosion

McMaster University, Hamilton, ON L8S 4L7

*Corresponding Author: (905) 525-9140, extension 21492, kishjr@mcmaster.ca

Submitted to Journal of The Electrochemical Society on 23rd June 2021.

4.1 Abstract

The extent of corrosion inhibition of Mg alloy ZEK100 in 100 mM NaCl (aq) imparted by dissolved Li_2CO_3 (aq), with a particular focus on Li incorporation into the surface film that forms under activated anodic dissolution (anodic polarization) was determined. Dissolved Li_2CO_3 reduces corrosion by a factor of ~12 when added at a concentration (100 mM) just below saturation. Effective inhibition involves suppressing the transition to filament-like corrosion, and associated anode/cathode activation, initiating at local breakdown sites. Such suppression is linked to the formation of Li-doped MgO as a corrosion product film during activated anodic dissolution. When formed by anodic polarization, the film composition also significantly affects the chloride ion distribution with the film. Without Li incorporation, chloride ions tend to enrich at the film/metal interface, whereas with Li incorporation, chloride ions tend to be uniformly distributed within the film.

4.2 Introduction

The low temperature formability of lightweight Mg alloy ZEK100 (1.3% Zn, 0.2% Nd, 0.25% Zr, balance Mg) sheet metal continues to attract interest in the automotive industry as a means to reduce vehicle weight (with concomitant improved fuel efficiency) through use of multi-material structural assemblies [1-3]. Increase utilization, however, continues to be stifled by corrosion, particularly so in NaCl (aq) [4-6]. Similar to Mg alloy AZ31B (3% Al, 1% Zn, 0.5% Mn, balance Mg) [7-11], corrosion of ZEK100 occurs via a localized filament-like mode that is driven by enhanced H_2 gas evolution (cathode activation) of the dissolving surface (anode activation) [12-14]. The mode involves the initiation of local activated anodes on the filmed surface, likely at secondary phase particles that serve as cathodes [15,16]. The local activated anodes then propagate across the filmed surface driven by cathode activation, which mostly takes place at the local anode site, but with some contribution from the porous oxide/hydroxide corrosion products left behind [17-19]. A consensus on the cathode activation mechanism has yet to be attained [20]. Proposed theories currently include the formation of an activated cathode either on the bare dissolving surface [21,22], noble metal enrichment due to selective dissolution of Mg [23-25] or re-deposition [26,27], or freshly formed $Mg(OH)_2$ [28]. An alternative, recently revisited, theory is the formation and subsequent dissolution of MgH_2 [29].

Application of a protective coating is the desired corrosion control strategy for Mg alloys in the automotive industry [5,30-32]. As a minimum for corrosion control, typical schemes include a surface pre-treatment barrier layer and a polymer-based sealant over-layer. The storage of inhibiting (inorganic or organic) compounds for controlled release at coating defects sites, however initiated, is a key design criterion for the development of next generation coating schemes. The concept is exemplified by the improved corrosion control of Mg alloys coated with inhibitor intercalated ion-exchangeable hydrotalcite (HT) or layered double hydroxide (LDH) surface pre-treated layers [33-39]. It follows that a well-developed understanding of a given inhibitor's efficiency in controlling corrosion of bare Mg alloys in NaCl (aq) is critical to inhibitor selection and, thus coating design. Inhibitor types studied in this context include anode/cathode site specific adsorption and barrier/blocking effects of anionic surfactants [40-43], complexing of dissolved noble metal (relative to Mg) to prevent re-deposition and associated cathode activation [44,45] and sparingly soluble anions to promote surface film formation [46-49].

Combining the beneficial effect of Li, as an alloying element, on stifling the anodic kinetics of Mg [50] and of dissolved OH− anions [51,52] and total dissolved carbonate anions (CO_3^{2-}/HCO_3^{-}), produce by dissolving a carbonate salt [53,54], on stifling both the anode and cathode kinetics of Mg, we investigated the inhibition extent imparted by dissolved Li_2CO_3 (aq) on the corrosion of AZ31B-H24 in 0.1 M NaCl (aq) with promising results [55]. We showed that dissolved Li_2CO_3 (aq) inhibits corrosion by suppressing the filament-like corrosion mode and associated anode/cathode activation at breakdown sites. We also showed that inhibition involves a reduction in both the global anode (anodic dissolution) and the global cathode (H_2 evolution) kinetics. We proposed the formation of a Li-containing oxide/hydroxide, with a similar mechanism to that proposed for Mg-Li-(Al-Y-Zr) alloys when corroding in NaCl (aq) [56-58], forms at breakdown sites to provide the inhibition observed, but presented no surface analysis evidence.

The purpose of this work was to determine the extent of corrosion inhibition of Mg alloy ZEK100 in 0.1 M NaCl (aq) imparted by dissolved Li_2CO_3 (aq), in terms of the combinatory inhibiting effect of Li^+ (aq), OH^- (aq) and CO_3^{2-}/HCO_3^- (aq). A particular focus was placed on determining the extent of Li incorporation into the surface film that forms under activated anodic dissolution (anodic polarization) in the presence of dissolved Li_2CO_3. Conventional electrochemical and bulk immersion measurements coupled with site specific X-ray photoelectron spectroscopy (XPS) and conventional and scanning transmission electron microscopy (TEM/STEM) were used for this purpose.

4.3 Experimental

Commercial ZEK100 sheet metal with a nominal thickness of 1.5 mm was supplied by Magna International (originally from Luxfer MEL Technologies (formerly Magnesium Elecktron)) in the fully-annealed O temper. Inductively coupled plasma - optical emission spectroscopy (ICP-OES) was used to determine the chemical composition: 1.4% Zn + 0.2% Nd + 0.28% Zr, balance Mg. A typical three-dimensional orthogonal view of the etched microstructure is shown in Figure 4.1a. The microstructure is comprised of a single phase (α Mg matrix phase) and a distribution of near-globular second phase intermetallic particles. These include ternary Mg-Zn-Nd and Zr-rich particles [12,59,60]. The typical appearance and elemental composition of the second phase particles is shown in Figure 4.1b by the backscattered electron image and associated EDS line scans. The average grain size (measured for the RD-TD plane using the Heyn lineal intercept procedure of ASTM E112-13) is 37 ± 0.6 μm.

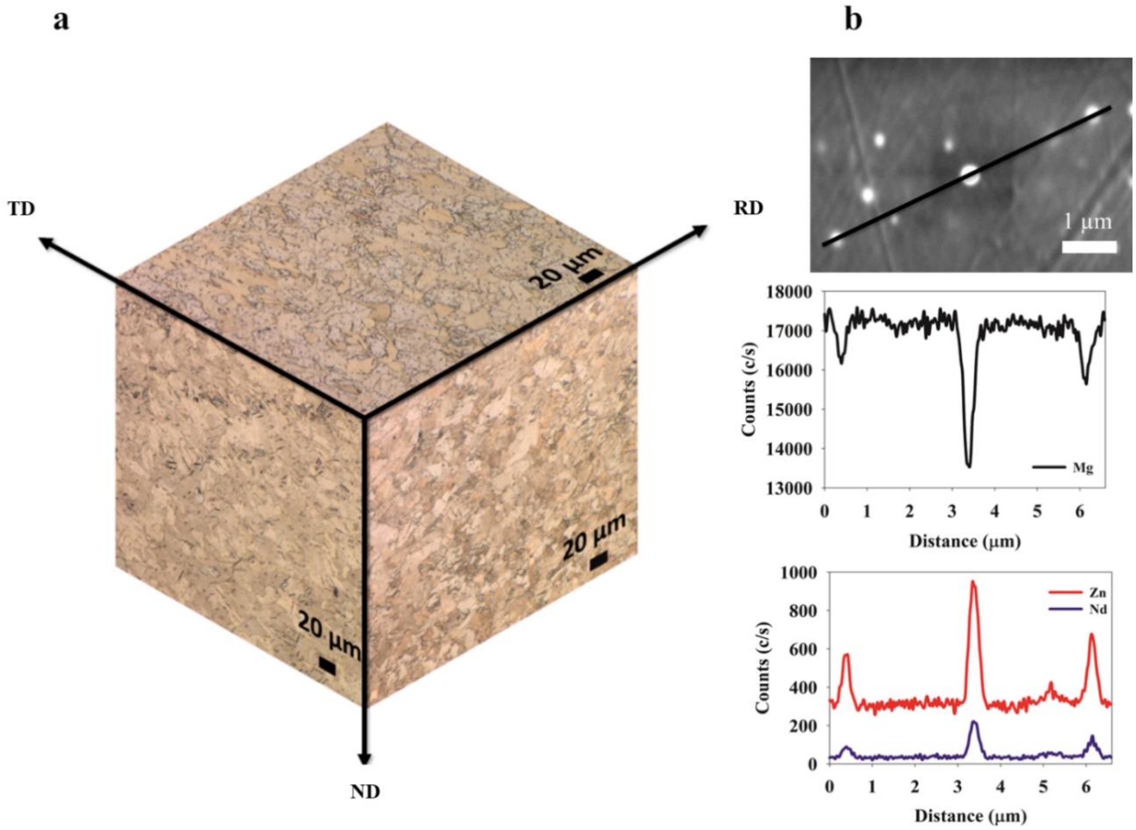

Figure 4.1. (a) Three-dimensional microstructure of the ZEK100 sheet metal reconstructed using light optical microscopy images. (b) back-scattered image of cross-sectional microstate showing typical appearance of second phase particles and associated SEM-EDS line scan showing elemental composition profile across such particles.

The inhibition effect of 0.1 M Li_2CO_3 (aq) on corrosion of ZEK100 immersed in 0.1 M NaCl (aq) at ambient temperature was assessed using electrochemical polarization, volumetric H_2 evolution and gravimetric mass loss. The Li_2CO_3 (aq) concentration chosen for study (0.1 M) is just below saturation: 12.75 g/L (0.1725 M) at 25 °C [61]. We showed that this concentration, over the range from 0.0001 M to 0.1 M, inhibited corrosion of AZ31B-H24 to the greatest extent [55]. The pH of this inhibiting solution is 11.1. Similar testing was conducted in pairs of test solutions to determine combinatory effects of dissolved Li^+ cations, OH^-anions and CO_3^{2-}/HCO_3^- anions on corrosion inhibition. Table 1 summarizes the solutions. Of the six solutions, two are near-neutral (pH ~7) and the remaining four are alkaline with pH ~11. In particular, solution 6 versus solution 1 provides the combinatory inhibiting effect of Li^+ (aq), OH^- (aq) and CO_3^{2-}/HCO_3^- (aq). Solution 2 versus solution 1 isolates the inhibiting effect of Li^+ (aq) at near-neutral pH (~7). Solutions 3 and 4 versus solution 1 isolate the inhibiting effect of OH^- (aq) with a high and low Li^+ (aq) concentration at alkaline pH (~11). Finally, solutions 5 and 6 versus solution 1 isolate the inhibiting effect of CO_3^{2-}/HCO_3^- (aq) with and without a high Li^+ (aq) concentration. All solutions were prepared fresh, using reagent grade chemicals and distilled water, and naturally aerated during testing.

Table 4.1. Summary of Test Solutions

No.	**Test Solution**	**Li^+ (aq)**	**OH^- (aq)**	**CO_3^{2-} / HCO_3^- (aq)**
1	100 mM NaCl (Baseline)	No	No	No
2	100 mM LiCl	Yes (high)	No	No
3	100 mM NaCl + 3 mM LiOH	Yes (low)	Yes	No
4	100 mM LiCl + 3 mM LiOH	Yes (high)	Yes	No
5	100 mM NaCl + 100 mM Na_2CO_3	No	Yes	Yes
6	100 mM NaCl + 100 mM Li_2CO_3	Yes (high)	Yes	Yes

Electrochemical measurements, including open-circuit potential (OCP) and potentio-dynamic polarization, were conducted using a conventional three electrode polarization cell. A saturated calomel electrode (SCE) was used a reference electrode and a graphite rod was used as a counter electrode. The sequence used consisted of an 1 h immersion at the OCP followed by a potentiodynamic polarization using scan rate of 1 mV/s, starting at a potential −250 mV relative to the steady-state OCP recorded after 1 h. Each polarization measurement was repeated at least three times for reproducibility. A computer-controlled Gamry Reference 600™ potentiostat was used for these measurements. The RD-TD plane of ZEK100 served as the working surface. A coated Cu wire was attached to the back face of a square (10 mm × 10 mm) sample before cold mounting in epoxy resin with the front face exposed to create a working electrode. The working surface was mechanically abraded to a 2400 grit surface finish, using SiC abrasive paper (CAMI 800/FEPA P2400, micron 14) and an ethylene glycol-ethanol lubricant, and then rinsed with ethanol and dried with an absorbent wipe. These measurements were not IR corrected.

Bulk immersion tests (96 h in duration) were used to determine the corrosion kinetics via volumetric H_2 evolution measurements made as a function of immersion time. Larger square (15 mm × 15 mm) samples were used for bulk immersion testing. The face and edge surfaces were prepared using the mechanical-abrasion procedure already described. Volumetric H_2 evolution measurements were made using the inverted burette method [62]. The working sample was placed flat on a rubber stopper on the bottom of a beaker containing 1500 mL of the test solution, centered underneath an inverted burette. A glass funnel, with a diameter much larger than the working sample, was attached to the open end of the inverted burette to help improve efficiency of H_2 bubble collection. A mass loss measurement was also made after the 96 h duration, using a digital balance with 0.1 mg precision. A secant rate was determined using this value for comparative purposes. The measurement was made after removal of corrosion products, which involved immersing the corroded sample in a solution comprised of 200 g CrO_3, 10 g $AgNO_3$ and 20 g $Ba(NO_3)_2$ dissolved in 1000 mL water for 60 s at room temperature (as described in ASTM G1). Each immersion test was repeated three times for reproducibility.

XPS was used to determine the composition of the intact surface film that formed on square samples (10 mm × 10 mm) during short-term immersion (2.5 h) in 0.1 M NaCl (aq) with and without dissolved Li_2CO_3. The working surface (RD-TD plane) was prepared using the mechanical-abrasion procedure already described. A PHI Quantera II Scanning XPS Microprobe instrument was used for this purpose. Spectra were acquired using monochromatic Al Ka X-rays at 1487 eV and a 45° take-off angle. The survey was acquired using a pass energy of 224 eV and a step size of 0.8 eV. High resolution peaks of elements of interest were acquired using a pass energy of 26 eV and a step size of 0.8 eV.

TEM/STEM was used to determine the composition of the film formed under potentiostatic anodic polarization using the electrochemical apparatus already described. Two 0.1 M NaCl (aq) based solutions were used: one with dissolved Li_2CO_3 and the other with dissolved Na_2CO_3. The potential was held for 30 minutes. at a value 150 mV more positive than the OCP, which was established after 1 h conditioning. Working samples were carefully removed from the epoxy mount after anodic polarization. FIB milling (Zeiss NVision† 40 FIB microscope) was then used to create electron transparent thin cross-sectional foils of the anodic film suitable for the TEM/STEM examination (Thermo

Scientific Talos 200X equipped with a Gatan ContinuumS GIF EELS spectrometer and a Super-X EDS system). Since the anodic films produced were relatively thin, an initial protective layer of C was electron beam deposited on the region of interest followed by an over-layer of ion beam deposited W. The foils were examined using an operating voltage of 200 kV with a cryogenic stage used to maintain the sample temperatures near −178 °C to minimize electron beam damage. This procedure has proved successful in resolving fine scale features of anodic films formed on Mg [23] and Mg alloys [8,63].

4.4 Results

Figure 4.2 shows four OCP transient comparisons for ZEK100 immersed in the different solutions listed in Table 4.1. Collectively, the OCP transients show similar features, namely an initial rapid increase to a local maximum value and subsequent relatively slower decay to a local minimum value followed by a small increase to a quasi steady state value. Such features are commonly observed in OCP transients of Mg and Mg alloy in aqueous saline solutions. The local maximum attained has been correlated with the breakdown of the intact surface film and, thus demarcates a breakdown potential (E_b) [14,64]. Thus, relative differences in the chemical stability of the intact surface film against breakdown and associated localized corrosion can be assessed based on the time to reach E_b. Such a comparison in presented in Table 4.2. In general, the time to reach E_b is longer time in the alkaline solutions.

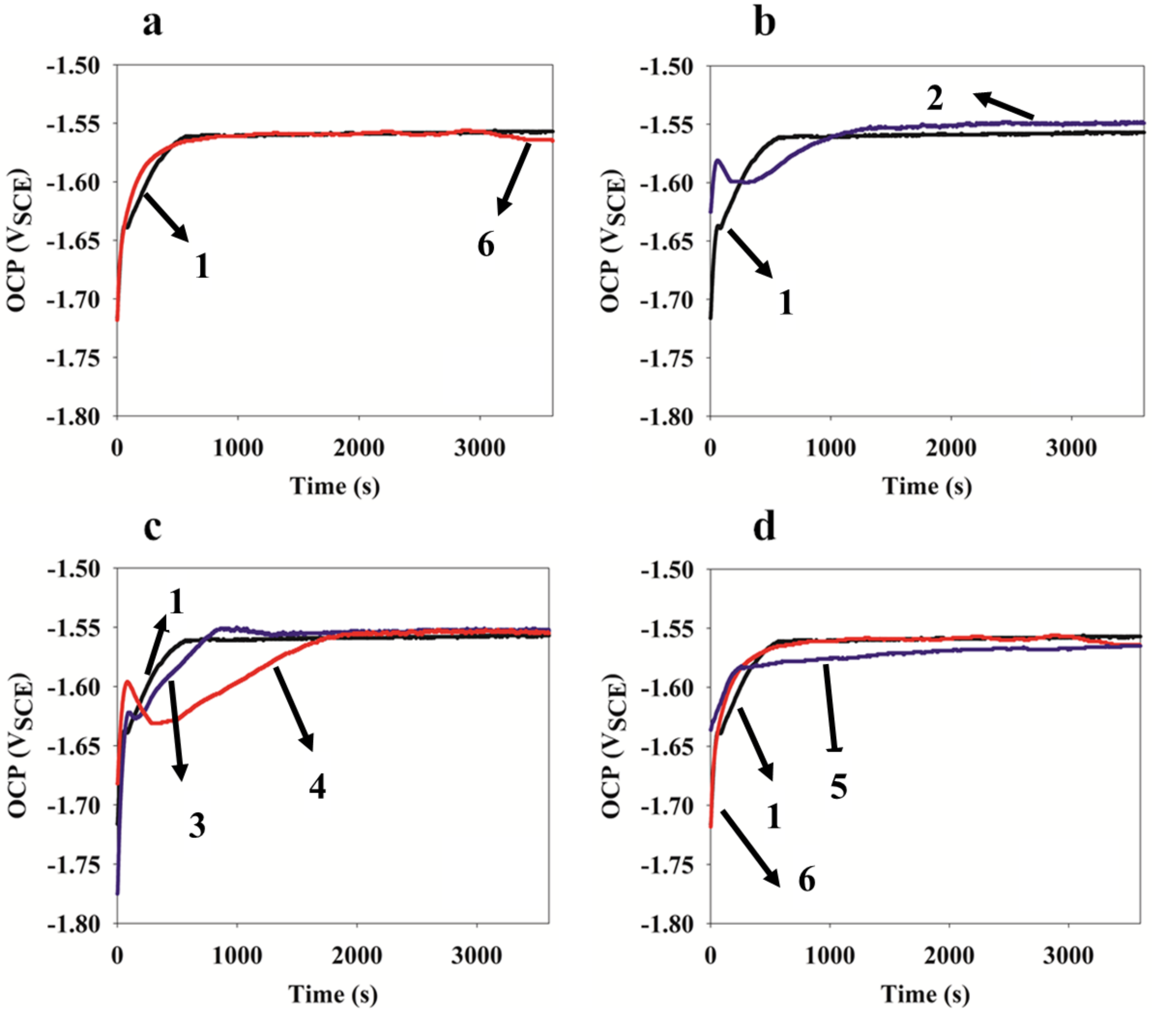

Figure 4.2. OCP transients for ZEK100 immersed in the different solutions listed in Table 4.1: solution 1: 100 mM NaCl (aq) (baseline); solution 2: 100 mM LiCl (aq); solution 3: 100 mM NaCl (aq) + 3 mM LiOH (aq); solution 4: 100 mM LiCl (aq) + 3 mM LiOH (aq); solution 5: 100 mM NaCl (aq) + 100 mM Na_2CO_3 (aq); solution 6: 100 mM NaCl (aq) + 100 mM Li_2CO_3 (aq).

Table 4.2. Time Required for Surface Film Breakdown (E_b)

No.	**pH**	**Solution Composition**	**Time (s)**	**E_b (V_{SCE})**
1	Near-Neutral (~7)	100 mM NaCl	64 ± 14	−1.64 ± 0.12
2	Near-Neutral (~7)	100 mM LiCl	62 ± 31	−1.58 ± 0.09
3	Alkaline (~11)	100 mM NaCl + 3 mM LiOH	99±7	−1.62 ± 0.08
4	Alkaline (~11)	100 mM LiCl + 3 mM LiOH	88 ± 23	−1.59 ± 0.02
5	Alkaline (~11)	100 m M NaCl + 100 mM Na_2CO_3	261 ± 59	−1.58 ± 0.13
6	Alkaline (~11)	100 mM NaCl + 100 mM Li_2CO_3	2971 ± 37	−1.56 ± 0.06

Several observations regarding the combinatory effect of the inhibitors on the relative stability of the intact surface film (time to reach E_b) formed on ZEK100 are extracted. First, replacing100 mM NaCl (aq) with 100 mM LiCl (aq) has no significant effect on increasing the relative chemical stability of the intact surface film (Figure 4.2b). The time to reach E_b is essentially the same considering the experimental errors reported the replicate measurement sets: 62 ± 31 s for LiCl (aq) versus 64 ± 14 s for NaCl (aq). Second, the addition of 3mM LiOH (aq) has a beneficial effect on the chemical stability of the intact surface film, relative to the baseline (Figure 4.2c). The time to reach E_b is increased: 99 ± 7 s with LiOH (aq) versus 64 ± 14 s without. However, no additional benefit is observed when replacing 100 mM NaCl (aq) with 100 mM LiCl (aq). The time to reach E_b is essentially the same considering the experimental errors reported the replicate measurement sets: 88 ± 23 s for LiCl (aq) with LiOH versus 99 ± 7 s NaCl (aq) with LiOH (aq). Third, the addition of 100 mM Na_2CO_3 (aq) also has a beneficial effect on the chemical stability of the intact surface film, relative to the baseline (Figure 4.2d). The time to reach E_b is increased, relative to the baseline: 261 ± 59 s with Na_2CO_3 (aq) versus 64 ± 14 s without. However, a substantial additional benefit is observed when replacing 100 mM Na_2CO_3 with 100 mM Li_2CO_3 (aq). The time to reach E_b is sustainably increased: 2971 ± 37 s with Li_2CO_3 (aq) versus 261 ± 59 s with Na_2CO_3 (aq). Thus, the largest increase in the time to breakdown, relative to the baseline (solution 1), is observed with the addition of 100 mM Li_2CO_3 (solution 6).

Figure 4.3 shows four potentiodynamic polarization measurement comparisons for ZEK100 immersed in the different solutions listed in Table 4.1. Figure 4.3a shows the effect of adding 100 mM Li_2CO_3 (aq) on the polarization response of ZEK100, relative to the baseline solution. The addition coincides with a significant reduction in both the global anode and cathode kinetics. The global anode kinetics exhibit an increased polarizability with dissolved Li_2CO_3 present, which is indicative of the formation of a more protective surface film. Regarding the combinatory effect of the inhibitors, the following observations are extracted from the remaining comparisons. First, replacing 100 mM NaCl (aq) with 100 mM LiCl (aq) has no significant effect on either the global anode or cathode kinetics (Figure 4.3b). Second, the addition of 3mM LiOH (aq) reduces both the global anode and cathode kinetics, relative to the baseline (Figure 4.3c). However, the addition has little effect on the polarizability of the global anode kinetics. An additional reduction in global cathode kinetics is observed when replacing 100 mM NaCl (aq) with 100 mM LiCl (aq) in combination with 3 mM LiOH (aq). However, there is no effect on global anode kinetics other than being shifted to more negative potentials. Third, the addition of 100 mM Na_2CO_3 (aq) also reduces both the global anode and cathode kinetics, relative to the baseline (Figure 4.3d). The addition also increases the polarizability of the global anode kinetics. An additional reduction in both the global anode and cathode kinetics is observed when replacing 100 mM Na_2CO_3 (aq) with 100 mM Li_2CO_3 (aq), without altering the increased polarizability of the anode kinetics.

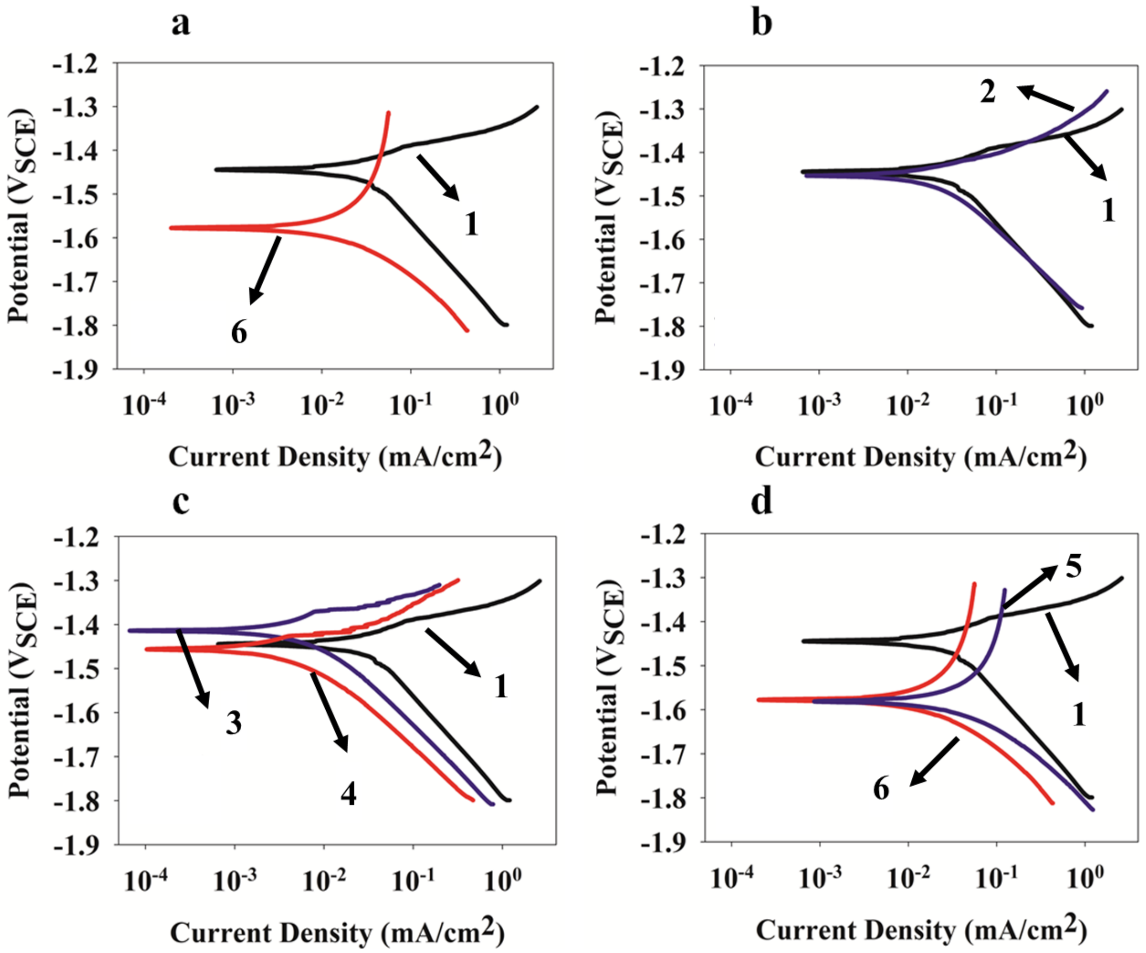

Figure 4.3. Potentiodynamic anodic polarization measurements for ZEK100 immersed in the different solutions listed in Table 4.1: solution 1: 100 mM NaCl (aq) (baseline); solution 2: 100 mM LiCl (aq); solution 3: 100 mM NaCl (aq) + 3 mM LiOH (aq); solution 4: 100 mM LiCl (aq) + 3 mM LiOH (aq); solution 5: 100 mM NaCl (aq) + 100 mM Na_2CO_3 (aq); solution 6: 100 mM NaCl (aq) + 100 mM Li_2CO_3 (aq).

Plots comparing the volumetric H_2 evolution measurements made during corrosion of ZEK100 immersed in the different solutions listed in Table 4.1 are shown in

Figure 4.4. H_2 evolution during the corrosion follows a linear rate law in all solutions, regardless of composition and pH. The R^2 value for each case is included in the legend for comparative purposes. The linear rate constants are listed in Table 4.3. The addition of 100 mM dissolved Li_2CO_3 significantly reduces the rate of H_2 evolution by an order of magnitude (by a factor of 11.5), relative to the baseline (Figure 4.4a). The following observations are extracted for combinatory effect of the inhibitors. First, replacing 100 mM NaCl (aq) with 100 mM LiCl (aq) reduces the H_2 evolution rate to a small extent (Figure 4.4b): from 0.369 to 0.221 mL/cm^2/day. Second, the addition of 3 mM LiOH (aq) reduces H_2 evolution rate to a larger extent (Figure 4.4c): from 0.369 to 0.067 mL/cm^2/day. Replacing 100 mM NaCl (aq) with 100 mM LiCl (aq), in combination with 3 mM LiOH (aq), reduces the rate further: from 0.067 to 0.44 mL/cm^2/day. Third, the addition of 100 mM Na_2CO_3 (aq) also reduces the H_2 evolution rate to a large extent (Figure 4.4d): from 0.369 to 0.035 mL/cm^2/day. An additional reduction in rate is observed when replacing 100 mM Na_2CO_3 (aq) with 100 mM Li_2CO_3 (aq): from 0.035 to 0.032 mL/cm^2/day.

The linear rate constants extracted from the volumetric H_2 evolution measurements were converted to corresponding corrosion rate. This was achieved by first converting the volume of H_2 evolved to moles of H_2 evolved using the ideal gas law. Then it was assumed that 1 mole of H_2 gas was evolved for each mole of Mg that was oxidized (100% efficiency) according to:

$$Mg\,(s) + 2H_2O\,(l) \rightarrow Mg\left(OH\right)_2(aq) + H_2\,(g) \qquad (1)$$

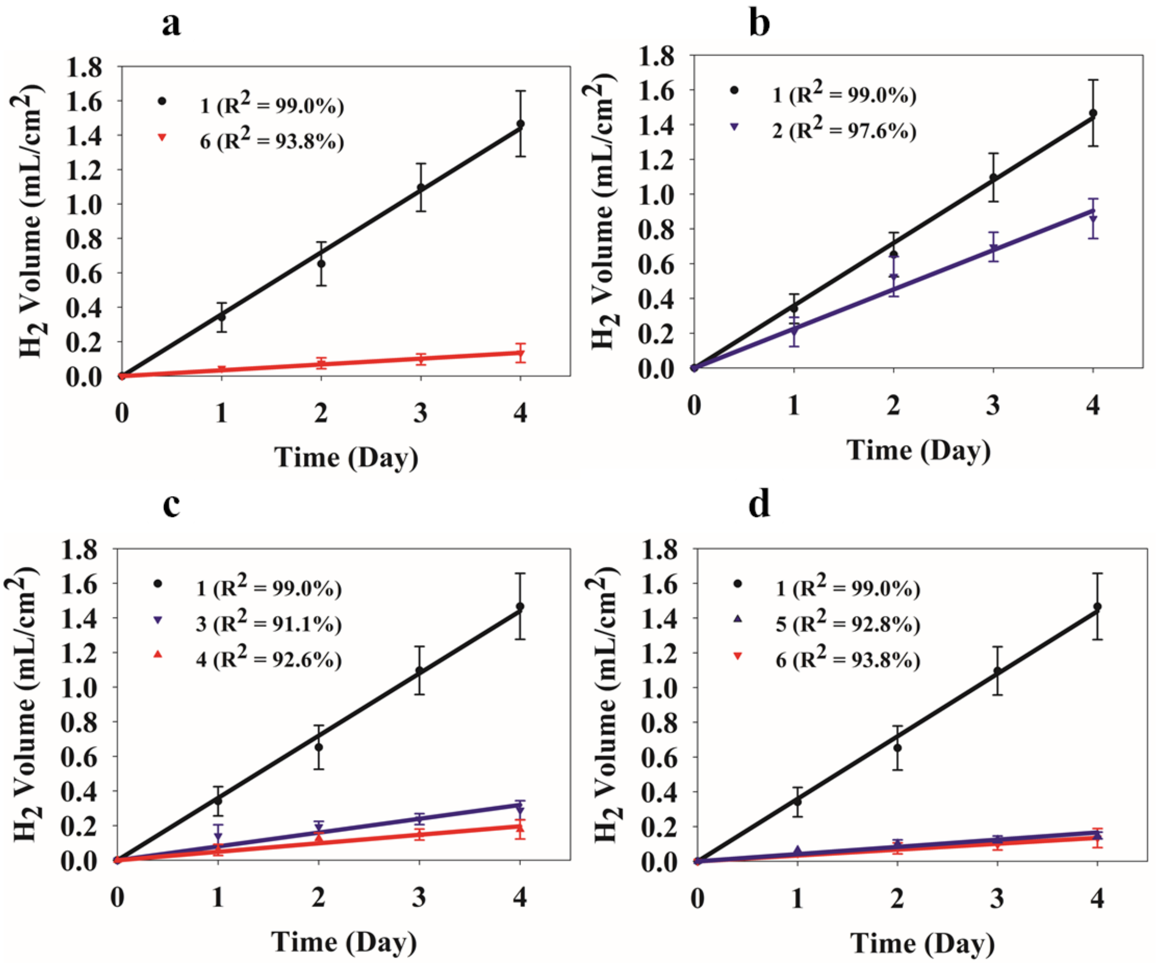

Figure 4.4. Volumetric H_2 measurements for ZEK100 immersed in the different solutions listed in Table 4.1: solution 1: 100 mM NaCl (aq) (baseline); solution 2: 100 mM LiCl (aq); solution 3: 100 mM NaCl (aq) + 3 mM LiOH (aq); solution 4: 100 mM LiCl (aq) + 3 mM LiOH (aq); solution 5: 100 mM NaCl (aq) + 100 mM Na_2CO_3 (aq); solution 6: 100 mM NaCl (aq) + 100 mM Li_2CO_3 (aq). R^2 values listed are for the superimposed linear rate law in each case.

The moles of oxidized Mg were converted to a mass of oxidized Mg, which were then adjusted by dividing by the nominal composition of Mg in the alloy to determine the mass of alloy oxidized. Dividing the mass of alloy oxidized by both the exposed surface area and exposure time yields a corrosion rate (mg/cm^2/day). Bar charts comparing the corrosion rate of ZEK100 in different solutions are presented in Figures 4.5a (for near-neutral solutions) and 4.5b (for alkaline solutions) along with the secant corrosion rate determined from the mass loss measurement made after the 96 h exposure. The corrosion rate data is also listed in Table 4.3. Collectively, the corrosion rate of ZEK100 is lower in the alkaline solutions. The H_2 evolution rate is consistently lower than the mass loss rate, which is an expected based on reported corrosion rate reported for AZ31B immersed in NaCl (aq) [55,62]. The discrepancy is likely explained by a lower H_2 gas collection efficiency than the assumed 100% value. Gas bubbles sticking to the corroding surface and the glass surfaces used to construct the collection apparatus (inverted funnel and upside-down burette) are limitations of this technique [65]. A contribution from oxygen reduction as an additional cathode reaction is also possible. However, it is considered unlikely since a pH of at least 13 is apparently required for such a contribution during corrosion of AZ31B in aqueous alkaline solutions [51]. Despite the discrepancy, the trend in both measurements is the same: corrosion rate decreasing monotonically from solution 1 (baseline) to solution 6 (baseline with dissolved Li_2CO_3).

Table 4.3. Corrosion Rate Data of ZEK100

No.	**pH**	**Solution Composition**	**H_2 Evolution (mL/cm2/day)**	**H_2 Evolution (mg/cm2/day)**	**Mass Loss (mg/cm^2/day)**
1	Near-Neutral (~7)	100 mM NaCl	0.369	0.370 ± 0.02	0.825 ± 0.08
2	Near-Neutral (~7)	100 mM LiCl	0.221	0.221 ± 0.01	0.625 ± 0.02
3	Alkaline (~11)	100 mM NaCl + 3 mM LiOH	0.067	0.073 ± 0.01	0.235 ± 0.04
4	Alkaline (~11)	100 mM LiCl + 3 mM LiOH	0.044	0.044 ± 0.01	0.159 ± 0.02
5	Alkaline (~11)	100 mM NaCl + 100 mM Na_2CO_3	0.035	0.035 ± 0.08	0.109 ± 0.01
6	Alkaline (~11)	100 mM NaCl + 100 mM Li_2CO_3	0.032	0.034 ± 0.01	0.057 ± 0.01

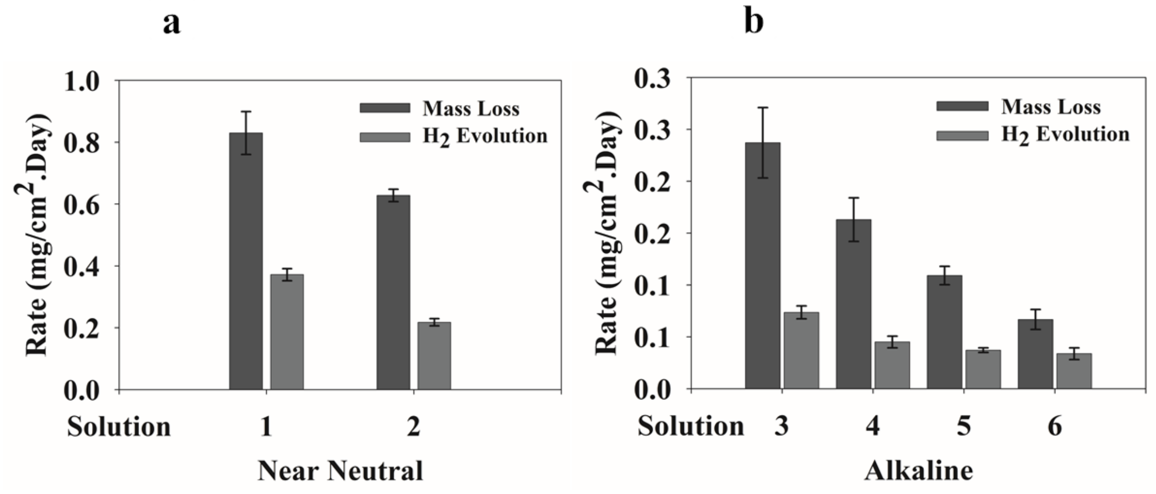

Figure 4.5. Bar char comparing the corrosion rate determined from the single mass loss measured after 96 h exposure against the linear rate determined from the volumetric H_2 evolution measurements: (a) near-neutral (pH ~7) solutions and (b) alkaline (pH ~11) solutions.

Photographic images of ZEK100 after 96 h immersion in the different solutions listed in Table 4.1 are shown in Figure 4.6. Localized filament-like corrosion is observed on the sample immersed in the 100 mM NaCl (aq) baseline solution (Figure 4.6a). Replacing 100 mM NaCl (aq) with 100 mM LiCl (aq) does not change the corrosion mode as this sample also reveals localized filament-like corrosion. Despite the significant reduction in corrosion rate that is observed with the addition of 3 mM LiOH to the baseline solution, localized filament-like corrosion is again observed on the surface, albeit with mush less surface coverage. The remaining samples immersed in the alkaline solutions exhibited no evidence (by the unaided eye) of localized filament-like corrosion. There are no defining features on any of these corroded surfaces that be linked to the difference in corrosion rate observed, as shown by Figure 4.5b and Table 4.3.

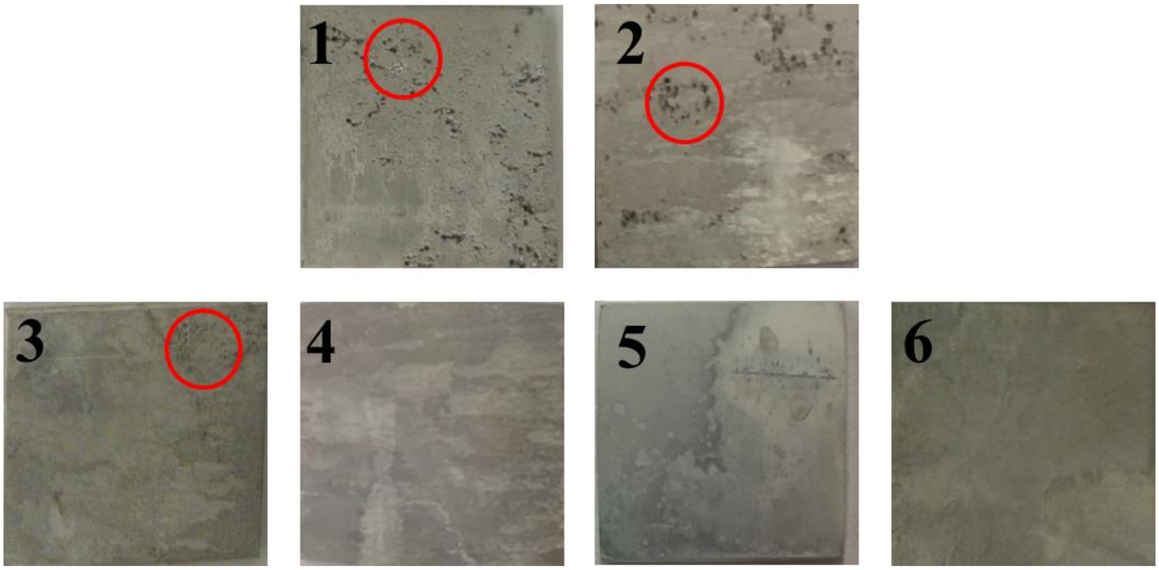

Figure 4.6. Photographic images of the ZEK100 surface after 96 h immersion in the different solutions listed in Table 4.1: solution 1: 100 mM NaCl (aq) (baseline); solution 2: 100 mM LiCl (aq); solution 3: 100 mM NaCl (aq) + 3 mM LiOH (aq); solution 4: 100 mM LiCl (aq) + 3 mM LiOH (aq); solution 5: 100 mM NaCl (aq) + 100 mM Na_2CO_3 (aq); solution 6: 100 mM NaCl (aq) + 100 mM Li_2CO_3 (aq). Superimposed cycles show regions were localized filament-like corrosion is present.

High resolution XPS spectra for C 1s, O 1s and Mg 1s acquired from the intact surface film formed on ZEK100 after 2.5 h immersed in 100 mM NaCl (aq) with and without dissolved Li_2CO_3 are shown in Figure 4.7. Li was not detected by the survey scan conducted on the as-received surface or on the surface after a gentle sputter cleaning for the sample immersed with dissolved Li_2CO_3. The C 1s spectrum is shown in Figure 4.7a. Both surface films exhibit a low binding energy peak around 284 eV. This peak was assumed to be associated with adventitious C and, thus the peak value of 284.8 eV [66] was used for calibration. The high binding energy peak, with higher intensity, at 289.4 eV acquired from the surface film formed with dissolved Li_2CO_3 is within the range reported for metal carbonates (288-290 eV) [66]. Since Li was not detected, the metal carbonate is most likely $MgCO_3$. The Mg 1s spectrum is shown in Figure 4.7b. Only one relatively broad binding energy peak was acquired from both surface films. Overlapping peaks involving $MgO/Mg(OH)_2$ (1304.5 eV) [66] and $MgCO_3$ (1305 eV) [66] likely combine to yield the single relatively broad peak observed. The O 1s peak is shown in Figure 4.7c. Again, only one relatively broad binding energy peak was acquired from both surface films. Overlapping peaks involving metal oxide/hydroxide (529-530 eV) [66] and metal carbonate (531.5-532 eV) [66] likely combine to yield the single relatively broad peak observed.

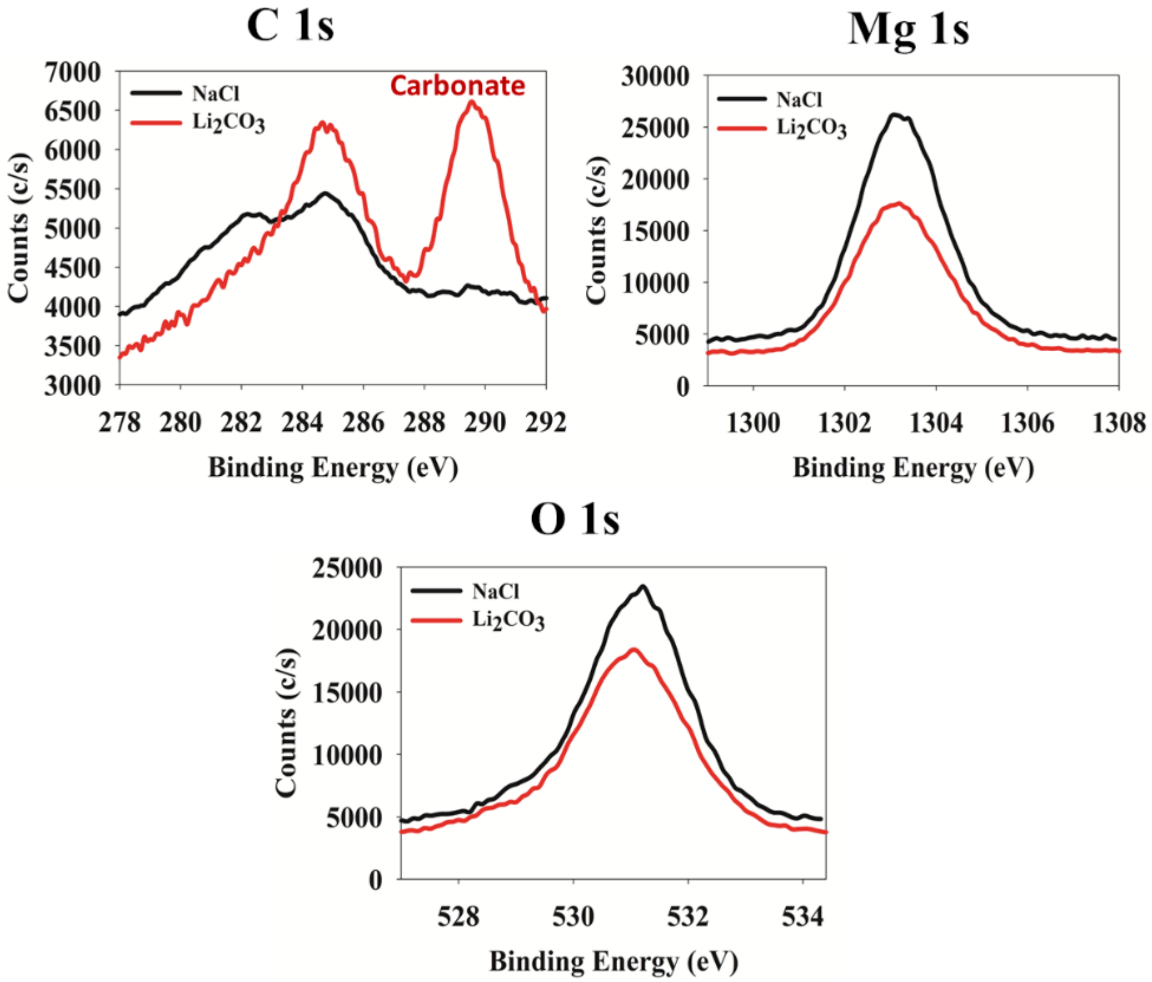

Figure 4.7. High resolution C 1s, Mg 1s and O 1s peaks acquired by XPS from the intact surface formed after 2.5 h immersion in 100 mM NaCl (aq) with dissolved Li_2CO_3 (pH ~11).

Figure 4.8 shows images of ZEK100 after potentiostatic anodic polarization in 100 mM NaCl (aq) with 100 mM Na_2CO_3 (aq) and with 100 mM Li_2CO_3 (aq). No evidence of localized breakdown is found on either surface (Figures 4.8a and 4.8b), even under higher magnification using SEM (Figures 4.8c and 4.8d). The anodic film formed in both alkaline carbonate inhibiting solutions reveals a similar morphology (Figures 4.8c and 4.8d): one consisting of compact platelets.

A high-angle annular dark-field (HAADF) image the anodic film formed on ZEK100 in 100 mM NaCl (aq) with 100 mM Na_2CO_3 (aq) is shown in Figure 4.9 along with an associated STEM-EELS maps for Mg, Zn and Zr (metal) and Na, C and O (solution). The acquired (STEM-EDS) Cl map is presented later together with one acquired from the anodic film formed with dissolved Li_2CO_3 (Figure 4.12). The HAADF image shows the anodic film consists of two layers: a thicker porous layer residing on top of a thinner compact layer. Both layers consist of Mg, O and C as major film forming elements. The porous nature of the outer layer is also reflected on the O map as the dark regions. Zn is enriched at the film/metal interface as a reasonably continuous thin layer, as well as within particles present within the film and metal. Zr is enriched only within particles present within the metal. Na is enriched at extreme surface of the film (C deposit/film interface). There is also some enrichment at the film/metal interface. A composite Na + Zn map is shown rather than just a standalone Na map to better differentiate between the two elements considering the relative position of the respective peaks: 1072 eV for Na and 1043 eV for Zn [67].

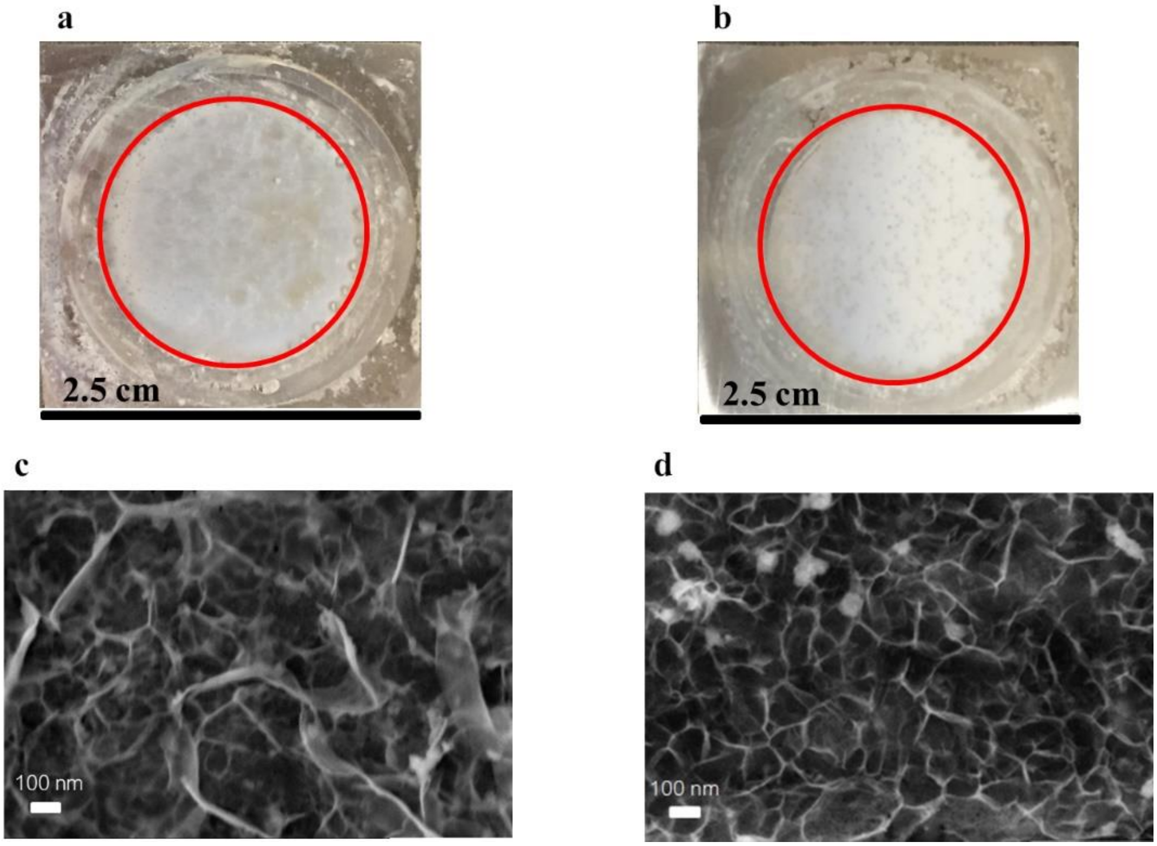

Figure 4.8. Photographic and secondary images of the ZEK100 surface after anodic potentiostatic polarization in 100 mM NaCl (aq) with (a) and (c) 100 mM Na_2CO_3 (aq) (pH ~11) and (b) and (d) 100 mM Li_2CO_3 (aq) (pH ~11).

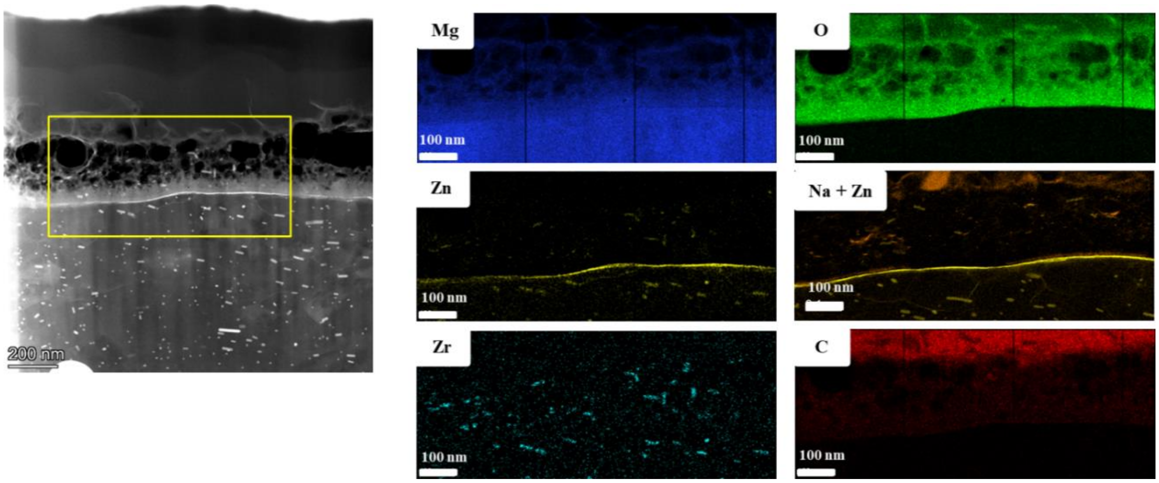

Figure 4.9. HAADF image of the anodic film formed in 100 mM NaCl (aq) with 100 mM Na_2CO_3 (aq) and associated STEM-EELS mapping showing the elemental composition of the film/metal interface.

Figure 4.10 shows a HAADF image the anodic film formed on ZEK100 in 100 mM NaCl (aq) with 100 mM Li_2CO_3 (aq) along with an associated STEM-EELS maps for Mg, Zn and Zr (metal) and Li, C and O (solution). Again, the HAADF image shows the anodic film consists of a thicker porous outer layer residing on a thinner compact inner layer. Unlike the case for Na, Li is clearly incorporated in both layers along with Mg, O and C. O-containing platelets extend into the C layer deposited on the surface. Li incorporation is absent in these platelets. Zn is again enriched at the film/metal interface and within particles present in both the film and metal. Zr is only enriched in particles present in both the film and metal.

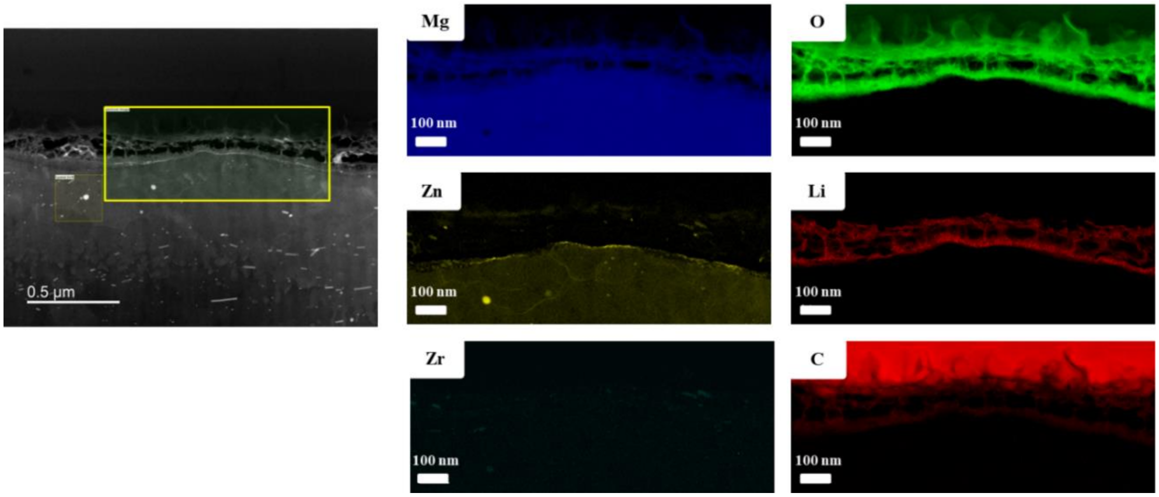

Figure 4.10. HAADF image of the anodic film formed on ZEK100 immersed in 100 mM NaCl (aq) with 100 mM Li_2CO_3 (aq) and associated STEM-EELS mapping showing the elemental composition of the film/metal interface.

Bright field images of the anodic film formed in the two alkaline carbonate solutions are shown in Figure 4.11 along with an acquired SAED pattern from the region of interest (dense inner layer) identified on each bright field image. A ring pattern in both cases implies that the dense inner layer is polycrystalline and comprised of ultrafine grains. The acquired pattern was compared against reference patterns calculated using the PDF-4+-2021 software [68] for possible compounds including MgO (periclase), $Mg(OH)_2$ (brucite), $MgCO_3$ (magnesite), $MgCO_3 \cdot 3H_2O$ (nesquehonite) and $3MgCO_3 \cdot Mg(OH)_2 \cdot 3H_2O$ (hydromagnesite). Of these expected compounds, MgO provides the best match, as shown by the agreement between the superimposed reference pattern and the acquired pattern.

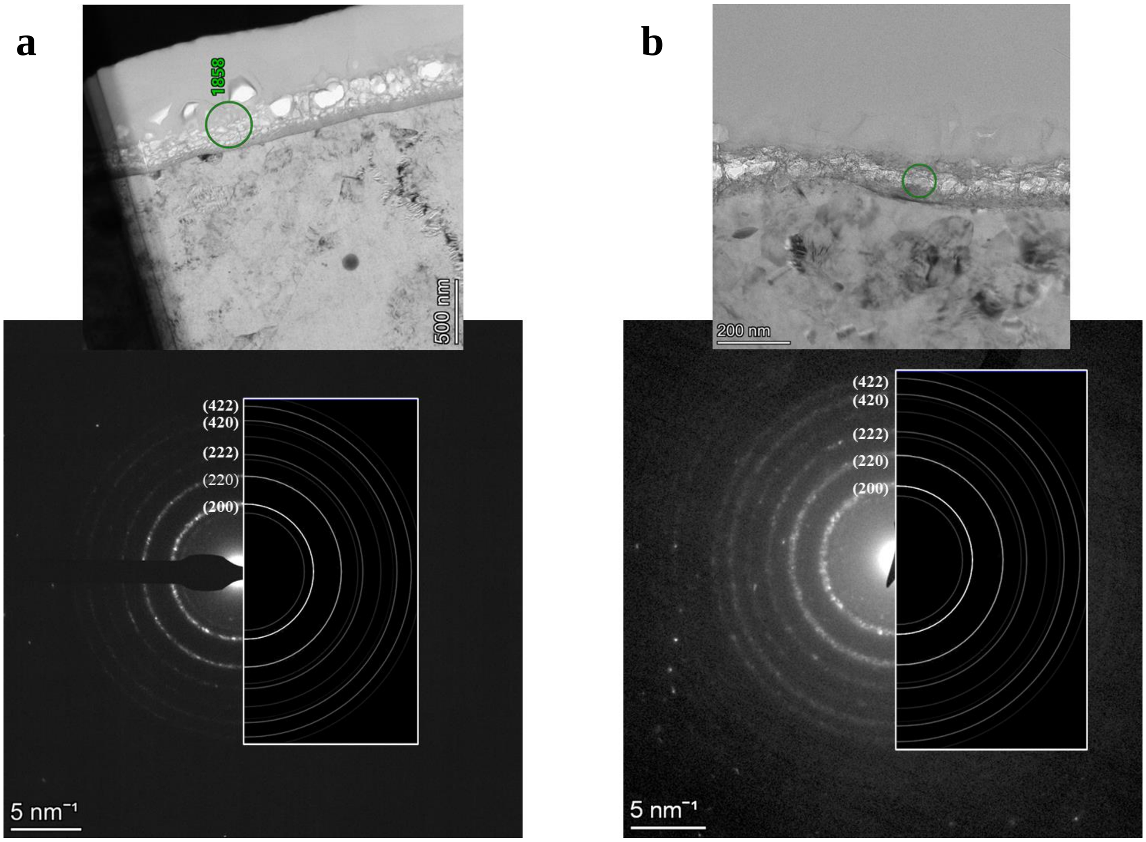

Figure 4.11. Bright field images and associated SAED patterns acquired from the dense inner film formed on ZEK100 immersed in 100 mM NaCl (aq) with (a) 100 mM Na_2CO_3 (aq) and (b) 100 mM Li_2CO_3 (aq).

The STEM-EDS Cl maps acquired from both anodic films are shown in Figure 4.12. Although Cl is incorporated into both anodic films, the distribution is significantly different. The distribution is non-uniform in the anodic film formed with dissolved Na_2CO_3 (aq). There is significant enrichment at the film/metal interface. In contrast, the distribution is significantly more uniform in the anodic film formed with dissolved Li_2CO_3 (aq). The uniform distribution is present in both the layers (thicker, porous outer layer and thinner, dense inner layer).

A simple experiment consisting of a cathodic polarization scan (1 mV/s) initiated from the open-circuit potential (after 10 minutes conditioning) before and after a potentiostatic anodic polarization step (150 mV more positive than OCP for 30 minutes) was conducted to test the theory about the suppression of cathode activation. Such a sequence readily shows the extent of cathode activation by a significant increase in the cathode kinetics after polarization.[23] Figure 4.13 shows the results for ZEK100 immersed in baseline near-neutral solution 1 and the two alkaline carbonate solutions 5 and 6. Cathode activation is clearly observed in the baseline solution 1, but is clearly suppressed in the two alkaline carbonate solutions 5 and 6. A more systematic approach to quantify the extent of cathodic activation would be applying an equivalent anodic charge pulse rather than the same overpotential, complete with a detailed characterization of the structure and composition of the surface film formed after each pulse.

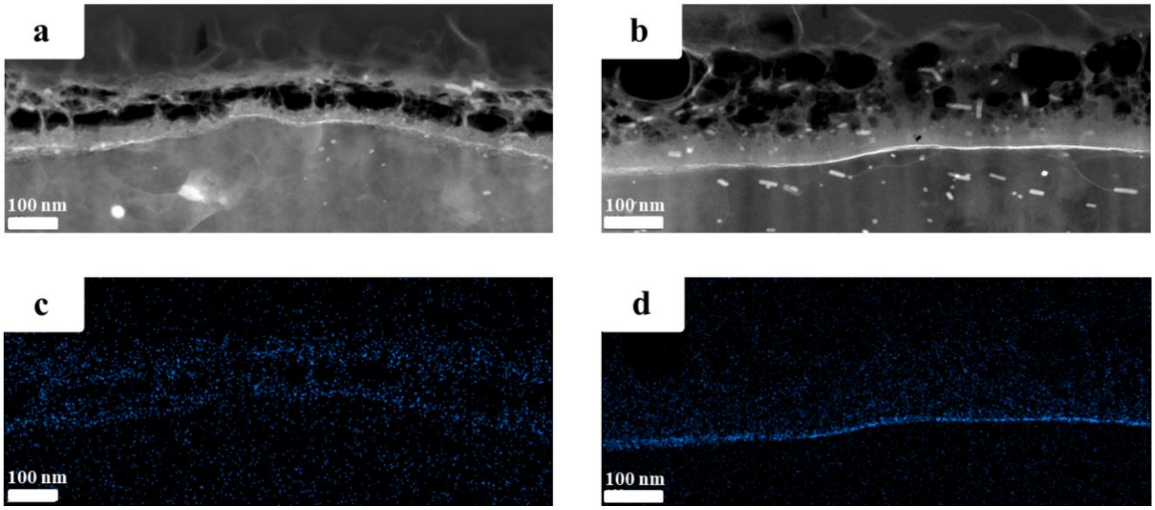

Figure 4.12. HAADF image of the anodic film formed on ZEK100 immersed in 100 mM NaCl (aq) with 100 mM Na_2CO_3 (aq) and with 100 mM Li_2CO_3 (aq) and associated STEM-EDS mapping showing the Cl distribution with each film.

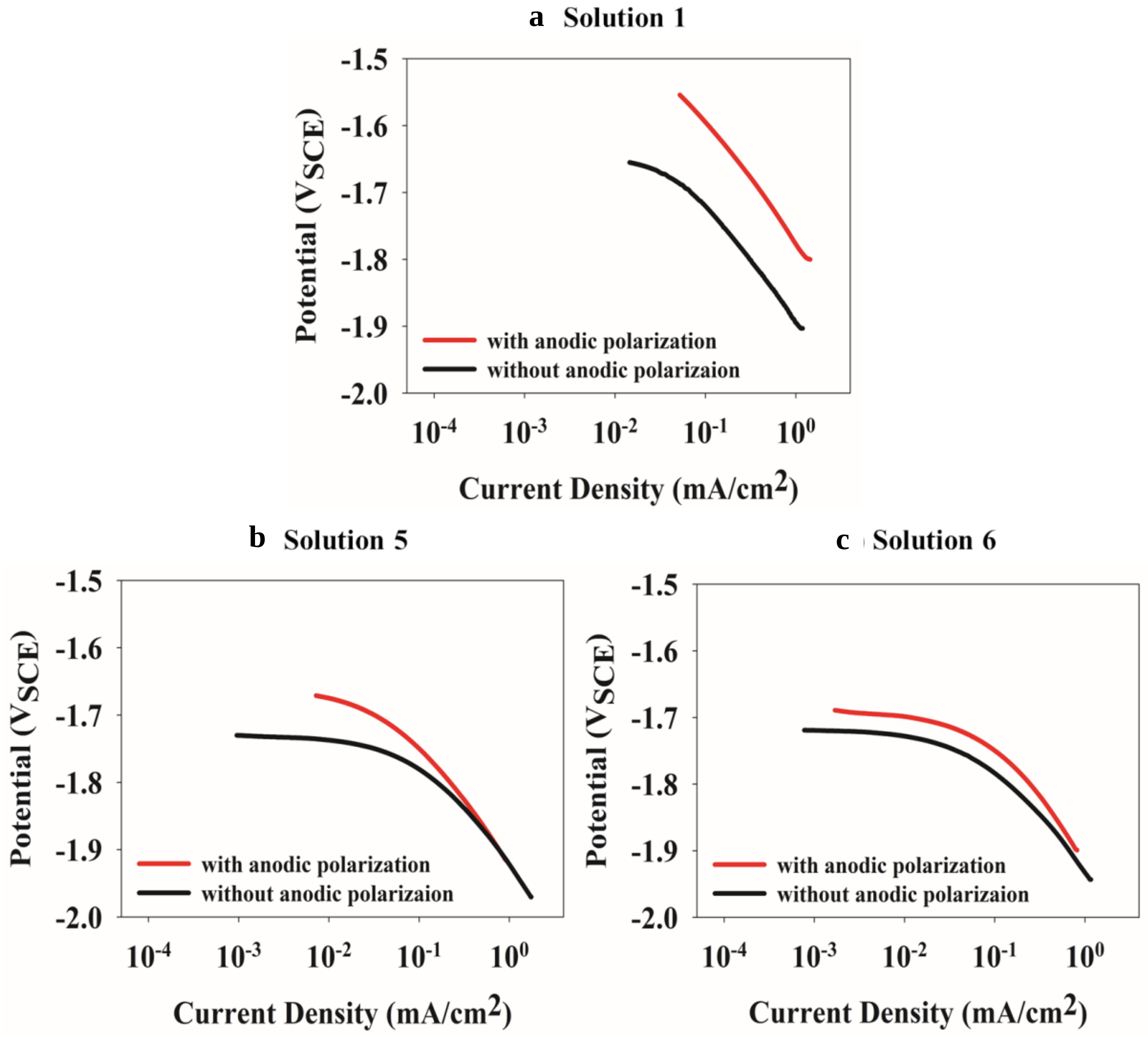

Figure 4.13. Cathodic polarization scans (1 mV/s) initiated from the open-circuit potential (after 10 minutes conditioning) before and after a potentiostatic anodic polarization step (150 mV more positive than OCP for 30 minutes) for ZEK100 immersed in (a) solution 1: 100 mM NaCl (aq) (baseline), (b) solution 5: 100 mM NaCl (aq) with 100 mM Na_2CO_3 (aq), and (c) solution 6: 100 mM NaCl (aq) with 100 mM Li_2CO_3 (aq).

4.5 Discussion

The addition of 100 mM Li_2CO_3 (aq) to 100 mM NaCl (aq) serves as an effective corrosion inhibitor for ZEK100. The addition reduced the corrosion rate (mg/cm^2/day) from 0.82 ± 0.08 mg/cm^2/day (mass loss) and 0.37 ± 0.03 (H_2 evolution) in absence of dissolved Li_2CO_3 to 0.06 ± 0.01 (mass loss) and 0.03 ± 0.01 (H_2 evolution) with dissolved Li_2CO_3: a reduction by a factor of 14 and 12 for the rate determined by mass loss and H_2 evolution respectively. The chemistry of dissolved Li_2CO_3 can be summarized as follows, with the equilibrium solubility product (k_{sp}) and base (k_b) constants quoted for 298 K [69]:

$$Li_2CO_3(s) \rightarrow 2Li^+(aq) + CO_3^{-2}(aq) \quad k_{sp} = 8.15 \times 10^{-4} \tag{2}$$

$$CO_3^{2-}(aq) + H_2O \rightarrow HCO_3^-(aq) + OH^-(aq) \quad k_b = 2\times10^{-4} \tag{3}$$

As indicated by the data tabulated in Table 4.3, inhibition involves the combinatory effect of dissolved Li^+ (aq), OH^- (aq) and CO_3^{2-}/HCO_3^- (aq). Removal of either the dissolved Li^+ (aq) or CO_3^{2-}/HCO_3^- (aq) increases the corrosion rate of ZEK100 relative to the dissolved Li_2CO_3 case, with the removal of CO_3^{2-}/HCO_3^- (aq) showing the greater increase.

Although effective at reducing the corrosion rate, dissolved Li_2CO_3 does not alter the kinetics rate law exhibited by ZEK100 during corrosion in 100 mM NaCl (aq). Recently, in-situ Raman spectroscopy (RMS) and associated kinetic Raman mapping (KRM) has revealed that Mg corrosion in alkaline NaCl (aq) (pH 9-11) follows a linear rate late and involves the formation of non-passivating $Mg(OH)_2$ surface film via initial dissolution of Mg and subsequent precipitation of $Mg(OH)_2$, with the latter process being rate-controlling [52]. Corrosion of ZEK100 in the alkaline carbonate solutions involves three major processes: (i) anodic dissolution (anode) at the film/metal interface, (ii) H_2 evolution (cathode), presumably at the film/solution interface in the absence of localized corrosion initiation and (iii) film formation. Thus, one of these three processes is rate-controlling (linear rate kinetics).

Global anodic polarization, where the global cathode is moved off the dissolving ZEK100 surface to the counter electrode, shows a significantly more polarizable anodic dissolution reaction in the alkaline carbonate solutions relative to the near-neutral baseline solution. This increased polarizability is consistent mixed type of control: one involving both activation and concentration polarization contributions. Diffusion of Mg^{2+} through the thinner dense inner layer is the likely responsible for the concentration polarization contribution. As such, the anodic dissolution is likely not rate-controlling. XPS surface analysis indicates that the surface film formed on ZEK100 during corrosion (open-circuit) the alkaline carbonate solutions is comprised of $MgO/Mg(OH)_2$ and $MgCO_3$, with the latter being formed predominantly as a thin outermost layer (depth profiles not shown here). Under anodic polarization, TEM-SAED analysis indicates that the surface film formed on ZEK100 during enhanced anodic dissolution is comprised of MgO, with significant Li incorporation when formed in dissolved Li_2CO_3. When formed on Mg-Li-(Al-Y-Zr) alloy during corrosion in NaCl (aq), such a film has been described as being Li-doped MgO [58]. A dense MgO inner layer, when formed in alkaline solutions relative to near-neutral solution, can be explained by slower MgO hydration kinetics in alkaline solutions [70,71]. Hydration is the first step in the overall transformation to $Mg(OH)_2$ through a dissolution-precipitation process [72] :

$$MgO + H_2O \rightarrow MgO \cdot HOH \rightarrow Mg^{2+}(aq) + 2OH^-(aq) \square \quad Mg(OH)_2(s) \tag{4}$$

Slower hydration kinetics serves to reduce the likelihood for stress-rupture of the intact MgO induced by the increased molar volume of $Mg(OH)_2$ transformation product [73,74]. It is unclear at this time how Li incorporated into MgO further inhibits the anode kinetics relative to the dense MgO film that forms in dissolved Na_2CO_3.

The possible formation Mg carbonates as the dense inner layer was considered on the basis that precipitation from salt lake brines via additions of dissolved Na_2CO_3 (aq) is candidate process to selectively remove Mg prior to Li extraction [75-77]. The precipitation chemistry can be summarized as follows:

$$Mg^{2+}(aq) + CO_3^{2-}(aq) + 3H_2O \rightarrow MgCO_3 \cdot 3H_2O\ (s) \tag{5}$$

$$5Mg^{2+}(aq) + 4CO_3^{2-}(aq) + 2OH^-(aq) + 3H_2O \rightarrow 3MgCO_3 \cdot Mg\left(OH\right)_2 \cdot 3H_2O\ (s) \tag{6}$$

Without an excess of CO_3^{2-} (aq), $MgCO_3 \cdot 3H_2O$ (nesquehonite) tends to from (Equation 5), whereas $MgCO_3 \cdot Mg(OH)_2 \cdot 3H_2O$ (hydromagnesite) tends to form with an excess CO_3^{2-} (aq) (Equation 6). Formation of hydromagnesite as the principle corrosion product, in place of MgO/$Mg(OH)_2$, during atmospheric corrosion has been reported for Mg alloys [78-80]. However, the TEM-SAED analysis ruled out any such formation.

The platelet morphology of the outer layer is expected of a precipitation reaction [81]. Precipitate morphology is strongly dependent on the supersaturation index, which is the ratio of the solute concentration in excess relative to the solute concertation at equilibrium. A relatively high supersaturation favors crystal growth and the formation of a less compact precipitate, whereas a relatively low supersaturation favors crystal nucleation and the formation of a more compact precipitate [82]. Thus, the bi-layer structure of the anodic film formed in the dissolved carbonate solution can be rationalized in the following way. Anodic polarization causes the rapid accumulation of Mg^{2+} (aq) at the dissolving interface, in addition to MgO film formation at the metal/film interface [83], creating supersaturated solution at the film/solution interface. Precipitation of the presumably $Mg(OH)_2$ outer layer begins once a critical value is achieved. Since both MgO and $Mg(OH)_2$ film formation processes occur during anodic dissolution, neither is expected to be rate-controlling given the overall mixed control exhibited by the anode polarization kinetics.

Global cathodic polarization, where the global anode is moved off the ZEK100 surface to the counter electrode, shows only a reduction in current density, not polarizability, in the alkaline carbonate solutions relative to the near-neutral baseline solution. Here, activation polarization is the dominant contribution to the cathode kinetics, which, if rate-controlling, can account for the linear corrosion kinetics. The expected shift in the equilibrium half-cell potential of the H_2 evolution reaction to lower values in the alkaline solution is the simplest explanation for the inhibited cathode kinetics observed in the alkaline solutions. However this does not explain the additional inhibition exhibited with Li^+ (aq) present. Inspection of the global cathode kinetics compared in Figure 4.3, Li^+ (aq) has no effect on the cathode kinetics (H_2 evolution) in near-neutral solutions, but decreased cathode kinetics are observed in alkaline solutions with Li^+ (aq) present. Recently, it has been shown the dissolved Li^+ (aq) can alter the H_2 evolution kinetics on metal electrodes immersed in aqueous electrolytes, either increasing or decreasing depending on the metal [84,85]. DFT calculations indicates that Li^+ moderates the Gibbs free energy of H adsorption. For those metals that show decreased HER kinetics, Li^+ moves the Gibbs free energy for H adsorption away from a favorable thermo-neutral energy value, thereby weakening H adsorption.[85] Therefore, a similar moving away from the favaorable thermo-neutral energy value is suspected in this case. DFT studies have also revealed that the Volmer-Heyrovsky is the dominant pathway for the HER, albeit for the bare (unfilmed) Mg surface [86.87]. Therefore, the Heyrovsky step is the one that is most likely affected. In addition to a reduction in the both the global anode and cathode kinetics, alkaline carbonate solutions also suppress localized filament-like corrosion and associated anode/cathode activation. Initiation requires the localized breakdown of the surface film that forms initially during corrosion as a precursor event [17-19]. As Table 4.3 shows, breakdown of the intact film occurs in the alkaline carbonate solutions (albeit delayed, more so with dissolved Li_2CO_3), but the transition to filament-like corrosion is not observed (Figure 4.6). The slow hydration-induced transformation of MgO to $Mg(OH)_2$ when formed at a local dissolving anode site could be responsible for the transition suppression observed. $Mg(OH)_2$ has been shown to catalyze H_2 evolution on Mg, more so when freshly formed [18,88]. Density functional theory (DFT) simulations indicate that $Mg(OH)_2$ is an effective water splitter that can enhance the efficiency of water splitting (H_2 evolution cathode reaction) relative to the bare Mg metal surface [89]. The formation of $MgCO_3$, in place of $Mg(OH)_2$ at dissolving anode sites on Mg exposed in 0.1 M $NaHCO_3$ (pH ~8.4) has been argued as the likely cause for the absence of cathodic activation as observed on the anodically-dissolved surface during subsequent cathodic potentiodynamic polarization [90]. However the TEM-SAED analysis of the surface films formed during anodic polarization in alkaline carbonate solutions does not support that claim. Finally, the incorporation of Cl^- (aq) into surface film is a precursor event for film breakdown [91,92]. It follows then that the ability for Li, when incorporated into the surface film formed during anodic dissolution, may also be contributing to the improved corrosion control by not allowing Cl^- (aq) to enrich at the film/metal interface.

4.6 Conclusions

1. Dissolved Li_2CO_3 (aq) significantly inhibits corrosion of ZEK100 in 100 mM NaCl (aq) at ambient temperature. The addition of 100 mM (just below saturation) reduces corrosion by a factor of ~12. Inhibition involves the combinatory effect of dissolved Li^+ (aq), OH^- (aq) and CO_3^{2-}/HCO_3^- (aq). Removal of either the dissolved Li^+ or CO_3^{2-}/HCO_3^- increases the corrosion rate of ZEK100 relative to the dissolved Li_2CO_3 case, with the removal of CO_3^{2-}/HCO_3^- showing the greater increase.
2. Inhibition does not alter the rate law. Linear kinetics is observed in all solutions considered. Of the major process involved in corrosion, the cathode seems to be rate-controlling. Critical factors are argued to be the lower equilibrium half-cell potential combined with the incorporation of Li into the surface film, which serves to de-catalyze H_2 evolution on the filmed surface.
3. Inhibition also involves the suppression of the localized filament-like corrosion and associated anode/cathode activation. The slow hydration-induced transformation of

MgO to $Mg(OH)_2$ at a local dissolving anode site combined with the ability of Li to de-catalyze local H_2 evolution on the film surface at a dissolving anode site may be responsible for the suppression.

4.7 Acknowledgments

Funding (operating) was provided by Natural Science and Engineering Research Council (NSERC) under the Discovery Grants program (RGPIN-2020-05727). Funding (student stipend and living allowance for B. Zaghloul) was provided by the Egyptian Armament Authority (EAA). Thanks to D. Pallisco and Dr. J.R McDermid for assisting with the indexing of the SAED patters. The Canadian Centre for Electron Microscopy (CCEM) is a national facility supported by NSERC, Canada Foundation for Innovation (CFI), under the MSI program, and McMaster University.

4.8 References

1. W. J. Joost, JOM, 64, 1032 (2012).

2. W. J. Joost and P. E. Krajewski, Scr. Mater., 128, 107 (2017).

3. A. A. Luo, R. Shi, J. Miao, and T. Avey, JOM, 73, 1402 (2021).

4. R. C. McCune, J. Forsmark, B. Schneider, A. Luo, H. Gu, W. Schumacher, X. Chen, and F. Vartolas, SAE Int. J. Mater. Manf., 6, 242 (2013).

5. M. P. Brady, W. J. Joost, and C. D. Warren, Corrosion, 73, 452 (2016).

6. M. Liu, Y. Guo, J. Wang, and M. Yergin. NPJ Mater. Degrad., 24, 1 (2018).

7. G. Williams, H. ap Llwyd Dafydd, and R. Grace, Electrochim. Acta, 109, 489 (2013).

8. Z. P. Cano, M. Danaie, J. R. Kish, J. R. McDermid, G. A. Botton, and G. Williams, Corrosion, 71, 146 (2015).

9. Z. P. Cano, J. R. Kish, and J. R. McDermid, J. Electrochem. Soc., 163, C732 (2016).

10. M. A. Melia, T. W. Cain, B. F. Briglia, J. R. Scully, and J. M. Fitz-Gerald, JOM, 69, 2322 (2017).

11. L. G. Bland, L. C. Scully, and J. R. Scully, Corrosion, 73, 526 (2017).

12. R. M. Asmussen, W. J. Binns, P. Jakupi, and D. Shoesmith, Corrosion, 71, 242 (2015).

13. M. P. Brady, D. N. Leonard, E. A. McNally, J. R. Kish, H. M. Meyer III, E. Cakmak, and B. Davis, J. Electrochem. Soc. 166, C492 (2019).

14. C. Kousis, N. McMurray, P. Keil, and G. Williams, Corrosion, 77, 156 (2021).

15. H. M. Krebs, A. Chirazi, L. Lechner, J. Gelb, X. Zhou, G. E. Thompson, and P. J. Withers, Frontiers in Materials Processing, Applications, Research and Technology (Singapore: Springer, 2018) pp. 165-177.

16. L. G. Bland, N. Birbilis, and J. R. Scully, J. Electrochem. Soc., 163, C895 (2016).

17. D. Rossouw, D. Fu, D. N. Leonard, M. P. Brady, G. A. Botton, and J. R. Kish, Corrosion, 5, 518 (2017).

18. S. Fajardo, C. F. Glover, G. Williams, and G. S. Frankel, Corrosion, 5, 482 (2017).

19. E. Michailidou, H. N. McMurray, and G. Williams, J. Electrochem. Soc., 5, C195 (2018).

20. S. Thomas, N. V. Medhekar, G. S. Frankel, and N. Birbilis, Curr. Opin. Solid State Mater. Sci., 19, 85 (2015).

21. G. S. Frankel, A. Samaniego, and N. Birbilis, Corros. Sci., 70, 104 (2013).

22. J. A. Yuwono, C. D. Taylor, G. S. Frankel, N. Birbilis, and S. Fajardo, Electrochem. Comm., 104, 106482 (2019).

23. M. Taheri, J. R. Kish, N. Birbilis, M. Danaie, E. A. McNally, and J. R. McDermid, Electrochim. Acta, 116, 396 (2014).

24. T. Cain, S. B. Madden, N. Birbilis, and J. R. Scully, J. Electrochem. Soc., 162, C228 (2015).

25. N. Birbilis, T. Cain, J. S. Laird, X. Xia, J. R. Scully, and A. E. Hughes, ECS Electrochem. Lett. 4, C34 (2015).

26. D. Hoche, C. Blawert, S. V. Lamaka, N. Scharnagl, C. Mendis, and M. L. Zheludkevich, Phys. Chem. Chem. Phys. 18, 1279 (2016).

27. J. Li, W. Sun, B. Hurley, A. A. Luo, and R. G. Buchheit, Corros. Sci. 112, 760 (2016).

28. S. H. Salleh, S. Thomas, J. A. Yuwono, K. Venkatesan, and N. Birbilis, Electrochim. Acta 161, 144 (2015).

29. W. J. Binns, F, Zargarzadah, V. Dehnavi, J. Chen, J. J. Noël, and D. W. Shoesmith, Corrosion, 75, 58 (2019).

30. X. B. Chen, N. Birbilis, and T. B. Abbott, Corrosion, 67, 035005-1 (2011).

31. J. E. Gray and B. Luan, J. Alloys Compd., 336, 88 (2002).

32. J. Wang, X. Pang, and H. Jahed, AIMS Mater. Sci., 6 567 (2019).

33. J.K. Lin and J. Y. Uan, Corros. Sci., 51, 1181 (2009).

34. J. Chen, Y. Song, D. Shan, and E-H. Han, Corros. Sci., 53 3281 (2011).

35. R. C. Zeng, Z. G. Liu, F. Zhang, S. Q. Li, H. Z. Cui, and E.H. Han, J. Mater. Chem. A, 2, 13049 (2014).

36. V. Zahedi Asl, J. Zhao, M. J. Anjum, S. Wei, W. Wang, and Z. Zhao, J Alloys Compd, 821, 153248 (2020)

37. G. Zhang, E. Jiang, L. Wu, W. Ma, H. Yang, A. Tang, and F. Pan, Scientific Reports, 11 1 (2021)

38. J. K. E. Tan, P. Balan, and N. Birbilis, Appl. Clay Sci., 202, 105948 (2021).

39. M. Tabish, G. Yasin, M. J. Anjum, M. U. Malik, J. Zhao, Q. Yang, S. Manzoor, H. Murtaza, and W. Q. Khan, J. Mater. Res. Technol., 10, 390 (2021).

40. H. Gao, Q. Li, Y. Dai, F. Luo, and H. X. Zhang, Corros. Sci., 52, 1603 (2010).

41. D. Eaves, G. Williams, and H.N. McMurray, Electrochim. Acta, 79, 1 (2012).

42. A. Frignani, V. Grassi, F. Zanotto, and F. Zucchi, Corros. Sci., 63, 29 (2012).

43. N. Dinodi and A.N. Shetty, Corros. Sci., 85, 411 (2014).

44. S. V. Lamaka, D. Höche, R. P. Petrauskas, C. Blawert, and M. L. Zheludkevich, Electrochem. Commun., 62, 5 (2016).

45. S. V. Lamaka, B. Vaghefinazari, Di Meia, R.P. Petrauskas, D. Höche, and M. L. Zheludkevich, Corros. Sci., 128, 224 (2017).

46. G. Williams, H. N. McMurray, and R. Grace, Electrochim. Acta, 55, 7824 (2010).

47. G. Williams, R. Grace, and R. M. Woods, Corrosion 71 (2015): p. 184.

48. Z. Feng, B. Hurley, J. Li, and R. Buchheit, J. Electrochem. Soc. 165 (2018): p. 94.

49. Z. Feng, B. Hurley, R. Buchheit, M. Zhu, Z. Yang, and J. Hwang, J. Electrochem. Soc. 166 (2019): p. 520.

50. W. Xu, N. Birbilis, G. Sha, Y. Wang, J. E. Daniels, Y. Xiao, and M. Ferry, Nat. Mater., 14. 1229 (2015).

51. S. Li, A. C. Bacco, N. Birbilis, and H. Cong, Corros. Sci., 112, 596 (2016).

52. A. Maltseva, V. Shkirskiy, G. Lefèvre, and P. Volovitch, Corros. Sci., 153, 272 (2019).

53. B.R, Fazal and S. Moon, J. Korean Inst. Surf. Eng., 50, 147 (2017).

54. L. Prince, M. A. Rousseau, X. Noirfalise, L. Dangreau, L. B. Coelho, and M-G. Olivier, Corros. Sci., 179, 109131 (2021).

55. B. Zaghloul, C. F. Glover, J. R. Scully, and J. R. Kish, Corrosion, 77, 192 (2021).

56. Y. M. Yan, O. Gharbi, A. Maltseva, X. B. Chen, Z. R. Zeng, S. W. Xu, W. Q. Xu, P. Volovich, M. Ferry, and N. Birbilis, Corrosion, 75, 80 (2019).

57. Y. Yan, Y. Qiu, O. Gharbi, N. Birbilis, and P. N. H. Nakashima, Appl. Surf. Sci., 494, 1066 (2019).

58. Y. M. Yan, A. Maltseva, P. Zhou, X. J. Li, Z. R. Zeng, O. Gharbi, K. Ogle, M. La Haye, M. Vaudescal, M. Esmaily, and N. Birbilis, Corros. Sci., 164, 108342 (2020).

59. A. Javaid and F. Czerwinski, J. Magnes. Alloy, 7 27 (2019).

60. A. Javaid, A. Hadadzadeh, and F. Czerwinski, J. Alloy Compd., 782, 132 (2019).

61. W. Cheng, Z. Li, and F. Cheng, J. Chem. Thermodyn., 67, 74 (2013).

62. L. G. Bland, A. D. King, N. Birbilis, and J. R. Scully, Corrosion, 71, 128 (2015).

63. C F. Glover, C. F., R. L. Liu, E. A. McNally, S. Mahboubi, J. R. McDermid, J. R. Kish, N. Birbilis, H. N. McMurray, and G. Williams, Corrosion 77, 134 (2021).

64. G. Williams, H. ap Llwyd Dafydd, R. Subramanian and H.N. McMurray, Corrosion, 73, 471 (2017).

65. N.T. Kirkland, N. Birbilis, and M. P Staiger, Acta Biomater. 8 (2012): p. 925.

66. Thermo Fischer Scientific Inc., https://xpssimplified.com/periodictable.php

67. Gatan, Inc., https://eels.info/atlas

68. S. Gates-Rector and T. Blanton, Powder Diffr. 34, 352 (2019).

69. CRC Handbook for Chemistry and Physics, 101st Edition, J. Rumble, editor (Boca Raton, FL, CRC Press, 2020).

70. D. Vermilyea, J. Electrochem. Soc., 116, 1179 (1969).

71. O. Fruhwirth, G. W. Herzog, I. Hollerer, and A. Rachetti, Surf. Technol., 24, 301 (1985).

72. J. H. Nordlien, S. Ono, N. Masuko, and K. Nisancioglu, Corros. Sci., 39 , 1397 (1997).

73. M. Taheri, R. C. Phillips, J. R. Kish, and G. A. Botton, Corros. Sci., 59, 222 (2012).

74. M. Taheri and J. R, Kish, J. Electrochem. Soc., 160, C36 (2013).

75. L. Hopkinson, P. Kristova, K. Rutt, and G. Cressey, Geochim. Cosmochim. Acta, 76, 1 (2012).

76. K. T. Tran, K. S. Han, S. J. Kim, M. J. Kim, and T. Tran, Hydrometallurgy, 160, 106 (2016).

77. Y. Zhang, Y. Hu, L. Wang, and W. Sun, Miner. Eng., 139, 105868 (2019).

78. M. Jönsson, D. Persson, and C. Leygraf, Corros. Sci., 50, 1406 (2008).

79. Z. Cui, X. Li, K. Xiao, and C. Dong, Corros. Sci., 76, 243 (2013).

80. J. Liao and M. Hotta, Corros. Sci., 112, 276 (2016).

81. Q. Gautier, P Bénézeth, V. Mavromatis, and J. Schott, Geochim. Cosmochim. Acta, 138, 1 (2014).

82. J. A. Dirksen and T. A. Ring, Chem. Eng. Sci., 46, 2389 (1991).

83. S. Thomas, O. Gharbi, S.H. Salleh, P. Volovitch, K. Ogle, and N. Birbilis, Electrochim. Acta, 210, 271 (2016).

84. A. Guha, S. Narayanaru, and T. N. Narayanan, ACS Appl. Energy Mater., 1, 7116 (2018).

85. A. Guha, N. M. Kaley, J. Mondal, and T. N. Narayanan, J. Mater. Chem. A, 8, 15795 (2020).

86. J. A. Yuwono, N. Birbilis, C. D. Taylor, K. S. Williams, A. J. Samin, and N. V. Medhekar, Corros. Sci., 147, 53 (2019).

87. T. Würger, C. Feiler, G. B. Vonbun-Feldbauer, M. L. Zheludkevich, and R. H. Meißner, Sci. Rep., 10, 15006 (2020).

88. S. H. Salleh, S. Thomas, J. A. Yuwono, K. Venkatesan, and N. Birbilis, Electrochim. Acta, 161, 144 (2015).

89. K. S. Williams, J. P. Labukas, V. Rodriguez-Santiago, and J. W. Andzelm, Corrosion, 71, 209 (2015).

90. P. Gore, V. S Raja, and N. Birbilis, J. Electrochem. Soc., 165, C849 (2018).

91. H. B. Yao, Y. Li, and A. T. S. Wee, Appl. Surf. Sci., 158, 112 (2000).

92. J. R. Kish, Y. Hu, J. Li, W. Zheng, and J.R. McDermid, Corrosion, 68, 468 (2012).

4.9 Supporting information

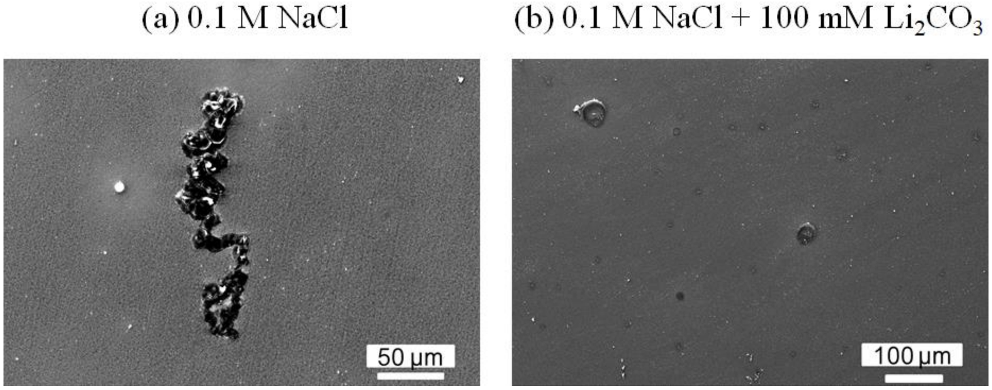

Figure 4.14. SEM image for ZEK100 in 0.1 M NaCl (aq) after 2.5 h immersion time, (a) 0 mM and (b) 100 mM (pH 11.1) Li_2CO_3 (aq).

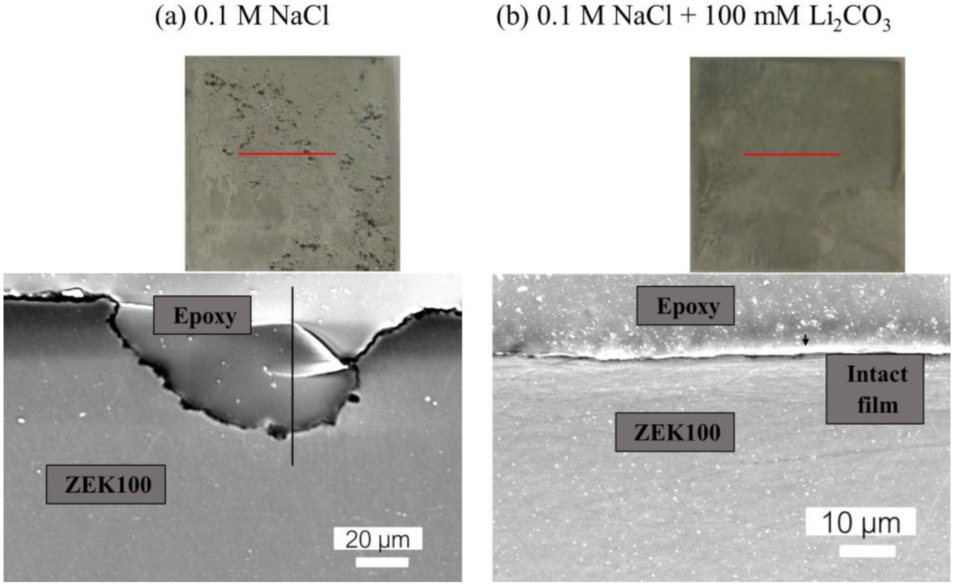

Figure 4.15. Photographic and cross-sectional SEM images For ZEK100 of hydrogen evolution and mass loss measurements for 4 days in 0.1 M NaCl (aq) (a) 0 mM and (b) 100 mM (pH 11.1) Li_2CO_3 (aq).

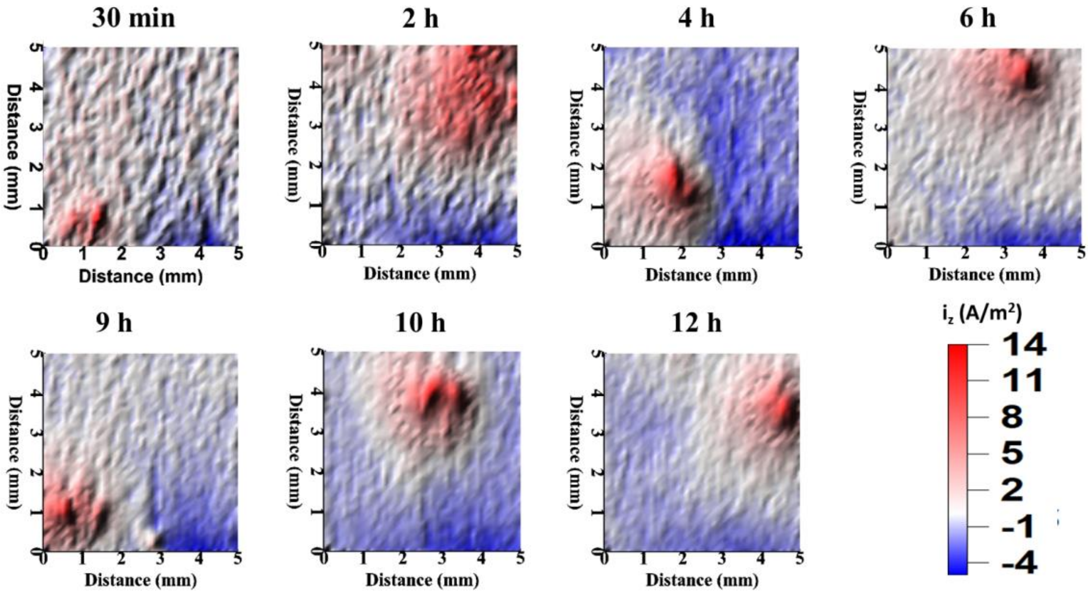

Figure 4.16. Time resolved SVET maps collected of ZEK100 during immersion in 0.1 M NaCl (aq) at ambient temperature after 12 h immersion.

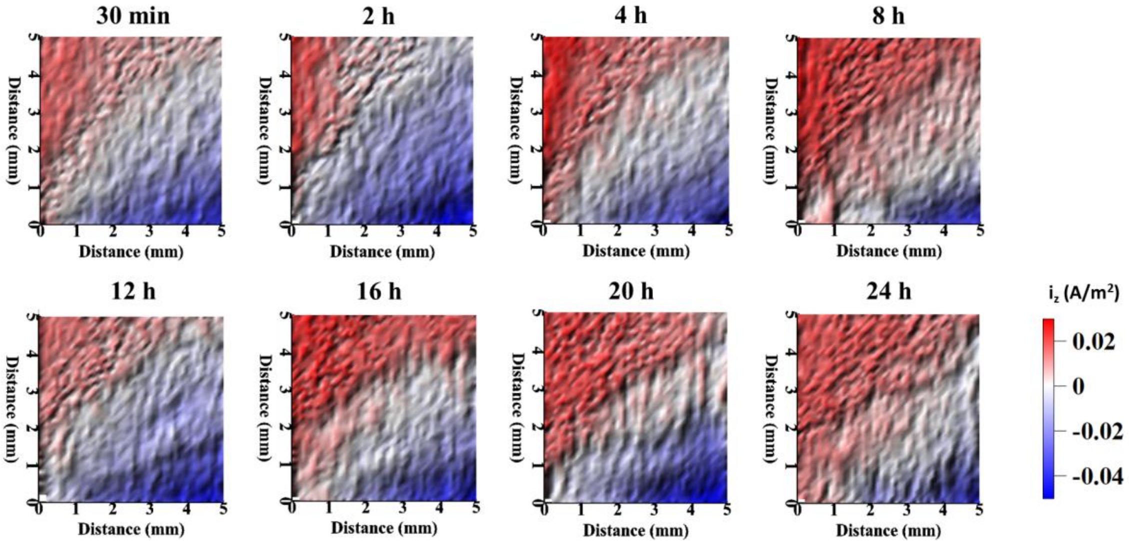

Figure 4.17. Time resolved SVET maps collected of ZEK100 during immersion in 0.1 M NaCl (aq) with dissolved 100 mM Li_2CO_3 (pH 11.1) at ambient temperature after 24 h immersion.

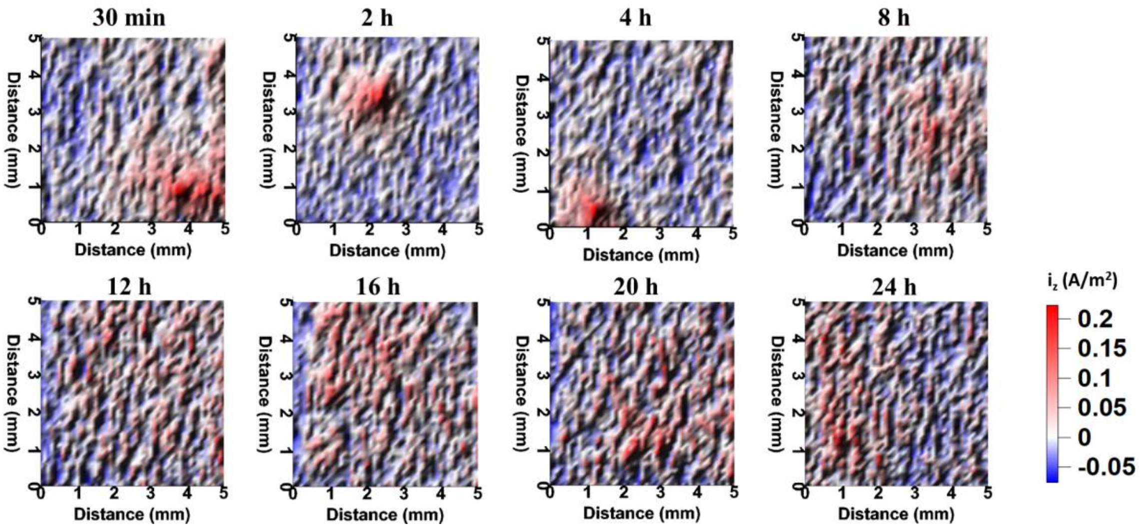

Figure 4.18. Time resolved SVET maps collected of ZEK100 during immersion in 0.1 M NaCl (aq) with dissolved 3 mM LiOH (pH 11.1) at ambient temperature after 24 h.

Chapter 5

Reducing Corrosion of Mg Alloy ZEK100 Sheet Metal with Lithium Carbonate Surface Pre-Treatment

B. Zaghloul and J.R. Kish*

Centre for Automotive Materials and Corrosion
McMaster University, Hamilton, ON Canada L8S 4L7

*Corresponding Author: (905) 525-9140, extension 21492, kishjr@mcmaster.ca

Submitted to Surface & Coatings Technology on 22nd June 2021

5.1 Abstract

The objective of this work was to determine the improved corrosion control imparted to Mg alloy ZEK100 sheet metal by a chemically (spray) deposited Li_2CO_3 surface pre-treatment. A commercial hexafluoro-titanate/zirconate-polymer conversion coating (Bonderite® MNT 5200) along with the bare metal surface served as the comparative basis. Coatings were characterization for structure and composition using X-ray diffraction and electron microscopy techniques. Corrosion in 0.1 M NaCl (aq) was assessed using conventional electrochemical polarization and electrochemical impedance spectroscopy measurements. The Li_2CO_3-coated surface exhibits the lowest relative corrosion, whereas the conversion-coated surface exhibits the highest relative corrosion. Improved corrosion control is attributed to the formation of a less defective (more compact) coating (physical contribution) and the ability of dissolved Li_2CO_3 to inhibit both the anode and cathode kinetics (electrochemical) contribution.

Keywords: magnesium, corrosion, coating, surface analysis

5.2 Introduction

Structural Mg alloys continue to garner interest within the transportation industry as candidate materials to improve fuel efficiency through lightweight design [1,2]. However, corrosion is a substantial technical challenge that is hindering widespread utilization [3-5]. Corrosion of Mg in aqueous chloride-containing solutions involves the conversion of Mg to $Mg(OH)_2$ according to the overall reaction: $Mg + 2H_2O \rightarrow Mg(OH)_2 + H_2$. Elementary steps include: (i) anodic dissolution of Mg to Mg^{2+}, (ii) cathodic reduction of H_2O to H_2, and (iii) precipitation of $Mg(OH)_2$ from a supersaturated alkaline solution at cathode sites. The tendency for the native oxide/hydroxide surface film to breakdown locally and for the solid oxide/hydroxide corrosion product, secondary intermetallic phases or the dissolving surface itself to serve as an active cathode (cathodic activation) has inspired various alloying, processing and surface modification strategies for improved corrosion control, which has been reviewed elsewhere [6-8]. A protective coating scheme comprised of a pre-treated surface layer and a polymer sealant overcoat is currently considered a minimum requirement for corrosion control of Mg alloys, particularly so for automotive applications [4,9,10].

A pre-treated surface layer provides both a degree of physical barrier protection against corrosion and a favorable surface for the polymer-based sealant overcoat to adhere to. A myriad of surface pre-treatments have been developed as part of protective coatings for Mg alloys, which, for example, include those reviewed for chemical/electrochemical deposition [9,11,12], anodizing [13], plasma electrolytic deposition [14] and sol-gel [15] processes. The ability to provide corrosion inhibition through surface film formation, when dissolved at local defects sites in the protective coating, is a desirable feature of inorganic pre-treatments [16-19]. Li_2CO_3 is a promising candidate in this context considering the beneficial effect of Li, as an alloying element, has on inhibiting the anodic kinetics of Mg [20] and of dissolved carbonate (CO_3^{2-}/HCO^{3-}/OH^-) on inhibiting both the anode and cathode kinetics of Mg [21-23]. Li_2CO_3 has been added as a leachable inhibitor additive in a protective coating applied to Al alloys for improved corrosion control [24-26]. Dissolved Li ions promote the fast formation of a protective multi-layered Al-Li-O surface film [26]. Corrosion inhibition of Mg alloy AZ31B-H24 (3% Al, 1% Zn, 0.5% Mn, balance Mg) [27] and ZEK100 (1.3% Zn, 0.2% Nd, 0.25% Zr, balance Mg) [28] in 0.1 M NaCl (aq) in the presence of dissolved Li_2CO_3 (aq) has been investigated with promising results. Inhibition involves the formation of by-layered Mg-Li-O-C surface film at dissolving anode site, which is argued to increase the concentration polarization contribution to anodic dissolution and suppress localized filament-like corrosion formation and associated cathodic activation.

The objective of this work was to demonstrate the improved corrosion control imparted to Mg alloy ZEK100 sheet metal by a chemically (spray) deposited Li_2CO_3 coating. The bare metal surface along with a surface coated with a commercial hexafluoro-titanate/zirconate-polymer conversion coating (Bonderite® MNT 5200) served as the baseline for comparison. This commercial conversion was included based on relevant prior work [29,30] and industry interest [10,12,31]. X-ray diffraction (XRD) was used to confirm Li_2CO_3 formation. The structure and composition of the as-coated surfaces were characterized using scanning electron microscopy (SEM) and transmission electron microscopy (TEM) of focused-ion beam (FIB) milled cross-sections. Short-term corrosion was assessed in 0.1 M NaCl (aq) at ambient temperature using electrochemical polarization and electrochemical impedance spectroscopy (EIS) measurements.

5.3 Materials and Methods

Commercial 1.5 mm thick ZEK100 sheet metal product in the fully annealed O temper was provided by Luxfer MEL Technologies (formerly Magnesium Elecktron) through Magna International. The chemical composition is 1.4% Zn + 0.2% Nd + 0.28% Zr + balance Mg, as was determined by inductively coupled plasma - optical emission spectroscopy (ICP-OES). The microstructure includes the single α-Mg matrix phase with a distribution of near-globular second phase ternary Mg-Zn-Nd and Zr-rich particles on the micro-scale [32-34].

The process used to spay-deposit a Li_2CO_3 coating on ZEK100 is schematically shown in Figure 5.1. As this was proof-of-concept type of study, small samples 2.5 cm × 2.5 cm were used for testing purposes. The working surface (RD (rolling direction) - TD (transverse direction) plane) was mechanically abraded to a 1200 grit surface finish using SiC abrasive papers and ethylene glycol as a lubricant. Subsequent cleaning of the working surface involved the usual steps specified for Mg: (i) ultrasonic degreasing, (ii) alkaline cleaning, and (iii) acid etching [9]. The working surface was degreased by immersing in an ultrasonic bath containing isopropyl alcohol at 55 ℃ for 10 minutes and then cleaned by immersing in an alkaline 1 M NaOH (aq) + 0.1 M Na_2CO_3 (aq) solution at 55 ℃ for 10 minutes. Thereafter, the working surface was pickled by dipped into a 0.1 M H_2SO_4 (aq) for approximately 1 second. A rinse with distilled water followed by drying in a stream of flowing air was performed after each of the aforementioned steps. Once cleaned, a small volume (100 mL) of 0.1 M Li_2CO_3 (aq) was spray-deposited on to the working surface, which was sufficient to cover the entire surface when flat, and then dried at 35 °C for 15-30 minutes. All solutions listed above were prepared using reagent grade chemicals and distilled water. X-ray diffraction (XRD) was used to confirm the Li_2CO_3 composition of the deposited coating. A. Bruker D8 Advanced X-ray diffractometer with a Cu-Kα radiation source was used for this purpose. A set of ZEK100 panels (10 cm × 15 cm) were sent to ACT Test Panels LLC (Hillsdale, LI) for application of the commercial hexafluoro-titanate/zirconate-polymer conversion coating. The process included degreasing, alkaline cleaning, acid activation, and coating. Small test samples 2.5 cm × 2.5 cm were prepared from the as-coated panels.

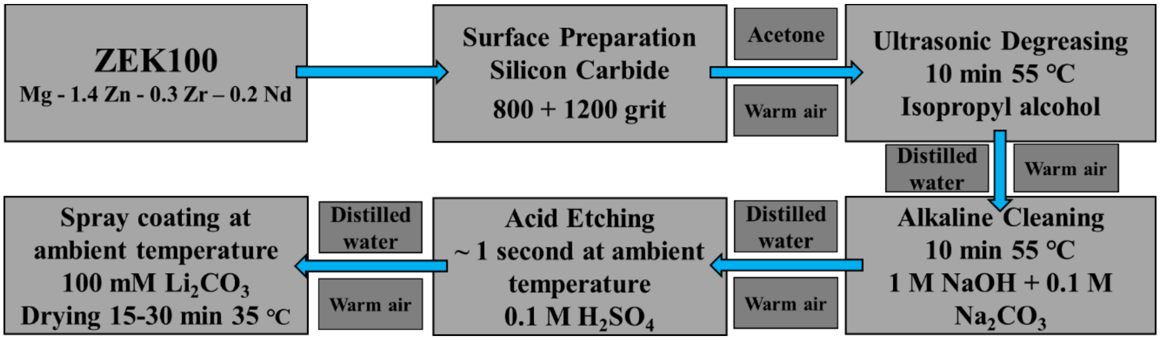

Figure 5.1. Schematic diagram for coating the ZEK100 surface with a spray-deposited Li_2CO_3 surface pre-treatment coating.

The structure and composition of both coatings (Li_2CO_3 and hexafluoro-titanate/ zirconate-polymer) was determined electron microscopy techniques. SEM was used for plan-view imaging (structure), whereas TEM and associated scanning mode techniques (X-ray energy dispersive spectroscopy (EDS) and electron energy loss spectroscopy (EELS)) was used for cross-sectional imaging (structure) and composition (element) characterization. A Zeiss NVision40 FIB-SEM with a used for the SEM examination and a Thermo Scientific Talos 200X equipped with a Gatan ContinuumS GIF EELS spectrometer and a Super-X EDS system was used for the TEM examination. Plan view secondary electron images of the coated surfaces were acquired using an accelerating voltage of 5 kV and a working distance of 5.2 mm (Li_2CO_3-coated surface) and 5.1 mm (conversion-coated surface). Electron transparent cross-sectional foils of the coated surfaces were prepared by the FIB milling and in-situ lift-out method using the Zeiss NVision40 FIB-SEM. Regions of interest were protected against the so-called curtaining effect by depositing a W layer on the site. Cross-sectional foils were examined 95 K (cryogenically mode) to minimize possible electron beam damage. The TEM examination was conducted using an accelerating voltage of 200 kV. The EELS data was processed using Gatan Digital Micrograph 3.4 and the EDS data was processed using FEI Velox 3.1.

All electrochemical measurements were made using a conventional three electrode cell and a computer-controlled potentiostat (Gamry Reference 600™). The electrolyte was naturally aerated 0.1 M NaCl (aq) held at ambient temperature, which was made fresh for each measurement using reagent grade NaCl (s) and distilled water. A graphite rod was used as the counter electrode and a saturated calomel electrode was used as the reference electrode. Working electrodes were bare ZEK100, Li_2CO_3-coated

ZEK100 or conversion-coated ZEK100. The bare surface was mechanically abraded to a 1200 grit surface finish using SiC abrasive papers and ethylene glycol as a lubricant prior to measurement. Potentiodynamic polarization measurements were made using a scan rate of 1 mV/s and were initiated after a 10 minute condition of the working electrode at the open-circuit potential (OCP). Polarization was started at a potential 250 mV more negative than the OCP recorded after 10 minutes and stopped at a potential 250 mV more positive than the OCP recorded after 10 minutes. EIS measurements were made over a frequency range from 0.01 Hz to 100 kHz using an AC voltage signal of ±10 mV. Measurements were made after the working electrodes were condition at the OCP for 10 minutes. The short time was necessary to minimize dissolution of the coatings applied. A set of at least three replicate measurements were carried out using to provide a measure of reproducibility.

5.4 Results

Figure 5.2a and 5.2b show photographic images of as-polished and Li_2CO_3-coated ZEK100 surface. The coating is compact, uniform and adherent when viewed with the unaided eye. The corresponding XRD spectrum acquired from the Li_2CO_3-cotaed surface is shown in Figure 5.2c. Also included for comparatives purposes are the spectra acquired from: (i) reagent grade Li_2CO_3 powder, (ii) JCPDF Li_2CO_3 powder reference and (iii) mechanically-abraded bare ZEK100 surface. The peaks acquired from the Li_2CO_3-coated surface exactly match those acquired from the reagent grade powder and the JCPDS Li_2CO_3 powder reference. Therefore, the spray deposition method was successful in depositing a crystalline Li_2CO_3 coating on the surface of ZEK100. As for the bare

ZEK100 surface, all major 2θ peaks observed (~32° $(10\bar{1}0)$, ~35° (0002), ~37° $(10\bar{1}1)$, ~48° $(10\bar{1}2)$, ~58° $(2\bar{1}\bar{1}0)$ and 64° $(10\bar{1}3)$,) correspond to hexagonal close packed Mg metal [35].

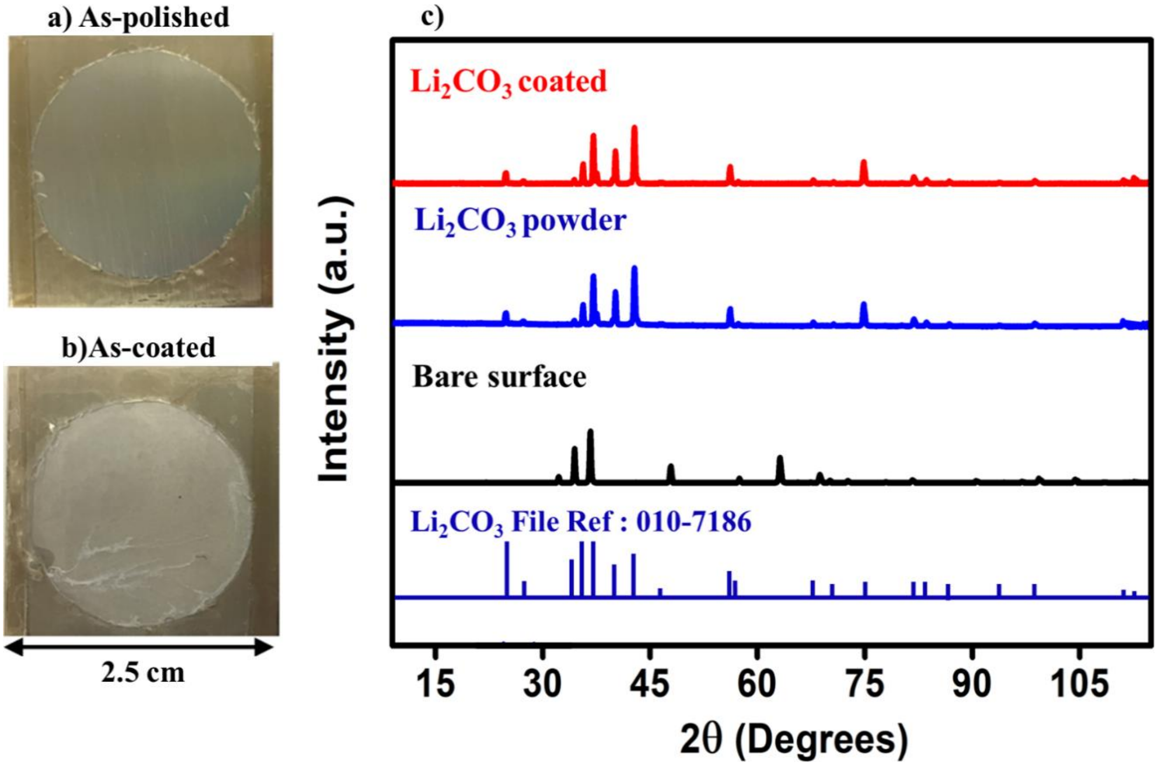

Figure 5.2. (a) and (b) Photographic images of as-polished ZEK100 and as-prepared Li_2CO_3-coated surface. (c) XRD spectra acquired from the Li_2CO_3- coated surface, bare surface and the reagent grade Li_2CO_3 powder. Also included is the JCPDS Li_2CO_3 powder reference for comparison.

Figure 5.3a and 5.3b show secondary electron images of the Li_2CO_3-coated surface. The coating is compact, uniform and adherent when viewed at these magnifications. The morphology consists of plate-like crystals that have grown in random directions. No major defects such as cracks and pores are observed at these magnifications. Secondary electron images of the conversion-coated surface are shown in

Figure 5.3c and 5.3d. The dark rectangular feature in the center region of Figure 5.3d is the protective W layer applied prior to FIB milling. The conversion coating also is compact, uniform and adherent when viewed at similar magnifications. However, the micro-crack indications are observed on the surface. Similar features have been reported elsewhere for this conversion coating when imaged using SEM [36].

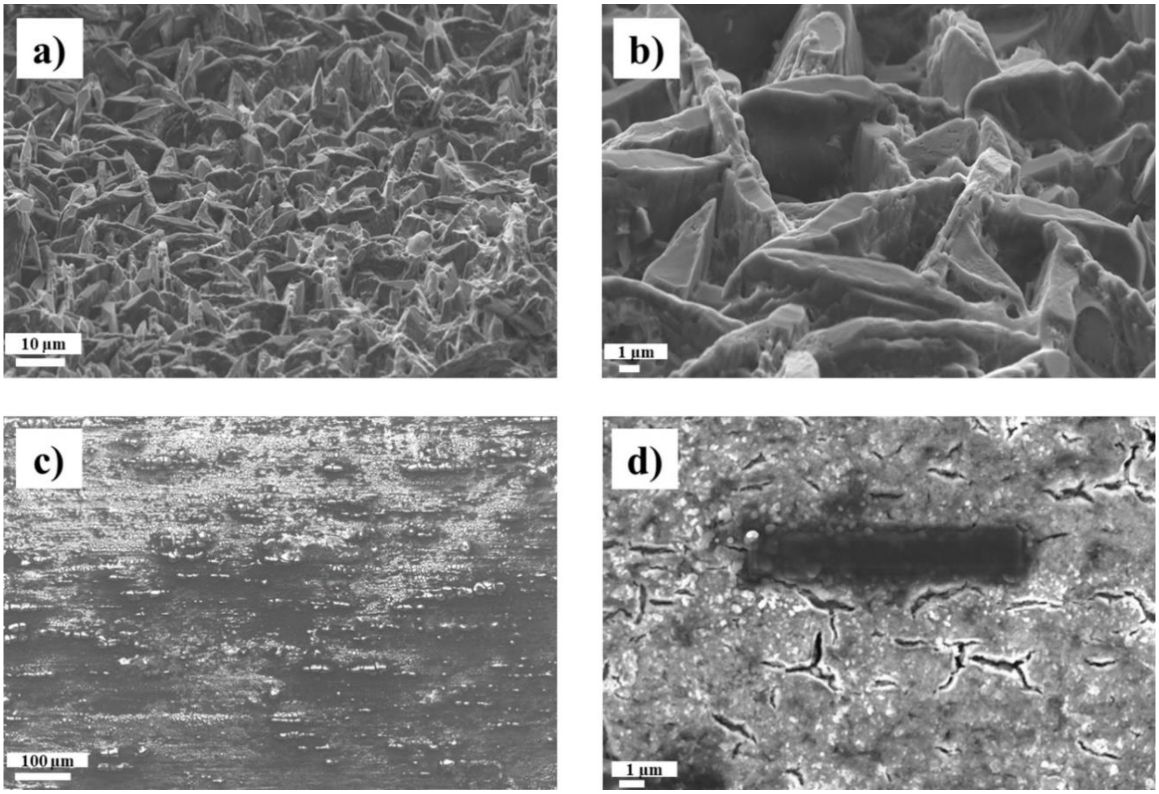

Figure 5.3. Plan view secondary electron images of the Li_2CO_3-coated surface (a and b) and the conversion-coated surface (c and d).

A high-angle annular dark-field (HAADF) image of the FIB-prepared Li_2CO_3-coated surface cross-section is shown in Figure 5.4 along with an associated STEM-EELS maps for Mg, Zn and Nd (metal) and C, Li and O (coating). The image shows the coating is compact and adherent to the metal substrate. The thickness ranges from 1.7 μm to 3.3 μm across the width of this cross-sectional sample. Defects including cracks and voids are not observed in the cross-section. Major surface layer forming elements include Li, C and O, as expected. None of the alloying elements are detected in the layer. However, there is a thin layer Mg-O-containing layer that separates the Li_2CO_3 coating from the metal. A relatively large Nd-containing particle resides at the metal surface. This particle does not impact the adhesion of the Li_2CO_3 coating in any meaningful way as it too is covered by the Mg-O containing intermediate layer.

Figure 5.5 shows a high-angle annular dark-field (HAADF) image of the FIB-prepared conversion-coated surface cross-section along with an associated STEM-EDS maps for Mg and Zn (metal) and F, O, C, Ti and Zr (coating). The conversion coating is significantly thinner than the Li_2CO_3 coating, but it is significantly more defective. The thickness ranges from 180 nm to 200 nm across the width of this cross-sectional sample. A relatively large pore exists within the coating itself and a second, smaller one, exist at the surface. Based on the STEM-EDS maps, the conversion coating consists of a dense layer containing F, N, O and Ti to a greater extent and Mg, Zr and Zn to a lesser extent. Zn is enriched at the metal/coating interface. Similar features have been reported elsewhere for this conversion coating when imaged using STEM-EDS [36].

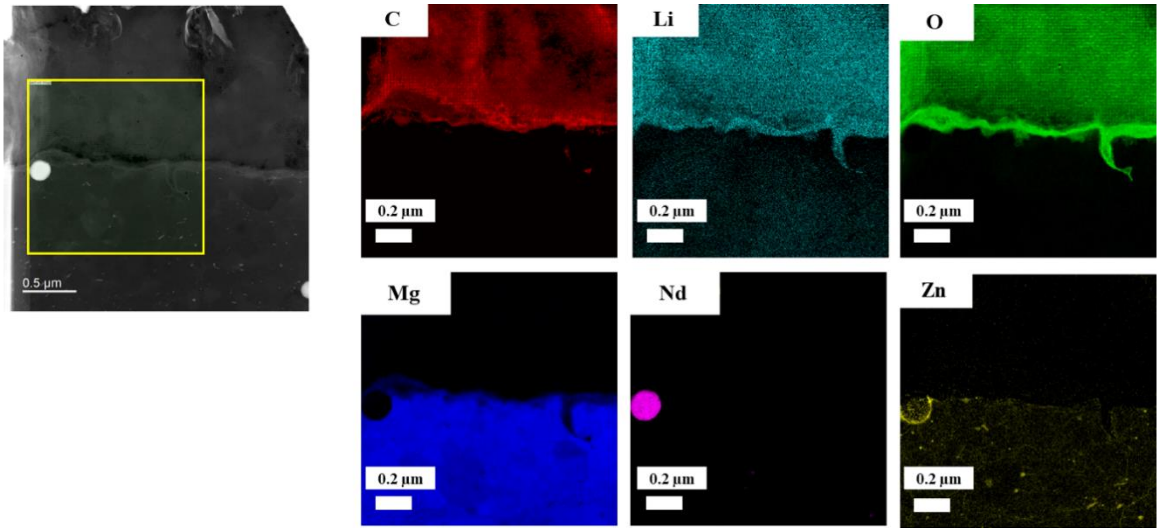

Figure 5.4. Cross-section HAADF image of the Li_2CO_3-coated surface and associated STEM-EELS elemental maps of the coating/metal interface.

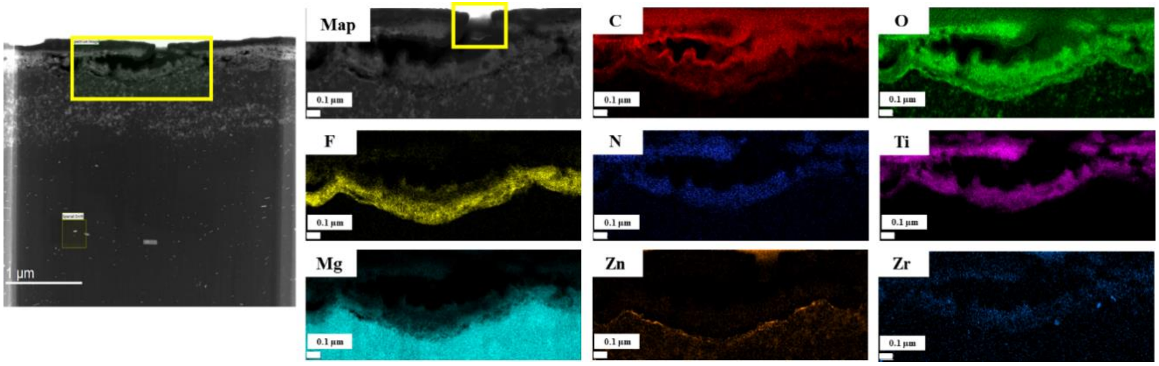

Figure 5.5. Cross-section HAADF image of the conversion-coated surface and associated STEM-EDS elemental maps of the coating/metal interface.

Figure 5.6a compares the OCP transients for 10 minute condition prior to initiating the potentiodynamic polarization measurements on the bare, Li_2CO_3-coated and conversion-coated ZEK100 surfaces immersed in 0.1 M NaCl (aq). The bare surface exhibits the expected transient: one consisting of an initial relatively rapid increase to a local maximum, which coincides with the localized breakdown of the native surface film [37,38], followed by a relatively slower decrease to a local minimum and then a relatively slow increase towards a steady-state value. The Li_2CO_3-coated surface exhibited a simple transient, one consisting of an initial decrease to a local minimum, followed by a small and gradual increase towards a steady-state value. The conversion-coated surface exhibited an even simpler transient: one consisting of a slow decayed towards a steady-state value. The OCP transient for the conversion-coated surface is the most noble of the three, whereas the transient for the Li_2CO_3-coated surface was the least noble.

The potentiodynamic polarization responses of the three surfaces immersed in 0.1 M NaCl (aq) are shown in Figure 5.6b. The Li_2CO_3 coating inhibits both the global anode and cathode kinetics relative to the bare surface. The global anode kinetic is inhibited to a greater extent than the global cathode kinetics. Note the polarization response for the conversion-coated surface consists of a separate measurement for the anode and cathode kinetics, with polarization starting from the OCP recorded after 10 minutes immersion. This was necessary to acquire reproducible responses. The conversion coating does not inhibit the global anode kinetics to any extent relative to the bare surface, but significantly increases the cathode kinetics relative to the bare surface.

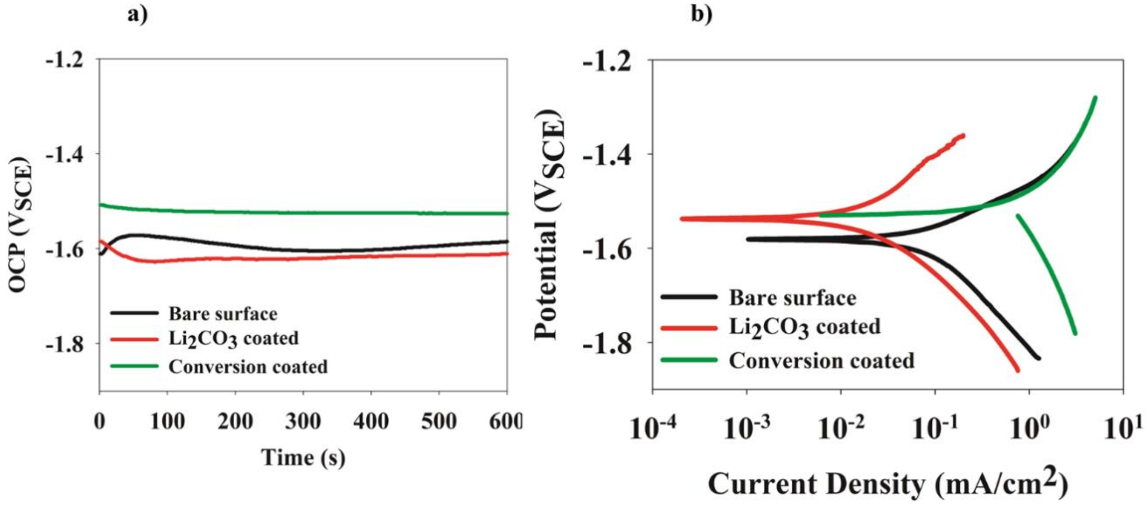

Figure 5.6. a) OCP transients and b) potentiodynamic polarization responses for the Li_2CO_3-coated, conversion-coated and bare surfaces immersed in 0.1 M NaCl (aq) at ambient temperature.

Figure 5.7a and 5.7b show Nyquist plots comparing the EIS responses recorded for the surfaces immersed in 0.1 M NaCl (aq). The conversion-coated surface is plotted separately because of the low impedance values recorded relative to the bare and Li_2CO_3-coated surfaces. The bare and the Li_2CO_3-coated surface show similar features (Figure 5.7a): a large capacitance loop at high frequencies and a small capacitance at low frequencies. Both spectra show the beginnings of an apparent inductive loop at the lowest frequencies considered. However, inspection of the Bode plots does not provide evidence that supports an inductive response with either corroding surface. The latter requires a positive phase angle at low frequencies and an impedance modulus that decreases with decreasing frequency: neither of which is observed for in the Bode plot comparing these two surfaces (Figure 5.7e). In contrast, the conversion-coated surface shows a single capacitance loop and a single inductance loop (Figure 5.7b), the latter being reflective by both a positive phase angle at low frequencies and an impedance modulus that decreases with decreasing frequency in the Bode plot (Fig. 5.7e). Qualitatively speaking, the EIS data shows that the order of the increasing corrosion control is conversion-coated surface < bare surface < Li_2CO_3-coated surface.

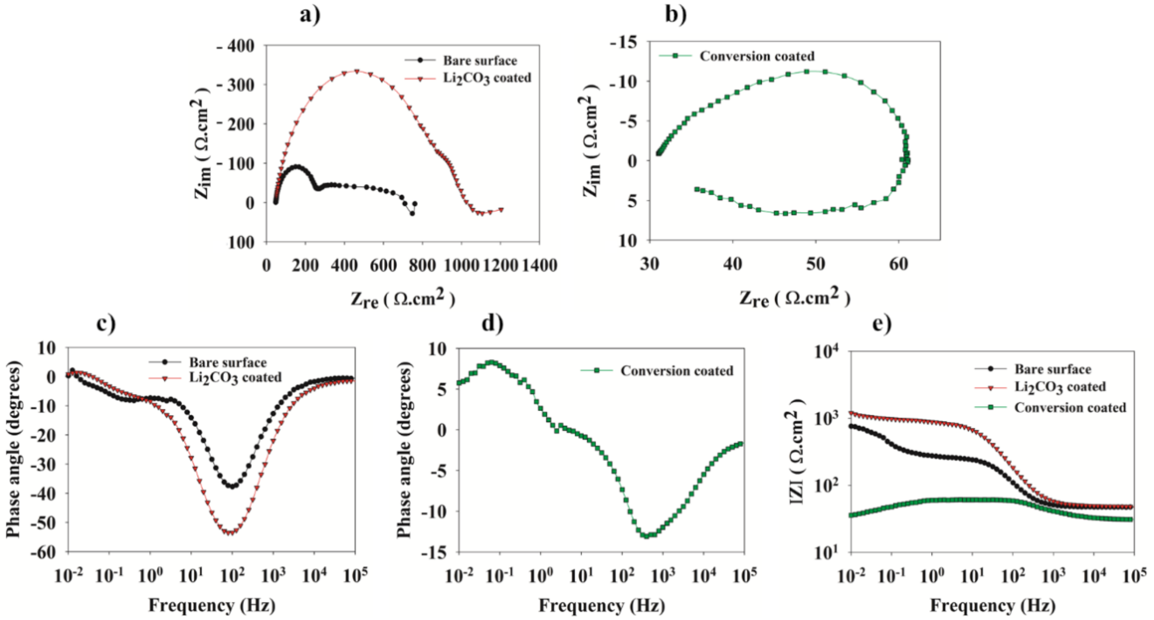

Figure 5.7. EIS spectra for the Li_2CO_3-coated, conversion-coated and bare surfaces immersed in 0.1 M NaCl (aq): Nyquist plots (a and b), phase angle plots (c and d) and Bode plot (d).

5.5 Discussion

The results presented certainly demonstrate that a Li_2CO_3 coating reduces corrosion of ZEK100 immersed in 0.1 M NaCl (aq) relative to the bare surface. Consider the starting physical features of the Li_2CO_3 coating revealed by the TEM examination in Figure 5.4 (dense, uniform and lacking pores and cracks), improved corrosion control likely involves a physical barrier contribution [9,11]. However, the aqueous chemistry of Li_2CO_3 also provides an electrochemical inhibition contribution [27,28]. Li_2CO_3 dissolves in water in the following manner (equilibrium solubility product (k_{sp}) and base (k_b) constants quoted for 298 K [39]):

$$Li_2CO_3(s) \rightarrow 2Li^+(aq) + CO_3^{-2}(aq) \quad k_{sp} = 8.15 \times 10^{-4} \tag{1}$$

$$CO_3^{2-}(aq) + H_2O \rightarrow HCO_3^-(aq) + OH^-(aq) \quad k_b = 2 \times 10^{-4} \tag{2}$$

It is this chemical reactivity that forced the electrochemical measurements to be made after relatively short immersion time. Longer times would certainly lead the completely dissolution of the Li_2CO_3 coating given the volume to surface ratio used in this work. It is also this chemical reactivity that Li_2CO_3 has been selected as a candidate inorganic compound corrosion inhibitor for Mg alloys. As the potentiodynamic polarization measurements show, both the anode and cathode kinetics are inhibited, which the anode kinetics being inhibited to a greater extent. Inhibition of the anode kinetics is believed to involve the formation of a thin, compact and uniform Li-doped MgO film on the dissolving metal surface, which serves increase the concentration polarization contribution (slower Mg^{2+} transfer from the dissolving surface to the solution) to the global kinetics [28]. Inhibition of the cathode kinetics (H_2 evolution) is believed to involve a modified H bond energy in the presence of Li^+ (aq) at the cathode site [28]. Dissolved Li^+ (aq) has been shown to alter the H_2 evolution kinetics on metal electrodes immersed in aqueous electrolytes, either increasing or decreasing depending on the metal, by modifying the H bond energy [40,41]. Another key aspect of corrosion inhibition involves the suppression of the localized filament-like corrosion and associated cathodic activation that the bare surface would exhibit otherwise when immersed in NaCl (aq) [28,38,42].

The conversion-coated surface does not inhibit the global anodic dissolution kinetics of ZEK100 to any extent, relative to the bare surface (Figure 5.6b). This is not surprising given the starting physical features of the coating revealed by the TEM examination (thin and compact, but defective with relative large pores). Although the cross-section did not reveal a continuous path from the coating surface to the metal interface, the surface and internal pore observed suggests that continuous networks, existing elsewhere on the surface, can be expected. The non-protecting capability of this particular conversion coating also been observed when applied to Mg alloy AZ31B immersed in NaCl (aq) [43]. The non-protecting capability was also linked to the same physical features (a thin and compact, albeit porous coating). It is noted that this coating is not intended to be a standalone coating to protect Mg alloys against corrosion. It has the interest of the automotive industry since it is a favorable surface on which an epoxy over-coat can be applied by cathodic electrophoretic deposition (E-coat) as part of a protective coating scheme applied to Mg alloys [43,44,45]. A chemical contribution to corrosion control is not expected either. A possible leachable component of the conversion layer to contribute to corrosion control would be F^- (aq) anions, through subsequent film formation by MgF_2 ($k_{sp} = 5.16 \times 10^{-11}$ at 25 °C [39]). However, no significant level of corrosion inhibition of Mg [16] or AZ31B [17] is observed in NaCl (aq) with relative small additions (10 mM) F^- (aq).

Although the physical features of the respective coating can alone explain the observed effect on the global anode dissolution kinetics relative to the bare surface, they do not seem wholly explain the EIS measurements (Figure 5.7). An inductive response was only observed by the conversion-coated surface (Figure 5.7b). A similar inductive loop was observed in the EIS measurements published for conversion-coated AZ31B immersed in NaCl (aq) [43]. The inductive loop associated with Mg corrosion has been given some recent consideration [46-49]. Coupling EIS measurements with online inductively coupled plasma - atomic emission spectroscopy elegantly showed that the inductance is associated with increased (cathodically-activated) anodic dissolution to Mg^{2+} (aq) [48]. The 10 minute conditioning of the bare surface at the OCP in 0.1 M NaCl (aq) (prior to the EIS measurement, Figure 5.6a) was not long enough to permit the initiation of the filament-like corrosion mode and the concomitant activated anodic dissolution coupled with enhanced H_2 evolution [28,38]. Therefore, there would be no inductive contribution to the impedance measured. For the conversion-coated surface to provide an inductive contribution, then the coating itself in some way needs to activate Mg dissolution at a coating-metal-solution interface. One such possibility involves the formation of a galvanic cell between some local active cathode that couple with the bare metal anode, thus activating anodic dissolution in a manner akin to DC polarization-induced activation [50]. The enhanced cathode kinetics observed on the conversion-coated surface supports this hypothesis. A possible local cathode could be the Zn-enriched layer at the metal/coating interface. The formation of a thin, presumably metallic, Zn-enriched layer at the metal/oxide-hydroxide during anodic dissolution of Zn-containing Mg alloys is typically revealed by cross-sectional TEM examination of the metal/film interface [28,36,51,52]. Since Zn is more noble than Mg, it would serve as a cathode in a galvanic couple with Mg. Enrichment either involves incongruent dissolution of the Zn-containing Mg alloy or re-deposition of dissolved Zn^{2+} (aq) and metallic Zn as an additional local cathode reaction. The latter is one of the theories proposed to explain cathodic activation, which involves de-coupled dissolution and re-deposition of noble metal impurities [53,54]. Regardless, the Zn-enrichment likely is a consequence of corrosion that occurred during the conversion coating process. The incorporation of Mg into the conversion coating is direct evidence (Figure 5.5) that this is indeed the case. Therefore, the condition necessary for galvanic corrosion to be established immediately upon immersion exist for the conversion coating, providing there are interconnecting pores that put the solution in direct contact with the bare metal. More research is clearly required to test this hypothesis.

5.6 Conclusions

1. Li_2CO_3 was successfully spray-deposited onto Mg Alloy ZEK100 sheet metal as a candidate surface pre-treatment layer. The as-deposited coating is dense, uniform and lacks defects such as pores and cracks. In contrast, the commercial hexafluoro-titanate/zirconate-polymer conversion coating is compact and thin, but contains relatively large defects such as pores and cracks.
2. Electrochemical measurements demonstrate that the Li_2CO_3-coated surface reduces corrosion of ZEK100 immersed in 0.1 M NaCl (aq) relative to the bare surface. The improved corrosion control likely involves both a physical

(barrier) and electrochemical (corrosion inhibiting) contribution as both the global anode and cathode kinetics are reduced relative to the bare metal.

3. The conversion-coated surface shows an inductive contribution to the impedance measured during short term immersion, which implies activated dissolution is occurring. STEM-EDS mapping points to a local galvanic coupling between the Zn-enriched layer (cathode) and the bare metal surface (anode) at sites where the solution would be in direct contact with the bare metal.

5.7 Acknowledgments

Funding for operating costs was provided by Natural Science and Engineering Research Council (NSERC) under the Discovery Grants program (RGPIN-2020-05727). Funding in the form of a student stipend and living allowance (B. Zaghloul) was provided by the Egyptian Armament Authority (EAA). The Canadian Centre for Electron Microscopy (CCEM) is a national facility supported by NSERC, Canada Foundation for Innovation (CFI), under the MSI program, and McMaster University.

5.8 Data Availability

The raw/processed data required to reproduce these findings can be shared upon request.

5.9 References

1. W.J. Joost, P.E. Krajewski, Towards magnesium alloys for high-volume automotive applications, Scr. Mater. 128 (2017) 107-112. https://doi.org/10.1016/j.scriptamat.2016.07.035.

2. X. Zhang, Y. Chen, J. Hu, Recent advances in the development of aerospace materials, Prog. Aerosp. Sci., 97 (2018) 22-34. https://doi.org/10.1016/j.paerosci.2018.01.001.

3. R.C. McCune, J. Forsmark, B. Schneider, A. Luo, H. Gu, W. Schumacher, X. Chen, F. Vartolas, Development of corrosion testing protocols for magnesium alloys andmagnesium-intensive subassemblies, SAE Int. J. Mater. Manf. 6 (2013) 242-47. https://doi.org/10.4271/2013-01-0978.

4. M.P. Brady, W.J. Joost, C.D. Warren, Insights from a recent meeting: current status and future directions in magnesium corrosion research, Corrosion 73 (2016) 452-462. https://doi.org/10.5006/2255.

5. M. Liu, Y. Guo, J. Wang, M. Yergin, Corrosion avoidance in lightweight materials for automotive applications, NPJ Mater. Degrad. 2 (2018) 24. https://doi.org/10.1038/s41529-018-0045-2.

6 . X.B. Chen, H.Y. Yang, T.B. Abbott, M.A. Easton, N. Birbilis, Magnesium: engineering the surface, JOM 64 (2012) 650-656. https://doi.org/10.1007/s11837-012-0331-3.

7. K. Gusieva, C.H.J. Davies, J.R. Scully, N. Birbilis, Corrosion of magnesium alloys: the role of alloying, Int. Mater. Rev. 60 (2015) 169-194. https:/doi.org/10.1179/1743280414Y.0000000046

8. M. Esmaily, J.E. Svensson, S. Fajardo, N. Birbilis, G.S. Frankel, S. Virtanen, R. Arrabal, S. Thomas, L.G. Johansson, Fundamentals and advances in magnesium alloy corrosion, Prog. Mater. Sci. 89 (2017) 92-193. https://doi.org/10.1016/j.pmatsci.2017.04.011.

9. J.E. Gray, B. Luan, Protective coatings on magnesium and its alloys - a critical review, J. Alloys Compd., 336 (2002) 88-113. https://doi.org/10.1016/S0925-8388(01)01899-0.

10. J. Wang, X. Pang, H. Jahed, Surface protection of Mg alloys in automotive applications: a review, AIMS Mater. Sci. 6 (2019) 567-600. https://doi.org/10.3934/matersci.2019.4.567.

11. X.B. Chen, N. Birbilis, T.B. Abbott, Review of corrosion-resistant conversion coatings for magnesium and its alloys, Corrosion, 67 (2011) 035005. https://doi.org/10.5006/1.3563639.

12. I. Milošev, G.S. Frankel, Review - conversion coatings based on zirconium and/or titanium, J. Electrochem. Soc. 165 (2018) C127-C144. https://doi.org/10.1149/2.0371803jes.

13. C. Blawert, W. Dietzel, E. Ghali, G. Song, Anodizing treatments for magnesium alloys and their effect on corrosion resistance in various environments, Adv. Eng. Mater. 8 (2006) 511-533. https://doi.org/10.1002/adem.200500257.

14. J. Dou, Y. Chen, H. Yu, C. Chen, Research status of magnesium alloys by micro-arc oxidation: a review, Surface Engineering 33 (2017) 731-738. https://doi.org/10.1080/02670844.2017.1278642.

15. M. Talha, Y. Ma, M. Xu, Q. Wang, Y. Lin, X. Kong, Recent advancements in corrosion protection of magnesium alloys by silane-based sol–gel coatings, Ind. Eng. Chem. Res. 59 (2020) 19840-19857. https://doi.org/10.1021/acs.iecr.0c03368.

16. G. Williams, H. N. McMurray and R. Grace, Inhibition of magnesium localised corrosion in chloride containing electrolyte, Electrochim. Acta 55 (2010) 7824-7833. https://doi.org/10.1016/j.electacta.2010.03.023.

17. G. Williams, R. Grace, R.M. Woods, Inhibition of the localized corrosion of Mg alloy AZ31 in chloride containing electrolyte, Corrosion 71 (2015) 184-198. https://doi.org/10.5006/1376.

18. Z. Feng, B. Hurley, J. Li, R. Buchheit, J. Electrochem. Soc. 165 (2018): p. 94.

19. Z. Feng, B. Hurley, R. Buchheit, M. Zhu, Z. Yang, J. Hwang, J. Electrochem. Soc. 166 (2019): p. 520.

20. W. Xu, N. Birbilis, G. Sha, Y. Wang, J. E. Daniels, Y. Xiao and M. Ferry, A high-specific-strength and corrosion-resistant magnesium alloy, Nature Mater. 14 (2015) 1229-1235. https://doi.org/10.1038/nmat4435.

21. E. Gulbrandsen, Anodic behaviour of Mg in HCO_3^-/CO_3^{2-} buffer solutions. Quasi-steady measurements, Electrochim. Acta 37 (1992) 1403-1412. https://doi.org/10.1016/0013-4686(92)87014-Q.

22. B.R, Fazal, S. Moon, Electrochemical properties of air-formed oxide film-covered AZ31 Mg alloy in aqueous solutions containing various anions, J. Korean Inst. Surf. Eng. 50 (2017) 147-154. https://doi.org/10.5695/JKISE.2017.50.3.147.

23. L. Prince, M. A. Rousseau, X. Noirfalise, L. Dangreau, L. B. Coelho and M-G. Olivier, Inhibitive effect of sodium carbonate on corrosion of AZ31 magnesium alloy in NaCl solution, Corros. Sci. 179 (2021) 109131. https://doi.org/10.1016/j.corsci.2020.109131.

24. P. Visser, H. Terryn, J.M. Mol, Active corrosion protection of various aluminium alloys by lithium-leaching coatings, Surf. Interface Anal. 51 (2019) 1276-1287. https://doi.org/10.1002/sia.6638.

25. P. Visser, Y. Gonzalez-Garcia, J. M. Mol and H. Terryn, J. Electrochem. Soc. 165 (2018) C60-C70. https://doi.org/10.1149/2.1011802jes.

26. A. Kosari, P. Visser, F. Tichelaar, S. Eswara, J. N. Audinot, T. Wirtz, H. Zandbergen, H. Terryn and J. M. C. Mol, Appl. Surf. Sci. 512 (2020) 145665. https://doi.org/10.1016/j.apsusc.2020.145665

27. B. Zaghloul, C.F. Glover, J.R. Scully J.R. Kish, Inhibiting corrosion of Mg alloy AZ31B-H24 sheet metal with lithium carbonate, Corrosion 77 (2021) 192-203.

https://doi.org/10.5006/3625.

28. B. Zaghloul, J.R. Kish, Corrosion inhibition of Mg alloy ZEK100 sheet metal by dissolved lithium carbonate, J. Electrochem. Soc., (2021).

29. Z. P. Cano, J. R. Kish, J. R. McDermid, in Materials Science and Technology (MS&T) 2013 Conference Proceedings, Warrendale, PA 15086–7514 USA,1591 (2013).

30. J. R. Kish, Z. Cano, A. Kobylecky, J. McDermid, T. Skszek, Comparative corrosion assessment of coated alloys for multi-material lightweight vehicle architectures," Technical Paper 2015-01-0738, Society of Automotive Engineers International, Warrendale, PA, USA, 2015, http://dx.doi.org/10.4271/2015-01-0738.

31. G.S. Cole, Magnesium (Mg) corrosion protection techniques in the automotive industry, in: G-L. Song (Ed.), Corrosion Prevention of Magnesium Alloys, Philadelphia, PA Woodhead Publishing, 2013, pp. 489-508.

32. R. M. Asmussen, W. J. Binns, P. Jakupi, D. Shoesmith, The influence of microstructure on the corrosion of magnesium alloy ZEK100, Corrosion 71 (2014) 242–254. https://doi.org/10.5006/138771, 242.

33. A. Javaid, F. Czerwinski, Effect of hot rolling on microstructure and properties of the ZEK100 alloy, J. Magnes. Alloy 7 (2019) 27-37. https://doi.org/10.1016/j.jma.2019.02.001.

34. A. Javaid, A. Hadadzadeh, F. Czerwinski, Solidification behavior of dilute Mg-Zn-Nd alloys, J. Alloy Compd., 782 (2019) 132-148. https://doi.org/10.1016/j.jallcom.2018.12.134.

35. A. Jain, S.P. Ong, G. Hautier, W. Chen, W.D. Richards, S. Dacek, S. Cholia, D. Gunter, D. Skinner, G. Ceder, K.A. Persson, The Materials Project: A materials genome approach to accelerating materials innovation, APL Materials, 1 (2013) 011002. doi:10.1063/1.4812323.

36. M. P. Brady, D.N. Leonard, H.M.Meyer III, J.K. Thomson, K.A. Unocic, H.H.

Elsentriecy, G.-L. Song, K. Kitchen, B. Davis, Advanced characterization study of commercial conversion and electrocoating structures on magnesium alloys AZ31B and ZE10A, Surf. Coatings Technol. 294 (2016) 164-176. https://doi.org/10.1016/j.surfcoat.2016.03.066.

37. G. Williams, H. Ap Llwyd Dafydd, R. Subramanian, H.N. McMurray, The influence of chloride ion concentration on passivity breakdown in magnesium, Corrosion 73 (2017) 471-481. https://doi.org/10.5006/2328

38. C. Kousis, N. McMurray, P. Keil, G. Williams, The influence of chloride ion concentration on the localized corrosion of E717 magnesium alloy, Corrosion 77 (2021) 156-167. https://doi.org/10.5006/3601.

39. CRC Handbook for Chemistry and Physics, 101st Edition, J. Rumble, editor (Boca Raton, FL, CRC Press, 2020).

40. A. Guha, S. Narayanaru, T.N. Narayanan, Tuning the hydrogen evolution reaction on metals by lithium salt, ACS Appl. Energy Mater. 1 (2018) 7116-7122. https://doi.org/10.1021/acsaem.8b01546.

41. A. Guha, N. M. Kaley, J. Mondal, T.N. Narayanan, Engineering the hydrogen evolution reaction of transition metals: effect of Li ions, J. Mater. Chem. A 8 (2020) 15795-15808. https://doi.org/c9ta12926j.

42. R.M. Asmussen, W.J. Binns, P. Jakupi, D. Shoesmith, The influence of microstructure on the corrosion of magnesium alloy ZEK100, Corrosion 71 (2015) 242-254. https://doi.org/10.5006/1387.

43. S. Song, W.D. Shen, M.H. Liu, G.L. Song, Corrosion study of new surface treatment/coating for AZ31B magnesium alloy, Surf. Eng. 28 (2012) 486-490. https://doi.org/10.1179/1743294411Y.0000000056.

44. G.C. Wang, K. Stewart, R. Berkmortel, J.I. Skar, Corrosion prevention for external magnesium automotive components, SAE Technical Paper 2001-01-0421 (2001).

https://doi.org/10.4271/2001-01-0421.

45. S. Song, G.L. Song, W. Shen, M. Liu, Corrosion and electrochemical evaluation of coated magnesium alloys. Corrosion 68 (2012) 015005. https://doi.org/10.5006/1.3674295.

46. A.D. King, N. Birbilis, J.R. Scully, Accurate electrochemical measurement of magnesium corrosion rates; a combined impedance, mass-loss and hydrogen collection study, Electrochim. Acta 121 (2014) 394-406. https://doi.org/10.1016/j.electacta.2013.12.124.

47. L.G. Bland, A.D. King, N. Birbilis, J.R. Scully, Assessing the corrosion of commercially pure magnesium and commercial AZ31B by electrochemical impedance, mass-loss, hydrogen collection, and inductively coupled plasma optical emission spectrometry solution analysis, Corrosion 71 (2015) 128-145. https://doi.org/10.5006/1419.

48. V. Shkirskiy, A.D. King, O. Gharbi, P. Volovitch, J.R. Scully, K. Ogle, N. Birbilis, Revisiting the electrochemical impedance spectroscopy of magnesium with online inductively coupled plasma atomic emission spectroscopy, ChemPhysChem, 16 (2015) 536-539. https://doi.org/10.1002/cphc.201402666.

49. L. Wang, D. Snihirova, M. Deng, C. Wang, B. Vaghefinazari, G. Wiese, M. Langridge, D. Höche, S.V. Lamaka, M.L. Zheludkevich, Insight into physical interpretation of high frequency time constant in electrochemical impedance spectra of Mg, Corros. Sci. 187 (2021) 109501. https://doi.org/10.1016/j.corsci.2021.109501.

50. N. Birbilis, A.D. King, S. Thomas, G.S. Frankel, J.R. Scully, Evidence for enhanced catalytic activity of magnesium arising from anodic dissolution, Electrochim. Acta 132 (2014) 277-283. https://doi.org/10.1016/j.electacta.2014.03.133

51. Z. P. Cano, M. Danaie, J. R. Kish, J. R. McDermid, G. A. Botton and G. Williams, Physical characterization of cathodically-activated corrosion filaments on magnesium

alloy AZ31B, Corrosion 71 (2015) 146-159. https://doi.org/10.5006/1384.

52. K.A. Unocic, H.H. Elsentriecy, M.P. Brady, H.M. Meyer III, G. Song, M. Fayek, R.A. Meisner, B. Davis, Transmission electron microscopy study of aqueous film formation and evolution on magnesium alloys, J. Electrochem. Soc. 161 (2014) C302-C311. https://doi.org/10.1149/2.024406jes.

53. D. Hoche, C. Blawert, S. V. Lamaka, N. Scharnagl, C. Mendis and M. L. Zheludkevich, The effect of iron re-deposition on the corrosion of impurity-containing magnesium, Phys. Chem. Chem. Phys. 18 (2016) 1279-1291. https://doi.org/10.1039/C5CP05577F.

54. J. Li, W. Sun, B. Hurley, A. A. Luo and R. G. Buchheit, Cu redistribution study during the corrosion of AZ91 using a rotating ring-disk collection experiment, Corros. Sci. 112 (2016) 760-764. https://doi.org/10.1016/j.corsci.2016.08.011.

Chapter 6

Global Discussion

When added as an inhibitor just below the solubility limit of 12.75 g/L (0.1725 M) at 25 °C [1], Li_2CO_3 (aq) can significantly reduce corrosion of Mg alloy sheet metal product. The addition of 100 mM Li_2CO_3 (aq) significantly reduces corrosion of AZ31B (H24 temper) and ZEK100 (O temper) in 0.1 M NaCl (aq) at ambient temperature by a factor of ~10 (Chapter 3) and ~12 (Chapter 4) respectively. Inhibition is a complex process that involves a reduction in the global anode and cathode kinetics, as well as a suppression of localized activation (anode and cathode) at sites where the intact surface film breaks down locally. The lack of a significant substrate (alloy composition) effect on the degree on inhibition is a significant finding from a “one size fits all” perspective for controlling corrosion of Mg alloy components using the two-layer protective coating scheme preferred by the automotive industry (surface pre-treatment inner layer with epoxy E-coating sealant over-layer) [2,3]. The idea going forward is to incorporate leachable Li_2CO_3 either as a standalone surface pre-treated coating or as an inhibitor additive within an appropriate polymer coating, akin to what has been successfully demonstrated for Al alloys [4-6], complete with an epoxy E-coating sealant over-layer.

6.1 Corrosion Inhibition Mechanism

Figure 6.1 shows a schematic comparing the various stages that are suspected to be involved during the corrosion of Mg alloys immersed in NaCl (aq) with and without inhibition imparted by a leachable Li_2CO_3 component, either as a standalone coating or as an inhibitor additive to a coating. For simplicity, key aspects are compared for two basic stages of corrosion: (i) initiation (localized breakdown of the intact film/coating) and (ii) propagation (activation and associated anodic film formation). Two key factors believed to be involved in either sustaining or suppressing activation include: (i) composition and relative chemical stability of the anodic film formed and (ii) composition of solution within the occluded cell that is the breakdown site. A detailed physical description of two basic stages is discussed separately as follows.

Stage 1: Corrosion Initiation

For the bare metal case, activated corrosion would initiate at localized site where the intact surface film breaks down. The intact surface film is comprised of a thicker, more porous $Mg(OH)_2$-rich layer residing on top of a thinner, less porous MgO-rich inner layer [7-9]. Incorporation of Cl^- ions into the intact surface film is a necessary precursor step to weaken the chemical stability prior to breakdown [10,11]. Breakdown has been linked to micro-galvanic cell activity between Al-Mn intermetallic particles, where the particles serves as the cathode and the α-Mg matrix phase serves as the anode [12,13]. Presumably, the galvanic coupling anodically- polarizes the film covered α-Mg matrix above the breakdown potential, but such a physical description is lacking this sequence of events.

Alternatively, breakdown has also been linked to the tendency for MgO to chemically transform to $Mg(OH)_2$ via the following process involving hydration, dissolution and precipitation [14-16]:

$$MgO + H_2O \rightarrow MgO \cdot HOH \rightarrow Mg^{2+}(aq) + 2OH^-(aq) \rightarrow Mg(OH)_2(s) \qquad (1)$$

Breakdown here is also assisted the positive volume change that accompanies the transformation of MgO to $Mg(OH)_2$, which causes a stress-induced rupture [7,17]. Since grain boundaries transform faster than the grains [18,19], it is easy to imagine how the stress rupture process creates a continuous pathway to contact the bare metal surface with the corrosive solution.

For the coated metal case, with a leachable Li_2CO_3 component, breakdown would involve a through-thickness defect that places the bare metal in direct contact with a corrosive solution.

The defect could be a pre-existing one that is formed during the coatings process or one that is formed during service where the coating break downs locally by various physical and/or chemical environmental factors. Once in contact with the corrosive solution, Li_2CO_3 would dissolve, setting up the following chemical equilibria (with the equilibrium solubility product (k_{sp}) and base (k_b) constants quoted for 298 K [20]):

$$Li_2CO_3(s) \rightarrow 2Li^+(aq) + CO_3^{-2}(aq) \quad k_{sp} = 8.15 \times 10^{-4} \qquad (2)$$

$$CO_3^{2-}(aq) + H_2O \rightarrow HCO_3^-(aq) + OH^-(aq) \quad k_b = 2 \times 10^{-4} \qquad (3)$$

If Li_2CO_3 dissolves to form a saturated solution (12.75 g/L (0.1725 M) at 25 °C [1]) within the occluded cell that is the defect site, then the corresponding pH would drop from near-neutral to about ~11, when just considering Equation (3) as the only chemical equilibrium associated with CO_3^{2-} (aq).

Thus, the main difference between the cases is the corrosion solution composition within the occluded cell that is the breakdown site. For the bare metal case, the corrosive solution is a near-neutral solution containing Cl^- as an aggressive ions. For the coated metal case, the corrosive solution is alkaline and contains Li^+, CO_3^{2-} and OH^- inhibiting ions in addition to aggressive Cl^- ions. In both cases, bare metal contacts the corrosive solution and activated corrosion initiates.

Stage 2: Corrosion Propagation

For both the bare metal and coated metal cases, activated corrosion would involve the close localized coupling of activated anodic dissolution and concomitant cathodic H_2 gas evolution [21]. A physical description of this stage is lacking given the lack of agreement on the actual cathode activation mechanism [22]. Regardless of the exact cathode mechanism, fast anodic film MgO formation as thin, relatively dense inner layer via Equation (4) would be expected based on detailed TEM examination [7-9]:

$$Mg\ (s) + H_2O \rightarrow MgO\ (s) + 2H^+\ (aq) + 2e^- \qquad (4)$$

Concrete in-situ evidence in support of this claim is the AES-ICP work that shows a consistent difference between the anodic charged passed from an anodically dissolving Mg surface and the quantity of charge passed determined from the detected of Mg^{2+} (aq), which can be accounted for by film formation [23]. For the bare metal case, the composition of MgO is not altered in any meaningful way. However, for the coated metal case, the composition of MgO is significantly altered by the incorporation of Li. Formation of a similar film formed during the corrosion of an Mg-Li-(Al-Y-Zr) alloy has been argued to involve a charge compensation mechanism [24].

For the bare metal case, activation would be sustained on account of two contributing factors that undermine the physical integrity of the anodic MgO film formed through stress rupturing. First is the tendency for the MgO film subsequently transform to the larger molar volume $Mg(OH)_2$ via the hydration, dissolution and precipitation reaction sequence (Equation (3)), similar to the breakdown process described for Stage 1. Second is the activated cathode H_2 gas evolution, and associated pressure build up, that accompanies activated anode dissolution of the bare metal. Stress rupture would serve to promote contact of new bare metal surface with the corrosion solution, thus sustaining propagation of the localized activated corrosion.

For the coated metal case, activation would be suppressed on account of two contributing factors. First is a physical factor that involves an increased chemical stability of the Li-doped MgO film against transformation to $Mg(OH)_2$ via the hydration, dissolution and perception reaction sequence (Equation (3)). The simplest explanation is the slower MgO transformation kinetics exhibited in alkaline solutions [14,15]. Second is an electrochemical factor that involves Li^+ ions inhibiting activated cathode H_2 gas evolution. Dissolved Li^+ would inhibit H_2 evolution kinetics by modifying the Mg-H bond energy in the presence of Li^+ in the presence of OH^- [25,26].

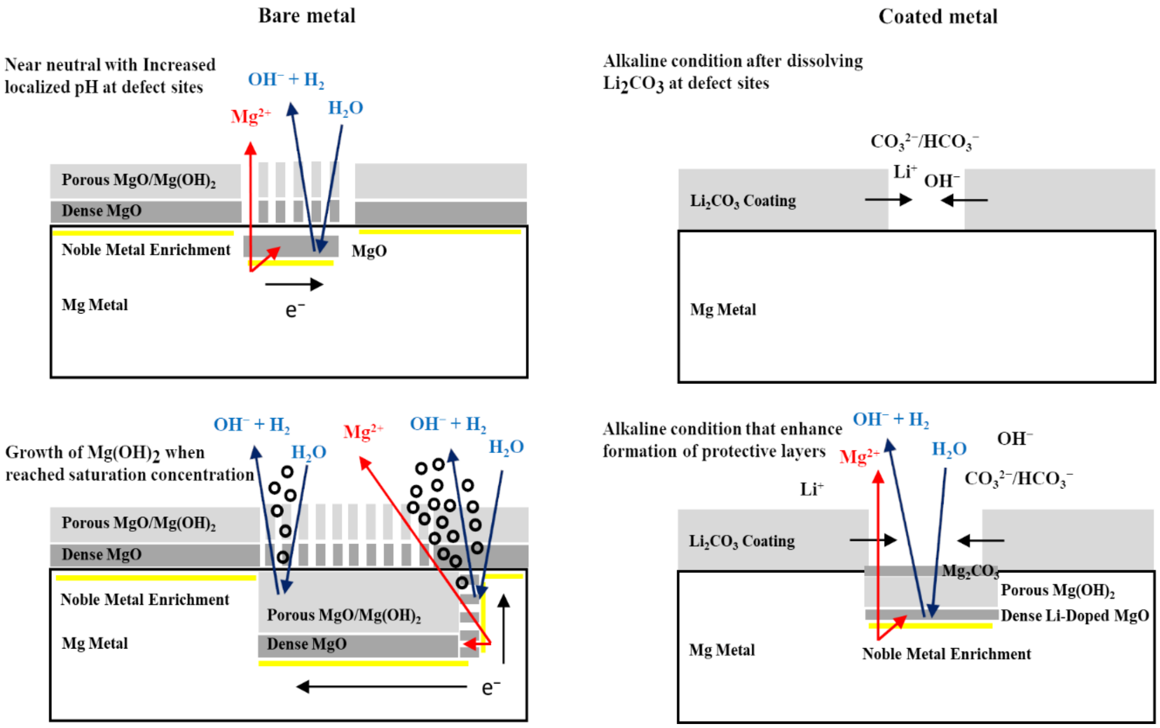

Figure 6.1. Schematic model shows the filament corrosion initiation and propagation stages for bare metal case and filament corrosion initiation and suppression for coated metal case.

6.2 Protective Coating Scheme Development Prospects

Spray-depositing Li_2CO_3 onto ZEK100, as a corrosion inhibiting surface pre-treatment layer, showed promising results in terms of controlling corrosion in 0.1 M NaCl (aq) (Chapter 5). The spray-coated layer exhibits key favorable characteristics expected of a barrier layer, including being uniform, compact, adherent and free of major defects such as pores and cracks. The looming question is here is how is compatible the Li_2CO_3-coated surface with the cationic epoxy E-coating sealant over-layer preferred by the automotive industry.

The cationic epoxy E-coating process is an electrophoretic deposition process that involves two steps: (i) charged cation-stabilized epoxy-based resin micelles dissolved in water migrate towards the working surface (cathode) under an applied electric field (electrophoresis) and (ii) neutralized (deprotonated) epoxy-based resin micelles then deposit on the working surface (cathode) forming a relatively dense and homogeneous compact pre-film (deposition) that is subsequently cured to promote polymerization [27-31]. These steps can be represented by two fundamental reactions:

$$2H_2O + 2e^- \rightarrow 2OH^-\ (aq) + H_2\ (g) \tag{5}$$

$$R - NH_3^+\ (aq) + OH^-(aq) \rightarrow R - NH_2\ (s) + H_2O \tag{6}$$

Equation 5 is surface alkalization reaction that generates OH^- as a product of the H_2 gas evolution reaction. Equation 6 is the deposition reaction whereby the dissolved cationic amino-epoxy resin ($R–NH3^+$) reacts with the OH^- (aq) produced to form the insoluble (deprotonated) neutral amino-epoxy resin ($R–NH_2$), which deposits on the cathode surface, forming the pre-film. The electrolyte basically consists of 80% water and 20% solids (resin and pigments) with pH 5.8-6.2 [28]. Thus, one major concern here is the tendency for the Li_2CO_3 coating to dissolve in slightly acidic aqueous electrolyte. Such a tendency to dissolved in near-neutral 0.1 M NaCl (aq) limited the measurements of the electrochemical response of the Li_2CO_3-coated ZEK100 surface in Chapter 5 to relatively short exposure times (~10 minutes). Future work will involve sending a set of spray-deposited Li_2CO_3-coated ZEK100 samples to ACT Test Panels LLC (Hillsdale, LI) for application of a commercial E-coating prior to a subsequent corrosion assessment.

6.3 References

[1] W. Cheng, Z. Li, and F. Cheng, “Solubility of Li2CO3 in Na-K-Li-Cl brines from 20 to 90 °c,” *J. Chem. Thermodyn.*, vol. 67, pp. 74–82, 2013, doi: 10.1016/j.jct.2013.07.024.

[2] G. S. Cole, “Magnesium (Mg) corrosion protection techniques in the automotive industry” *Corrosion Prevention of Magnesium Alloys*, pp. 489-508, 2013, *Woodhead* Publishing Limited, doi.org/10.1533/9780857098962.4.489.

[3] I. Milošev and G. S. Frankel, “Review—Conversion Coatings Based on Zirconium and/or Titanium,” *J. Electrochem. Soc.*, vol. 165, no. 3, pp. C127–C144, 2018, doi: 10.1149/2.0371803jes.

[4] P. Visser, Y. Gonzalez-Garcia, J. M. C. Mol, and H. Terryn, “Mechanism of Passive Layer Formation on AA2024-T3 from Alkaline Lithium Carbonate Solutions in the Presence of Sodium Chloride,” *J. Electrochem. Soc.*, vol. 165, no. 2, pp. C60–C70, 2018, doi: 10.1149/2.1011802jes.

[5] P. Visser, H. Terryn, and J. M. C. Mol, “Active corrosion protection of various aluminium alloys by lithium-leaching coatings,” *Surf. Interface Anal.*, vol. 51, no. 12, pp. 1276–1287, 2019, doi: 10.1002/sia.6638.

[6] Kosari, A., Visser, P., Tichelaar, F., Eswara, S., Audinot, J.N., Wirtz, T., Zandbergen, H., Terryn, H. and Mol, J.M.C, “Cross-sectional characterization of the conversion layer formed on AA2024-T3 by a lithium-leaching coating,” *Appl. Surf. Sci.*, vol. 512, pp. 145665, 2020, doi: 10.1016/j.apsusc.2020.145665.

[7] M. Taheri, R. C. Phillips, J. R. Kish, and G. A. Botton, “Analysis of the surface film formed on Mg by exposure to water using a FIB cross-section and STEM-EDS,” *Corros. Sci.*, vol. 59, pp. 222–228, 2012, doi: 10.1016/j.corsci.2012.03.001.

[8] Unocic, K.A., Elsentriecy, H.H., Brady, M.P., Meyer III, H.M., Song, G., Fayek, M., Meisner, R.A. and Davis, B, “Transmission Electron Microscopy Study of

Aqueous Film Formation and Evolution on Magnesium Alloys," *J. Electrochem. Soc.*, vol. 161, no. 6, pp. C302–C311, 2014, doi: 10.1149/2.024406jes.

[9] Z. P. Cano, M. Danaie, J. R. Kish, J. R. Mcdermid, G. A. Botton, and G. Williams, "Physical Characterization of Cathodically-Activated Corrosion Filaments on Magnesium Alloy AZ31B," *Corrosion*, vol. 71, no. 2, pp. 146–159, 2015, doi.org/10.5006/1384.

[10] H. B. Yao, Y. Li, and A. T. S. Wee, "XPS investigation of the oxidation/corrosion of melt-spun Mg," *Appl. Surf. Sci.*, vol. 158, no. 1, pp. 112–119, 2000, doi: 10.1016/S0169-4332(99)00593-0.

[11] J. R. Kish, Y. Hu, J. Li, W. Zheng, and J. R. Mcdermid, "Technical Note : Examination of Focused Ion Beam-Sectioned Surface Films Formed on AM60B Mg Alloy in an Aqueous Saline Solution," *Corrosion*, vol. 68, no. 6, pp. 468–474, 2012, doi.org/10.5006/i0010-9312-68-6-468.

[12] L. G. Bland, N. Birbilis, and J. R. Scully, "Exploring the Effects of Intermetallic Particle Size and Spacing on the Corrosion of Mg-Al Alloys Using Model Electrodes," *J. Electrochem. Soc.,* vol. 163, no. 14, pp. C895–C906, 2016, doi: 10.1149/2.1151614jes.

[13] Krebs, H.M., Chirazi, A., Lechner, L., Gelb, J., Zhou, X., Thompson, G.E. and Withers, P.J., "Time-Lapse Correlative 3D Imaging Applied to the Corrosion Study of AZ31 Mg Alloy in a Saline Environment," *Front. Mater. Process. Appl. Res. Technol.*, pp. 165–177, 2018, Springer, Singapore, doi: 10.1007/978-981-10-4819-7_15.

[14] D. A. Vermilyea, "The Dissolution of MgO and $Mg(OH)_2$ in Aqueous Solutions," *J. Electrochem. Soc.*, vol. 116, no. 9, pp. 1179-1183, 1969, doi: 10.1149/1.2412273.

[15] Fruhwirth, O., Herzog, G.W., Hollerer, I. and Rachetti, A, "Dissolution and

hydration kinetics of MgO," *Surf. Technol.*, vol. 23, no. 2, pp. 4461–4464, 1985, doi.org/10.1016/0376-4583(85)90080-9.

[16] J. H. Nordlien, S. Ono, N. Masuko, and K. Nisancioglu, "A tem investigation of naturally formed oxide films on pure magnesium," *Corros. Sci.*, vol. 39, no. 8, pp. 1397–1414, 1997, doi: 10.1016/S0010-938X(97)00037-1.

[17] M. Taheri and J. R. Kish, "Nature of Surface Film Formed on Mg Exposed to 1 M NaOH," *J. Electrochem. Soc.*, vol. 160, no. 1, pp. C36–C41, 2013, doi: 10.1149/2.018302jes.

[18] J. H. Lee, J. H. Eun, S. G. Kim, S. Y. Park, M. J. Lee, and H. J. Kim, "Hydration behavior of MgO single crystals and thin films," *J. Mater. Res.*, vol. 18, no. 12, pp. 2895–2903, 2003, doi: 10.1557/JMR.2003.0404.

[19] J. H. Lee, J. H. Eun, S. Y. Park, S. G. Kim, and H. J. Kim, "Hydration of r.f. magnetron sputtered MgO thin films for a protective layer in AC plasma display panel," *Thin Solid Films*, vol. 435, no. 1–2, pp. 95–101, 2003, doi: 10.1016/S0040-6090(03)00411-5.

[20] The Handbook of Chemistry and Physics, 82nd Edition by David R. Lide. CRC Press LLC 2002, 2002.

[21] E. Michailidou, H. N. McMurray, and G. Williams, "Quantifying the Role of Transition Metal Electrodeposition in the Cathodic Activation of Corroding Magnesium," *J. Electrochem. Soc.*, vol. 165, no. 5, pp. C195–C205, 2018, doi: 10.1149/2.0251805jes.

[22] S. Thomas, N. V. Medhekar, G. S. Frankel, and N. Birbilis, "Corrosion mechanism and hydrogen evolution on Mg," *Curr. Opin. Solid State Mater. Sci.*, vol. 19, no. 2, pp. 85–94, 2015, doi: 10.1016/j.cossms.2014.09.005.

[23] S. Thomas, O. Gharbi, S. H. Salleh, P. Volovitch, K. Ogle, and N. Birbilis, "On the effect of Fe concentration on Mg dissolution and activation studied using atomic

emission spectroelectrochemistry and scanning electrochemical microscopy," *Electrochim. Acta*, vol. 210, pp. 271–284, 2016, doi: 10.1016/j.electacta.2016.05.164.

[24] Yan, Y.M., Maltseva, A., Zhou, P., Li, X.J., Zeng, Z.R., Gharbi, O., Ogle, K., La Haye, M., Vaudescal, M., Esmaily, M. and Birbilis, N, "On the in-situ aqueous stability of an Mg-Li- (Al-Y-Zr) alloy : Role of Li," vol. 164, pp. 108342, 2020, doi.org/10.1016/j.corsci.2019.108342.

[25] A. Guha, S. Narayanaru, and T. N. Narayanan, "Tuning the Hydrogen Evolution Reaction on Metals by Lithium Salt," *ACS Appl. Energy Mater.*, vol. 1, no. 12, pp. 7116–7122, 2018, doi: 10.1021/acsaem.8b01546.

[26] A. Guha, N. M. Kaley, J. Mondal, and T. N. Narayanan, "Engineering the hydrogen evolution reaction of transition metals: Effect of Li ions," *J. Mater. Chem. A*, vol. 8, no. 31, pp. 15795–15808, 2020, doi: 10.1039/c9ta12926j.

[27] F. BECK, "Fundamental Aspects of Electrodeposition of Paint," *Process Org. Coatings*,4, vol. 4, no. 1, pp. 1-60, 1976, doi.org/10.1016/0300-9440(76)80001-X.

[28] Arlt, K, "CATHODIC DEPOSITION OF PAINT," Electrochim. Acta, vol. 39, no. 8-9, pp. 1189–1193, 1994, doi.org/10.1016/0013-4686(94)E0036-Y

[29] N. M. Aćamović, D. M. Dražić, and V. B. Mišković-Stanković, "Influence of substrate on the formation and growth kinetics of cathodic electrocoat paint," *Prog. Org. Coatings*, vol. 25, no. 3, pp. 293–307, 1995, doi: 10.1016/0300-9440(94)00511-X.

[30] L. Besra and M. Liu, "A review on fundamentals and applications of electrophoretic deposition (EPD)," *Prog. Mater. Sci.*, vol. 52, no. 1, pp. 1–61, 2007, doi: 10.1016/j.pmatsci.2006.07.001.

[31] N. Van Phuong and S. Moon, "Deposition and characterization of E-paint on magnesium alloys," *Prog. Org. Coatings*, vol. 89, pp. 91–99, 2015, doi:

10.1016/j.porgcoat.2015.08.014.

[32] G. L. Song, "'Electroless' deposition of a pre-film of electrophoresis coating and its corrosion resistance on a Mg alloy," *Electrochim. Acta*, vol. 55, no. 7, pp. 2258–2268, 2010, doi: 10.1016/j.electacta.2009.11.078.

[33] J. Hu, D. Huang, G. Zhang, G. L. Song, and X. Guo, "Research on the inhibition mechanism of tetraphenylporphyrin on AZ91D magnesium alloy," *Corros. Sci.*, vol. 63, pp. 367–378, 2012, doi: 10.1016/j.corsci.2012.06.021.

Chapter 7

Conclusions

The overarching hypothesis of this thesis is the idea that dissolved Li_2CO_3 can impart effectively inhibit corrosion of Mg alloy sheet metal when immersed in NaCl (aq) by combining the inhibiting capability of dissolved Li^+, albeit based on an alloyed Li effect, and carbonate ($CO_3^{2-}/HCO_3^-/OH^-$) on both anode and cathode kinetics and protective surface film formation. Three global conclusions can be drawn from the research conducted to prove the hypothesis correct, which are summarized as follows.

1. When added as an inhibitor just below the solubility limit at 25 °C, Li_2CO_3 (aq) can significantly reduce corrosion of Mg alloy sheet metal product. The addition of 100 mM Li_2CO_3 (aq) significantly reduces corrosion of AZ31B (H24 temper) and ZEK100 (O temper) in 0.1 M NaCl (aq) at ambient temperature by a factor of ~10 (Chapter 3) and ~12 (Chapter 4) respectively.

2. Inhibition is a complex process that involves a reduction in the global anode and cathode kinetics, as well as a suppression of localized activated corrosion (activated anodic dissolution and concomitant activated cathode H_2 gas evolution) at sites where the intact surface film breaks down locally. Two factors are proposed to account for localized activated corrosion suppression. First is a physical factor that involves an increased chemical stability of the Li-doped MgO

film, formed during anodic dissolution, against transformation to $Mg(OH)_2$ via the hydration, dissolution and perception reaction sequence. Second is an electrochemical factor that involves Li^+ ions inhibiting activated cathode H_2 gas evolution in the presence of OH^- ions.

3. Spray-depositing Li_2CO_3 onto ZEK100, as a corrosion inhibiting surface pre-treatment layer, showed promising results in terms of controlling corrosion in 0.1 M NaCl. Improved corrosion control is attributed to the formation of uniform, compact, adherent and defect-free coating (physical barrier contribution) and the ability of dissolved Li_2CO_3 to inhibit both the global anode and cathode kinetics and suppression of localized activated corrosion (electrochemical).
